KfK 4294
Februar 1988

Searches for Supersymmetric Particles with the Cello Detector at Petra

H. Küster
Institut für Kernphysik

Kernforschungszentrum Karlsruhe

KERNFORSCHUNGSZENTRUM KARLSRUHE

Institut für Kernphysik

KfK 4294

SEARCHES FOR SUPERSYMMETRIC PARTICLES WITH THE CELLO DETECTOR AT PETRA

HERMANN KÜSTER

Kernforschungszentrum Karlsruhe GmbH, Karlsruhe

von der Fakultät für Physik der Universität Karlsruhe genehmigte Dissertation

Kernforschungszentrum Karlsruhe GmbH
Postfach 3640, 7500 Karlsruhe 1

ISSN 0303-4003

SEARCHES FOR SUPERSYMMETRIC PARTICLES WITH THE CELLO DETECTOR AT PETRA

Abstract

A search was made for missing transverse momentum final states such as acoplanar lepton pairs, acoplanar jets, single electrons, and single jets in e^+e^- collisions at center of mass energies between 40 and 46.78 GeV. Moreover, multihadronic final states were searched for an excess of spherical events. No unexpected signal was observed. This result is used to put mass limits on various supersymmetric particles, namely scalar electrons, scalar taus, winos, zinos, and higgsinos considering various assumptions on their decay modes. An extensive discussion is given of the consequences of various choices for the lightest supersymmetric particle and of gaugino higgsino mixing. In addition, limits are given on pair production of charged Higgses (or technipions) and on a fourth generation heavy lepton.

SUCHE NACH SUPERSYMMETRISCHEN TEILCHEN MIT DEM CELLO DETEKTOR BEI PETRA

Zusammenfassung

Es wird berichtet über eine Suche nach Endzuständen mit fehlendem Transversalimpuls wie acoplanare Leptonpaare, acoplanare Jets, einzelne Elektronen und einzelne Jets in e^+e^- Kollisionen bei Schwerpunktsenergien zwischen 40 und 46.78 GeV. Außerdem wurden hadronische Endzustände auf einen Überschuß an sphärischen Ereignissen hin untersucht. Kein unerwartetes Signal wurde beobachtet. Dies Ergebnis wurde benutzt, um Massengrenzen zu setzten für verschiedene supersymmetrische Teilchen wie skalare Elektronen, skalare Taus, Winos, Zinos und Higgsinos unter verschiedenen Annahmen über ihre Zerfallseigenschaften. Die Konsequenzen von verschiedenen Annahmen über das leichteste supersymmetrische Teilchen und über Gaugino - Higgsino Mischung werden ausführlich diskutiert. Zusätzlich werden Grenzen angegeben für die Paarerzeugung geladener Higgse (oder Technipions) und für ein schweres Lepton einer vierten Generation.

Contents

Introduction

Within the last decade, initiated by the discovery of neutral currents [1] and the charm quark [2], the so-called Standard Model of elementary particles and their interactions evolved. The spectrum of elementary particles in the Standard Model is quite simple (Tab. 1):

Fermions

$$T_3=+1/2 \begin{pmatrix} \nu_e \\ e \end{pmatrix}_L \quad \begin{pmatrix} \nu_\mu \\ \mu \end{pmatrix}_L \quad \begin{pmatrix} \nu_\tau \\ \tau \end{pmatrix}_L \qquad \begin{pmatrix} u \\ d \end{pmatrix}_L \quad \begin{pmatrix} c \\ s \end{pmatrix}_L \quad \begin{pmatrix} t \\ b \end{pmatrix}_L$$

$$T_3=-1/2$$

$$T_3=0 \qquad e_R \;\; \mu_R \;\; \tau_R \;\; \nu_{e,R} \;\; \nu_{\mu,R} \;\; \nu_{\tau,R} \qquad u_R \;\; d_R \;\; c_R \;\; s_R \;\; t_R \;\; b_R$$

Bosons

$$SU(3)_C \quad \times \quad SU(2)_L \quad \times \quad U(1)$$

$$g \qquad\qquad W \;\; Z^0 \qquad\qquad \gamma$$

Higgs Sector

$$H^0_{(i)} \qquad (H^{+/-})_i$$

Table 1: The Standard Model particle spectrum. The left handed fermions are in $SU(2)_L$ doublets while the right handed ones are in singlets.

Matter is built from fermions, the quarks and leptons, which come in 3 repetitive families. Interactions are mediated by spin 1 vector gauge bosons arising from symmetry under local transformations within the gauge group $SU(3)_C \otimes SU(2)_L \otimes U(1)$. The left handed fermions form doublets under the $SU(2)_L$ while the right handed ones are singlets. Mixing occurs between the neutral gauge bosons of the

$U(1)$ (B^0) and the $SU(2)_L$ (W_3^0) giving rise to the photon and the Z^0

$$\begin{aligned} \gamma &= B^0 cos\Theta_W + W_3^0 sin\Theta_W \\ Z^0 &= -B^0 sin\Theta_W + W_3^0 cos\Theta_W, \end{aligned} \tag{.1}$$

where Θ_W is the Weinberg mixing angle between electromagnetic and weak interaction.

An additional necessary ingredient is the spontaneous breaking of the as yet perfect $SU(2)_L \otimes U(1)$ symmetry down to $U(1)_{em}$ in order to give masses to the $W^{\pm}$ and Z^0 bosons and to the fermions. This is achieved by a set of weak scalars, the Higgs bosons. A minimum of one weak isospin doublet of complex scalar fields corresponding to 4 degrees of freedom is needed. 3 of them are absorbed into the W and Z^0 giving them masses and therefore longitudinal polarisation states. One remains as an observable particle. This Higgs particle, a central ingredient of the Standard Model, still awaits discovery.

At present this simple and elegant model describes all experimental observations with remarkable accuracy. Its biggest triumph was the observation of the $W^{\pm}$ and Z^0 bosons with the predicted masses at the CERN $Sp\bar{p}S$ collider in 1983 [3].

However, several troubling questions remain unanswered, indicating that the Standard Model must be incomplete.

- For a fundamental theory the Standard Model has too many free parameters, among them 3 separate coupling constants for electromagnetic, weak, and strong interaction corresponding to the three gauge groups U(1), SU(2), and SU(3). Attempts to unify these interactions in a single gauge group with a single coupling constant (so called grand unified theories, GUTs) lead to an unification scale of order $10^{15} GeV$. Gauge bosons with a mass of this order of magnitude should mediate the decay of the proton. Then, present experimental limits on the proton lifetime start to conflict with a unification scale of $10^{15} GeV$.

- Within the Standard Model there is no way of preventing the elementary Higgs scalars from aquiring masses of the order of the unification scale by radiative corrections. This would make them useless for symmetry breaking at the weak scale of the order of 100 GeV. This so-called 'hierarchy problem' is not confined to GUT models, it is more generally a problem of two widely different energy scales. Even if there is no GUT scale at $\sim 10^{15} GeV$, the next (unavoidable) scale is the Planck scale at $10^{19} GeV$ where gravity becomes a strong force.

- Another set of free parameters are the fermion masses. No predictions whatsoever are made in the Standard Model.

- There is no relation between gravity and the other forces

This (partial) list indicates the need to go beyond the Standard Model. In particular the hierarchy problem seems to necessitate new physics at a scale not too far from the weak scale, i.e. $\lesssim$ 1 TeV.

So-called composite models introduce substructure for all or part of the Standard Model particles of Table .1. Technicolor, for instance, postulates the Higgses to be made up of fermions bound by a new force at a scale of O(TeV), avoiding elementary scalars and thus eliminating the hierarchy problem (dynamic symmetry breaking). The family problem is addressed by models in which fermions are composite. However, no phenomenologically viable model has yet been constructed.

Supersymmetry (SUSY) [4] connects fermions and bosons by the symmetry operation $j \rightarrow j + \Delta j$, $|\Delta j| = \pm 1/2$. The essential feature of supersymmetric models is the prediction of a partner for each known particle with the same couplings and quantum numbers except for the spin which differs by $|\Delta j| = \pm 1/2$, thus obtaining a symmetry between fermion and boson states. In this case many divergencies in Feynman diagrams are cancelled since fermions and bosons contribute equally with opposite sign. In particular the loop diagrams giving radiative corrections to the Higgs mass are cut off at an energy corresponding to the mass splitting between ordinary particles and their supersymmetric partners, thus solving the hierarchy problem.

The absence of mass degenerate partners of the ordinary particles shows that supersymmetry must be broken. Since the details of this symmetry breaking are unknown, there exists no convincing theory for the masses of the superpartners. (This is not worse than the situation for the usual fermions). However, if supersymmetry should be of relevance for the solution of the hierarchy problem, the mass splitting between the ordinary particles and their superpartners must not be much larger than the weak energy scale, i.e. at most of order 1 TeV.

Local supersymmetry (supergravity) may pave the way to a finite quantum theory of gravity and to a unification of all particle interactions. A theory of gravity should then also account for the elementary particle masses. Moreover, supersymmetry is a necessary ingredient of 'superstring' theories [5] which recently generated a lot of excitement as a promising candidate for a TOE ('Theory Of Everything').

Outline

In this thesis, searches for non-standard signatures (in particular missing p_t signatures such as acoplanar lepton pairs, single electrons, acoplanar jets, and single jets) in e^+e^- collisions at center of mass energies of up to 46.78 GeV are reported. These results are interpreted in terms of the production of supersymmetric particles, and mass limits on the superpartners of the leptons, the neutrinos, the photon, the weak gauge bosons, and the Higgses are presented. A search for charged scalars (charged Higgses or technipions) decaying into $\tau\nu$ as well as a new limit on a fourth generation heavy lepton are discussed in an appendix.

Chapter 1 gives an introduction to the spectrum of new particles predicted by a minimal supersymmetric model. The question of the lightest supersymmetric particle, which is of great phenomenological importance, is discussed.

In Chapter 2 a comprehensive overview is given on supersymmetric reactions in e^+e^- collisions. Rates and signatures are discussed. They greatly depend on the details of the unknown mass hierarchy of the supersymmetric particle spectrum.

An overview on the used experimental apparatus is given in Chapter 3. After a brief introduction of the PETRA e^+e^- storage ring, the CELLO detector is described. Tracking, calorimetry, muon identification, trigger, and data aquisition will be discussed.

Chapter 4 describes the CELLO analysis chain, the event filtering strategy and event reconstruction.

In Chapter 5 a detailed description is given of the searches for for acoplanar [1] 2 track events, single electrons, hadronic final states with missing energy and momentum, and for an excess of spherical hadronic events.

Chapter 6 gives an account of the procedures applied in calculating the expected number of events as a function of the mass of the particles involved. The

[1] Acoplanarity can be defined as 180° - ϕ where ϕ is the angle between two tracks (or jets) in the projection into the plane perpendicular to the beam axis. If the transverse momentum is conserved the acoplanarity is 0.

Monte Carlo methods used are described and the resulting detection efficiencies for various supersymmetric reactions are discussed.

All results in terms of excluded mass ranges for supersymmetric particles are summarized in Chapter 7, such that a reader less interested in experimental details may skip the previous chapters. A detailed discussion is given of the consequences of different assumptions on the supersymmetric particle mass hierarchy.

Total and differential cross sections of all the supersymmetric processes in e^+e^- interactions discussed in Chapter 2 are summarized in Appendix A.

Supersymmetry as well as technicolor models predicts the existence of physical charged scalar particles, be they Higgses or technipions. A search for these particles is described in Appendix B.

Pair production of a new heavy lepton has a signature very similar to wino pair production. In appendix C a new mass limit on a fourth generation heavy lepton is presented.

Chapter 1

Supersymmetry

The fundamental idea of supersymmetry [4] is to relate fermions to bosons by the symmetry operation $j \rightarrow j \pm 1/2$. This introduces a bosonic (fermionic) partner for each known fermion (boson). Then many divergencies in Feynman diagrams are cancelled since bosons and fermions contribute equally with opposite signs. In particular, the loop diagrams for the Higgs self energy which cause the hierarchy problem are cut off at an energy corresponding to the mass splitting between the contributing particles and their superpartners. In order to make this mechanism work, an exact equality in the number of fermionic and bosonic degrees of freedom is needed.

1.1 The Supersymmetric Particle Spectrum

Unfortunately, no known particle can be identified as the superpartner of any other, since there is no pair of particles with identical quantum numbers except a spin differing by 1/2. Hence we must double the Standard Model particle spectrum as shown in Tab. 1.1.

For each fermion (quarks and leptons) there exist two corresponding 'scalar fermions' $\tilde{f}$, one for each fermion helicity component, with, of course, different couplings with respect to weak interactions. The 'right handed' scalar electron $\tilde{e}_R$, for instance, like the right handed electron does not couple to the W. These two states, $\tilde{f}_L$ and $\tilde{f}_R$, may or may not be degenerate in mass. For instance, in some models the $\tilde{e}_L$ is expected to be heavier than the $\tilde{e}_R$ due to additional weak radiative corrections.

The vector bosons g, W, Z^0, and γ obtain spin 1/2 partners, the gluino $\tilde{g}$, the wino $\tilde{w}$ and zino $\tilde{z}$, and the photino $\tilde{\gamma}$.

For the Higgs particles one expects spin 1/2 partners, the higgsinos $\tilde{h}$. Note that in contrast to the minimal Standard Model supersymmetry requires a second Higgs doublet in order to give masses to both the up and down type quarks [6]. As

Spin	0	1/2	1	3/2	2
Matter	$\tilde{l}_L \ \tilde{l}_R$	l			
multiplets	$\tilde{q}_L \ \tilde{q}_R$	q			
		$\tilde{g}$	g		
Gauge	$H^{\pm}$	$\tilde{w}^{\pm} \ \tilde{h}^{\pm}$	$W^{\pm}$		
multiplets	$H_1^0 \ H_2^0 \ A^0$	$\tilde{z} \ \tilde{h}_1^0 \ \tilde{h}_2^0$	Z^0		
		$\tilde{\gamma}$	γ		
				$\tilde{G}$	G

Table 1.1: The minimal supersymmetric extension of the Standard Model particle spectrum. The SUSY fermions grouped in the dashed boxes may mix forming chargino and neutralino mass eigenstates respectively. In models with global supersymmetry breaking there exists a light spin 1/2 Goldstino. In locally supersymmetric models (supergravity) this is absorbed, giving mass and spin $\pm 1/2$ polarization states to the spin 3/2 gravitino.

a consequence, supersymmetry predicts the existence of physical charged Higgses. In addition, the (at least) two Higgs doublets are required to preserve the one to one correspondence between bosonic and fermionic degrees of freedom for the weak gauge bosons and Higgses and their respective fermionic partners.

There is no convincing theory for the masses of the superpartners. Even the ordering of the superpartner masses is quite model dependent. Moreover, the partners of the colourless vector bosons and the higgsinos are expected to mix forming 'neutralino' $\tilde{\chi}_i^0, i = 1 \cdots 4$ and 'chargino' $\tilde{\chi}_i^{\pm}, i = 1, 2$ mass eigenstates. Unfortunately, although all couplings of the SUSY particles are fixed, this mixing introduces a lot of freedom to neutralino and chargino couplings. Therefore, experimental searches for SUSY particles should be as independent as possible from specific assumptions on the supersymmetric mass spectrum and mixing.

SUSY particles carry a (in most models) conserved multiplicative quantum number R-parity which is defined as $R = (-1)^{2S+3B-L}$. Ordinary particles have R $= +1$ while R $= -1$ for their superpartners. For this reason, these can be produced only in pairs.

1.2 The Lightest Supersymmetric Particle

Of particular phenomenological importance is the lightest SUSY particle (LSP) since all SUSY particles eventually will decay into it. It is favoured to be colorless and neutral and it must be stable because of R-parity conservation. Moreover, it will only interact weakly with matter (i.e. ν-like) because all interactions involve the exchange of massive superparticles. The cross section for such interactions behaves roughly as

$$\sigma \propto \frac{1}{M_X^4} E\ m_p \tag{1.1}$$

were E is the energy of the particle impinging on a target of mass m_p. M_X is the mass of the exchanged particle. For instance, if the LSP is a photino its interaction with a quark (lepton) is mediated by exchange of a high mass scalar quark (lepton) as depicted in Fig. 1.1. **Therefore a general signature for supersymmetric processes is missing energy and momentum carried away by the LSP.** LSP candidates [7] are the photino, the neutral higgsino, the scalar neutrino, or a spin 1/2 Goldstino $\tilde{G}$ appearing in globally supersymmetric models [8]. (In locally supersymmetric models the Goldstino appears in disguise as the spin $\pm 1/2$ polarization state of the gravitino.)

If the photino were the lightest supersymmetric particle it would be stable. Constraints on the mass of a stable photino may be derived from the observed mass density of the universe using methods developed to bound the masses of stable neutrinos [9]. If the photino is light, one can compare [10] the contribution of photinos to the mass density of a 2.7 K universe,

$$\rho_{\tilde{\gamma}} \sim 109\ m_{\tilde{\gamma}}\ cm^{-3} \tag{1.2}$$

with the critical (closure) density

$$\rho_{crit} = (3.2 - 10.3)(keV/c^2)\ cm^{-3} \tag{1.3}$$

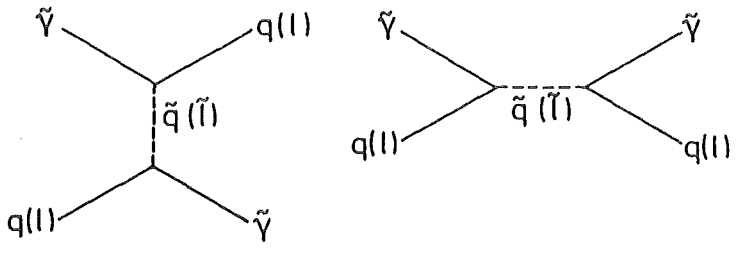

Figure 1.1: Feynman diagrams for the interaction of photinos with matter.

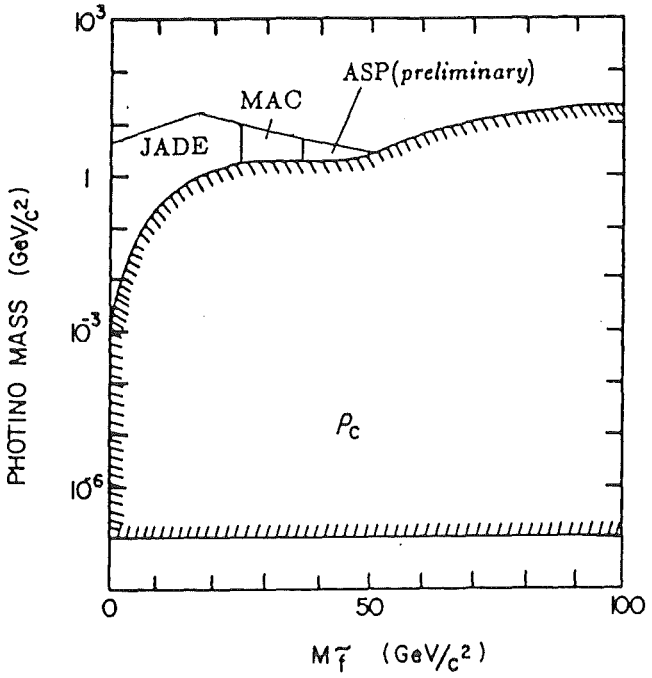

Figure 1.2: Limits on the photino mass derived from the mass density of the universe as a function of the mass of the lightest scalar partner of the fermions. The photino is assumed to be stable as the lightest supersymmetric particle.

(a reasonable upper bound on the observed density), to find

$$m_{\tilde{\gamma}} \lesssim 100\ eV/c^2. \tag{1.4}$$

Note that this upper bound on the mass of the photino is valid also for any other fermionic LSP, be it a higgsino or a zino.

When the photino mass exceeds about 1 MeV, it is necessary to take into account the annihilation of photinos into light fermions by the exchange of a scalar partner of the fermion. The result of this analysis [11] yields a lower bound on the mass of a 'heavy' photino, which is shown together with (1.4) in Figure 1.2

If a light Goldstino is the LSP the photino is expected to decay into a photon and a Goldstino (see Fig. 1.3b) with a lifetime [12]

$$\tau = \frac{8\pi d^2}{m_{\tilde{\gamma}}^5} \tag{1.5}$$

where $d = \Lambda_{SUSY}^2$ characterizes the scale of supersymmetry breaking.

Another LSP candidate is the neutral higgsino. In this case the photino would decay into a photon and a higgsino (see Fig 1.3c). For a wide range of parameters ($m_{\tilde{\gamma}}$, $m_{\tilde{h}}$, m_t, $m_{\tilde{t}}$, $\tilde{\gamma} - \tilde{h}$ mixing) the photino lifetime is sufficiently short that such a decay occurs inside a detector [13]. This scenario was discussed [14] as a possibility to weaken the missing p_t signature of photinos, thus making more room for SUSY reactions in the $p\bar{p}$ collider data.

Photinos can be pair produced in e^+e^- interactions by t-channel exchange of a scalar electron (see Fig. 1.3a.). The subsequent decay into photon and one of

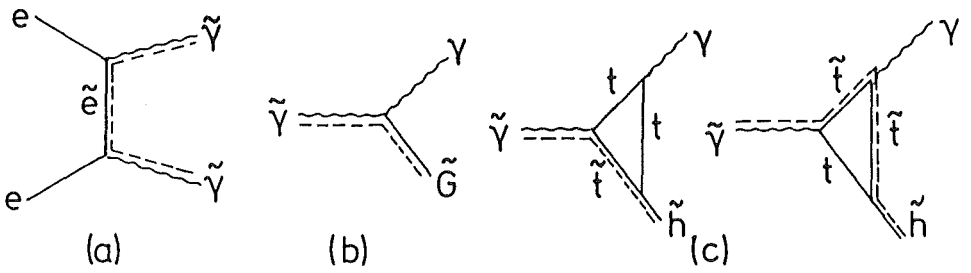

Figure 1.3: Diagrams for photino pair production (**a**) and decay into photon and Goldstino (**b**) or photon and higgsino (**c**).

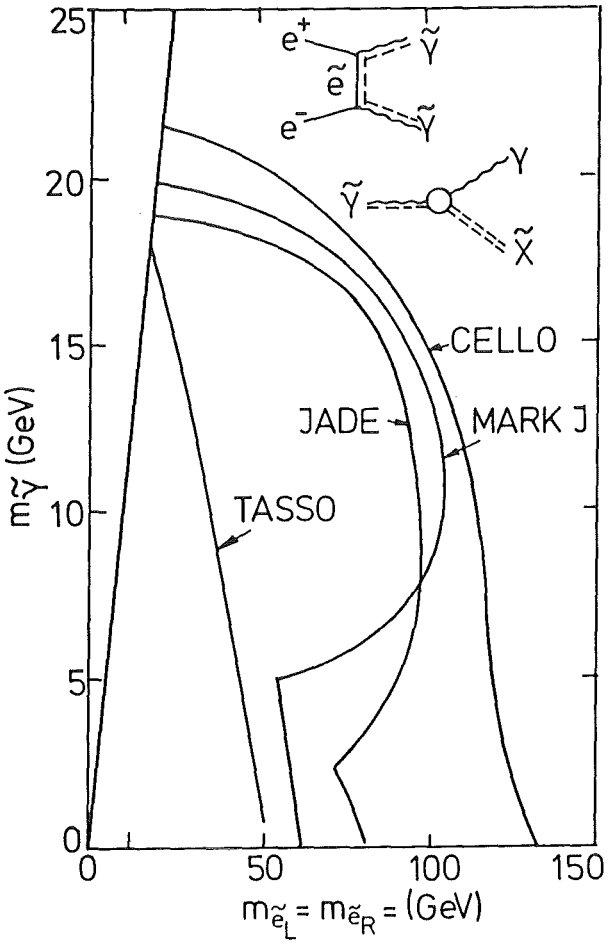

Figure 1.4: Excluded domain in photino and scalar electron mass for unstable photinos decaying inside the detector.

the LSP's discussed above produces, in case of a heavy photino, an acoplanar pair of photons with missing energy and momentum carried away by the unobserved LSP's, whereas for a light photino its decay photons are boosted into the original photino direction giving rise to a pair of collinear photons with missing energy. All four PETRA experiments [15,16,17,18] looked for these signatures and did not observe any signal.

Fig. 1.4 shows the status of the relevant searches. The message of this plot is that photinos below $\sim$ 20 GeV decaying inside a detector into a photon and a light penetrating particle are excluded if the scalar electron is lighter than $\sim$ 100 GeV, independent of any specific model. **For this reason the searches discussed in this work assume an invisible photino** (either stable or long lived or decaying invisibly, e.g. into $\tilde{\nu}\nu$).

Chapter 2

Supersymmetry in e^+e^- collisions

High energy e^+e^- collisions are a good place to look for the production of new particles. Before discussing specific processes, I would like to make some general remarks on new particle production mechanisms in e^+e^- collisions. The simplest case is the pair production of charged particles via single photon annihilation (Fig. 2.1a). The cross section depends on charge, spin, and mass of the particle:

$$\begin{aligned} \sigma(e^+e^- \to X^+X^-) &= Q^2 \frac{\beta(3-\beta^2)}{2}\sigma_{\mu\mu} \quad \text{for spin } 1/2 \\ \sigma(e^+e^- \to X^+X^-) &= Q^2 \frac{1}{4}\beta^3\sigma_{\mu\mu} \qquad\quad \text{for spin } 0 \end{aligned} \tag{2.1}$$

Here $\sigma_{\mu\mu} = 4/3\ \pi\alpha^2/s$ stands for the lowest order QED μ-pair cross section. Fig. 2.2 illustrates the threshold behavior for pair production of spin 0 and spin 1/2 particles. In the spin 0 case the cross section is suppressed by a β^3 p-wave threshold factor and by a factor 1/4 due to spin statistics.

Neutral particles can be pair produced by annihilation into a (at present energies virtual) Z^0 (Fig. 2.1b). For instance, at present PETRA energy ($\sqrt{s} = 44$ GeV) the muon neutrino pair production cross section is:

$$\sigma(e^+e^- \to Z^0 \to \nu_\mu\bar{\nu}_\mu) \sim 1.1pb \tag{2.2}$$

Correspondingly, the total cross section for Z^0 production at PETRA is

$$\sigma(e^+e^- \to Z^0 \to anything) = \frac{\sigma(e^+e^- \to Z^0 \to \nu_\mu\bar{\nu}_\mu)}{BR(Z^0 \to \nu\bar{\nu})} \sim 19pb. \tag{2.3}$$

This means that $\sim$ 900 Z^0's have been produced at each of the four PETRA interaction regions. Seen this way, at present PETRA (and PEP) are the largest Z^0 factories available! This large production rate opens up the possibility to search for unusual Z^0 decays at present energy e^+e^- colliders. (c.f. searches for monojets from Z^0 decays at PETRA and PEP [19].)

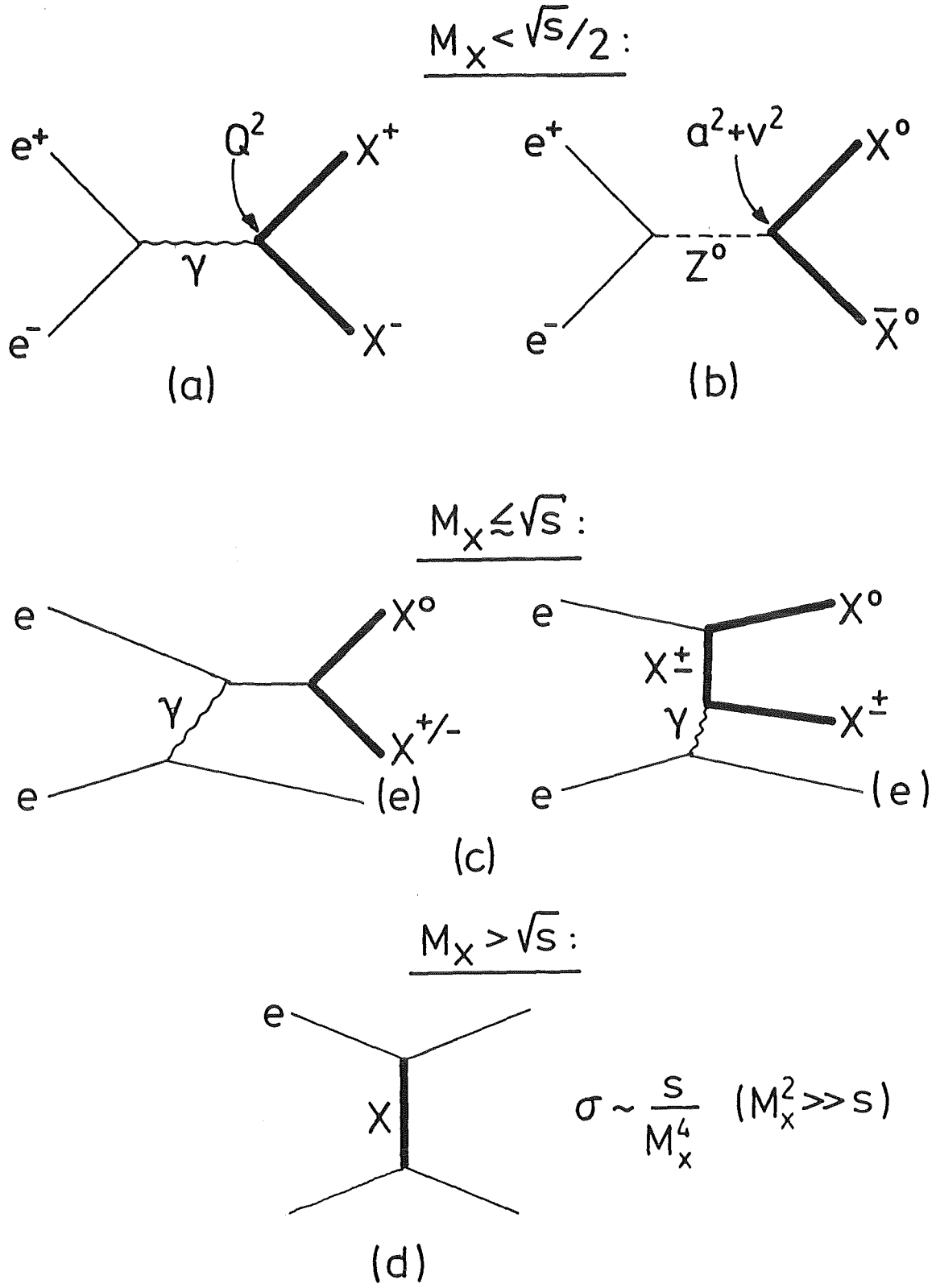

Figure 2.1: New particle production processes in e^+e^- collisions.

(a): pair production of a charged particle (e.g. $e^+e^- \rightarrow \tilde{l}^+\tilde{l}^-$)

(b): pair production of a neutral particle via virtual Z^0 exchange (e.g. $e^+e^- \rightarrow N\overline{N}$)

(c): single production of a charged particle together with a neutral one in $e\gamma$ collisions (e.g. $e^+e^- \rightarrow (e)\tilde{e}\tilde{\gamma}$)

(d): new particle in the propagator (e.g. $e^+e^- \rightarrow \tilde{\gamma}\tilde{\gamma}$ via $\tilde{e}$ exchange).

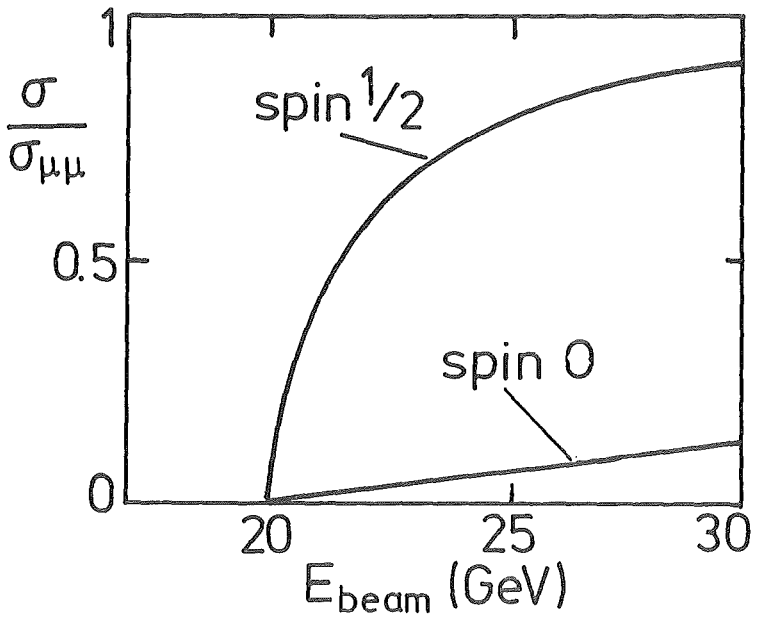

Figure 2.2: Threshold behavior for pair production of a m = 20 GeV, $|Q| = 1$ particle with spin 0 and spin 1/2.

Obviously, pair production of new particles is limited to masses below the beam energy. Higher masses can be probed in the associated production of a charged particle together with a (possibly light) neutral one in $e\gamma$ collisions (Fig. 2.1c). This process is sensitive to masses up to $\sqrt{s}$ - m_{X^0}.

Particles with masses above the c.m. energy can still be detected as virtual particles in the propagator (Fig. 2.1d).

Although limited in the available c.m. energy, as compared to hadron colliders, e^+e^- machines offer a very clean laboratory where potential new processes would stick out clearly over a well understood background.

Table 2.1 shows a comprehensive list of supersymmetric reactions in e^+e^- interactions. Production cross sections as a function of the masses of the supersymmetric particles involved are shown in Figs. 2.3, 2.4, and 2.5. In the rest of this Chapter we will give a discussion of all these processes. A summary of signatures of supersymmetric processes together with the most important conventional background processes can be found in Tab. 2.2 on page 31. The reactions which were searched for in this thesis are marked in the table. A complete account of a search by CELLO for all these processes can be found in Ref. [15]. For definiteness, in the following discussion we will assume the gauginos and higgsinos to be unmixed. A discussion of gaugino higgsino mixing will be given in Chapter 7.

	reaction	decay	signature	
	$e^+e^- \to \tilde{\gamma}\,\tilde{\gamma}$	$\tilde{\gamma} \to \gamma\widetilde{X}$	(c)	acoplanar photons
*	$e^+e^- \to \tilde{e}\,\tilde{e}$	$\tilde{e} \to e\tilde{\gamma}$	(a)	acoplanar $e-e$
	$e^+e^- \to \tilde{\mu}\,\tilde{\mu}$	$\tilde{\mu} \to \mu\tilde{\gamma}$	(a)	acoplanar $\mu-\mu$
*	$e^+e^- \to \tilde{\tau}\,\tilde{\tau}$	$\tilde{\tau} \to \tau\tilde{\gamma}$	(a)	acoplanar $\tau-\tau$
*	$e^+e^- \to \tilde{l}\,\tilde{l}$	$\tilde{l}$ stable		excess in μ pair cross section
	" $\to \tilde{q}\,\tilde{q}$	$\tilde{q} \to q\tilde{\gamma}$	(d)	acoplanar jet pair
	"	$\tilde{q} \to q\tilde{g}$	(i)	spherical events
	"	$\tilde{q} \to q\nu\tilde{\nu}$ or $q'l\tilde{\nu}$	(d)	acoplanar jets
*	$e\gamma \to \tilde{e}\,\tilde{\gamma}$	$\tilde{e} \to e\tilde{\gamma}$	(f)	single e
	$e^+e^- \to \gamma\tilde{\gamma}\tilde{\gamma}$	$\tilde{\gamma}$ invisible	(g)	single γ
*	$e^+e^- \to \tilde{\gamma}\,\tilde{z}$	$\tilde{z} \to l\bar{l}\tilde{\gamma}$	(a)	acoplanar $l-\bar{l}$
*	"	" $\to q\bar{q}\tilde{\gamma}$	(d,h)	acoplanar jet pair, single jets
*	"	" $\to q\bar{q}\tilde{g}$		"
	"	" $\to \nu\tilde{\nu}$		——
*	$e^+e^- \to \tilde{h}_1^0\,\tilde{h}_2^0$	$\tilde{h}_2^0 \to l\bar{l}\tilde{\gamma}$	(a)	acoplanar $l-\bar{l}$
*	"	" $\to q\bar{q}\tilde{\gamma}$	(d,h)	acoplanar jet pair, single jets
*	$e^+e^- \to \tilde{\chi}^+\,\tilde{\chi}^-$	$\tilde{\chi} \to l\nu\tilde{\gamma}$	(a,b)	acoplanar $l-\bar{l}'$
*	"	" $\to q\bar{q}'\tilde{\gamma}$	(d)	acoplanar jets
*	"	" $\to q\bar{q}'\tilde{g}$	(i)	spherical events (high $m_{\tilde{\chi}}$)
*	"	" $\to l\tilde{\nu}$	(a,b)	acoplanar $l-\bar{l}'$
*	"	$\tilde{\chi}$ stable		excess in μ pair cross section
*	$e\gamma \to \tilde{w}\,\tilde{\nu}$	$\tilde{w} \to l\tilde{\nu}$	(f)	single lepton
	$e^+e^- \to \gamma\tilde{\nu}\tilde{\nu}$	$\tilde{\nu}$ invisible	(g)	single γ

Table 2.1: List of supersymmetric reactions in e^+e^- collisions and their experimental signatures. The reactions investigated in this work are marked with a asterisk in the first column. The letters in the signature column refer to Tab. 2.2 on page 31 which gives an overview of the supersymmetric signatures in e^+e^- collisions. The gluino is assumed to decay into $q\bar{q}\tilde{\gamma}$. $\tilde{\chi}^{\pm}$ stands for an arbitrary mixture of wino and charged higgsino. 'Invisible' here means either stable or long lived or decaying into an 'invisible' final state.

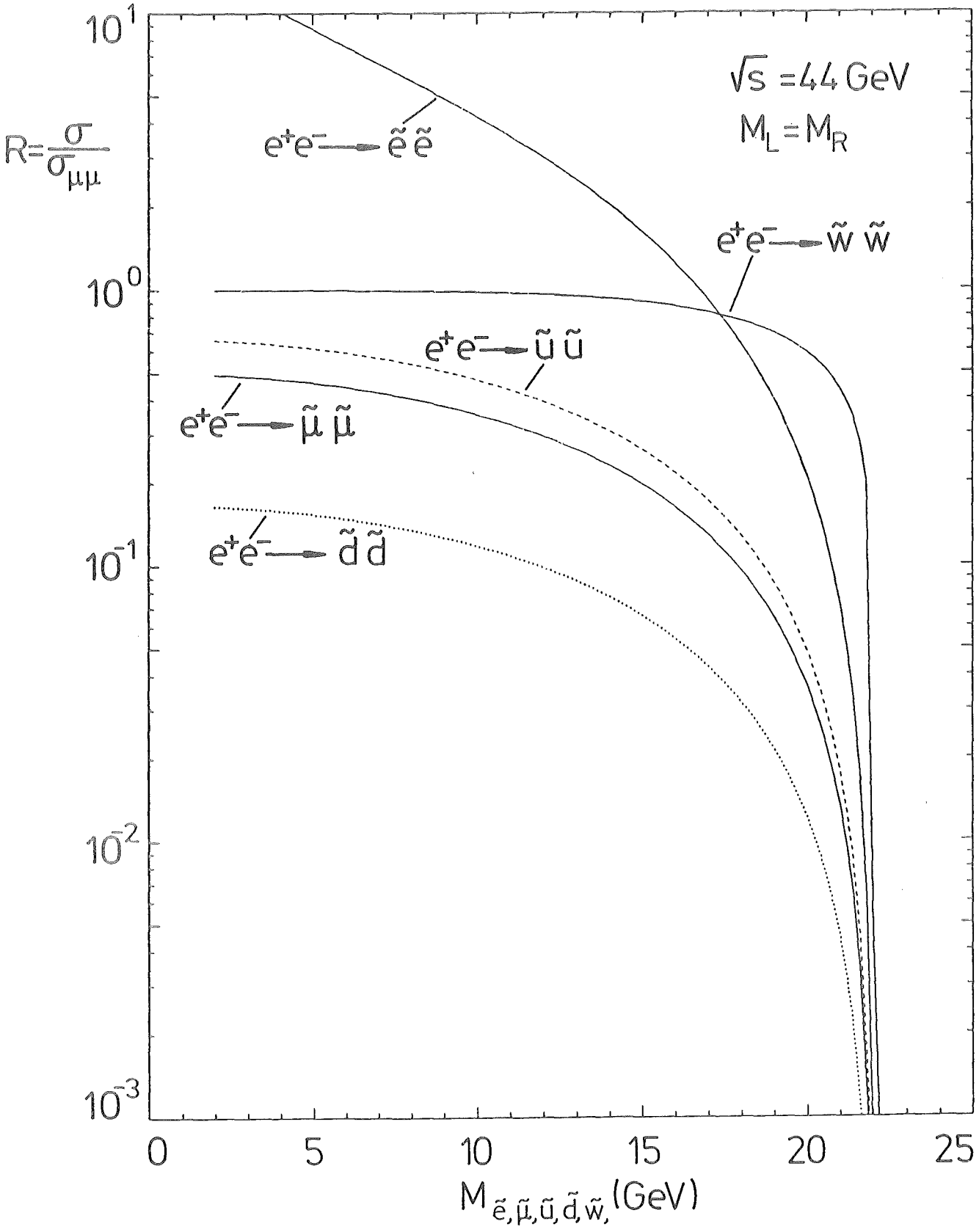

Figure 2.3: Lowest order cross section for pair production of supersymmetric particles at $\sqrt{s} = 44$ GeV assuming $m_{\tilde{\gamma}} = m_{\tilde{\nu}} = 0$ and mass degenerate partners of the left and right handed quarks and leptons.

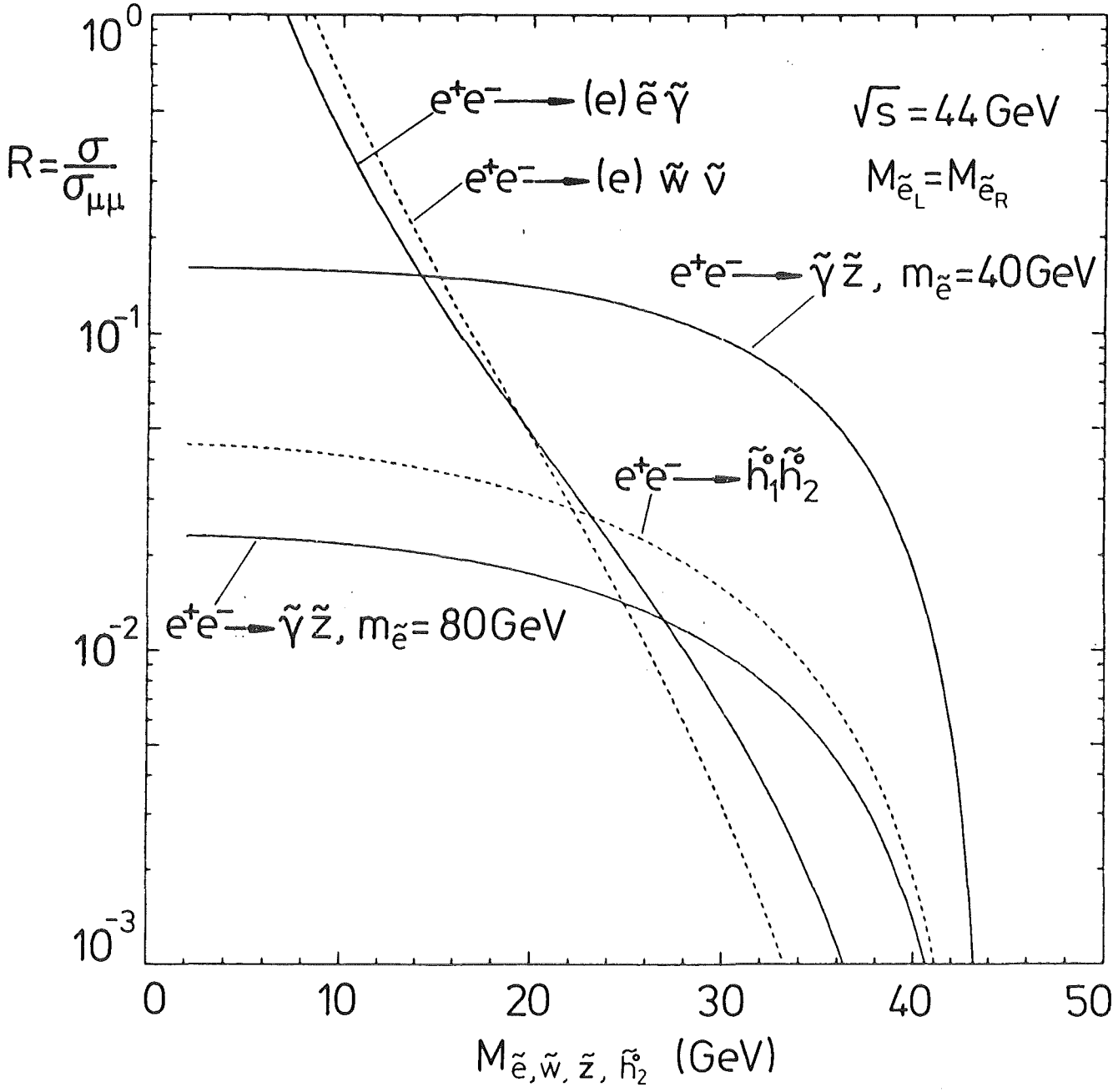

Figure 2.4: Production cross sections at $\sqrt{s}$ =44 GeV assuming $m_{\tilde{\gamma}} = m_{\tilde{\nu}} = 0$ and mass degenerate $\tilde{e}_L$ and $\tilde{e}_R$.

- $e^+e^- \rightarrow (e)\tilde{e}\tilde{\gamma}$ as function of $m_{\tilde{e}}$
- $e^+e^- \rightarrow (e)\tilde{w}\tilde{\nu}$ as function of $m_{\tilde{w}}$
- $e^+e^- \rightarrow \tilde{\gamma}\tilde{z}$ as function of $m_{\tilde{z}}$, $m_{\tilde{e}} = 40$ GeV
- $e^+e^- \rightarrow \tilde{\gamma}\tilde{z}$ as function of $m_{\tilde{z}}$, $m_{\tilde{e}} = 80$ GeV
- $e^+e^- \rightarrow \tilde{h}_1^0\tilde{h}_2^0$ as function of $m_{\tilde{h}_2^0}$, $m_{\tilde{h}_1^0} = 0$

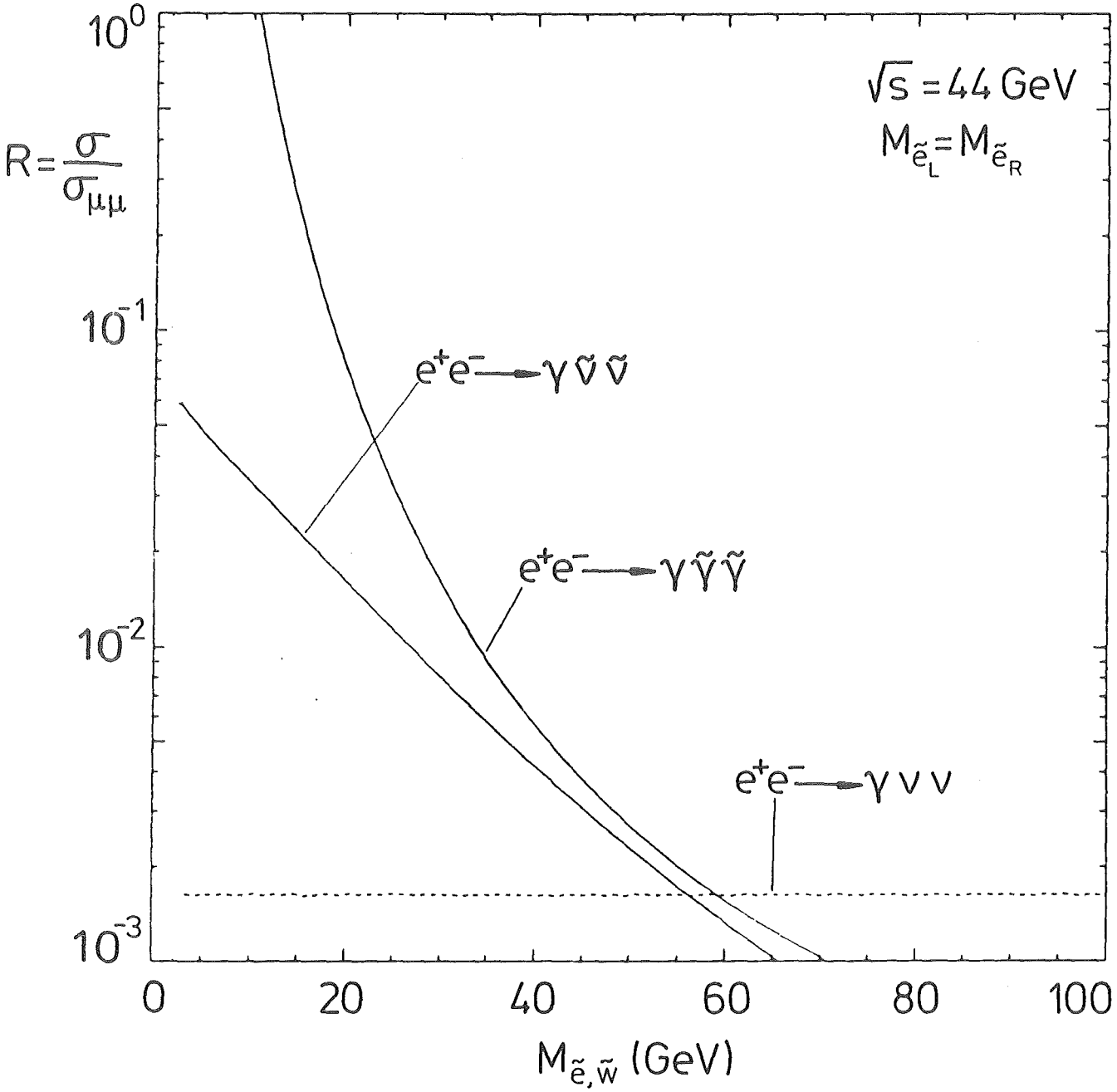

Figure 2.5: Production cross sections at $\sqrt{s}$ =44 GeV for the radiative processes

- $e^+e^- \rightarrow \gamma\tilde{\gamma}\tilde{\gamma}$ as function of $m_{\tilde{e}}$ for $x_{t,\gamma} > .05$, $|cos\Theta_\gamma| < .83$
- $e^+e^- \rightarrow \gamma\tilde{\nu}_e\tilde{\nu}_e$ as function of $m_{\tilde{w}}$ for $x_{t,\gamma} > .05$, $|cos\Theta_\gamma| < .83$

assuming $m_{\tilde{\gamma}} = m_{\tilde{\nu}} = 0$ and mass degenerate $\tilde{e}_L$ and $\tilde{e}_R$. For comparison, the dashed line indicates the cross section for radiative neutrino pair production $e^+e^- \rightarrow \gamma\nu\nu$ assuming 3 neutrino generations.

2.1 Scalar Leptons

2.1.1 Scalar Lepton Pair Production

Scalar leptons can be pair produced in e^+e^- interactions via single photon annihilation or in case of the scalar electron also via t-channel photino exchange:

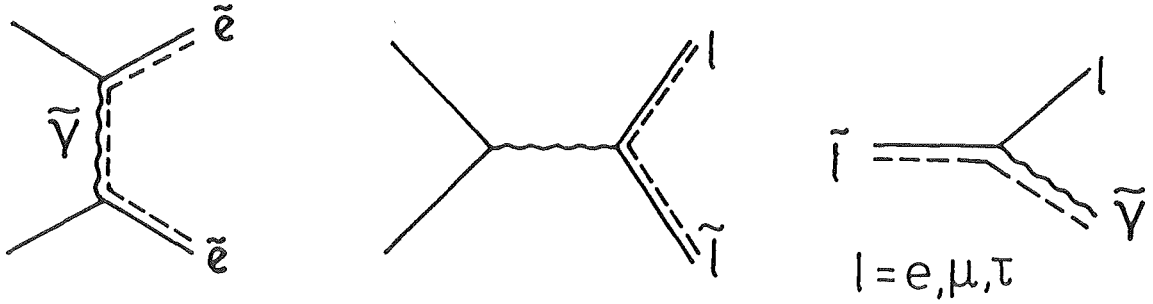

Figure 2.6: Scalar lepton pair production and decay

The total cross section is small for scalar τ's and μ's due to the β^3 p-wave suppression (see Equ. (2.1) and Fig. 2.2 on page 15), namely

$$\sigma(e^+e^- \to \tilde{l}_R^+\tilde{l}_R^-) = \frac{1}{4}\beta^3\sigma_{\mu\mu} \ , \qquad \text{for } l = \mu, \tau \tag{2.4}$$

but it is considerably enhanced for scalar electrons due to the $\tilde{\gamma}$ exchange amplitude (c.f. Fig. 2.3). If the partners of the right handed and left handed leptons are degenerate in mass, the cross section is doubled.

The decay of the sleptons into lepton and photino gives rise to an acoplanar pair of leptons, a very clean signature at e^+e^- machines. Background from the QED processes $e^+e^- \to ll\gamma$ and $e^+e^- \to ee\ ll$ can be easily rejected by requiring some minimum acoplanarity (i.e. some minimum p_t) and no additional particles in the detector. The case of acoplanar τ final states is somewhat more difficult since each τ decay produces at least one invisible neutrino. However, the mass of the τ is small compared to the beam energy so that the visible decay products follow closely the original τ direction. Therefore the acoplanarity of the observed τ decay products is still a good cut quantity to seperate $e^+e^- \to \tilde{\tau}\tilde{\tau}$ from $e^+e^- \to \tau\tau$.

2.1.2 Single Production of a Scalar Electron

Higher $\tilde{e}$ masses up to $\sqrt{s}$ - $m_{\tilde{\gamma}}$ can be probed in the single production of a scalar electron [21]:

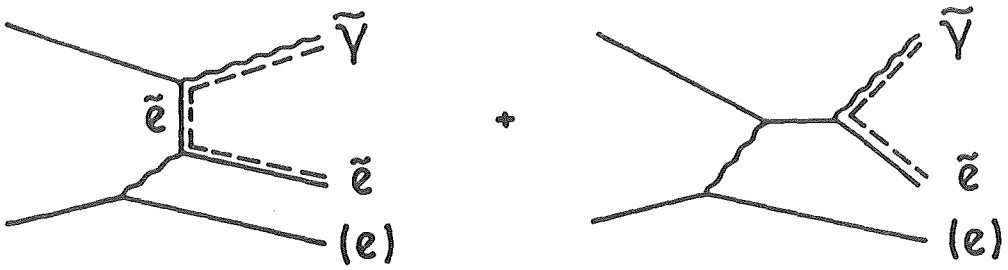

Figure 2.7: Dominant diagrams for single scalar electron production if the final electron is scattered under small angle ('virtual Compton' configuration).

Here one of the beam electron radiates a quasi real photon which interacts with an electron of the other beam producing a scalar electron and a photino, either by t-channel $\tilde{e}$ exchange or via a virtual electron in the s-channel (the supersymmetric analogue of Compton scattering). The electron is scattered at very small angles and escapes unobserved down the beam pipe. The decay of the $\tilde{e}$ gives rise to an energetic electron distributed almost isotropically for high $\tilde{e}$ masses plus an unobserved photino. Therefore the signature for this reaction is a single hard electron from the $\tilde{e}$ decay and nothing else in the detector.

The cross section for single scalar electron production has been computed first by M.K. Gaillard et al. [21] for massless photinos using the equivalent photon approximation [22] to compute the diagrams in Fig. 2.7:

$$\sigma(e^+e^- \rightarrow (e)\tilde{e}\tilde{\gamma}) \simeq \int_x^1 dy F(y)\sigma(e\gamma \rightarrow \tilde{e}\tilde{\gamma}, \hat{s}) \tag{2.5}$$

where

$$F(y) = \frac{\alpha}{\pi y}[1 + (1-y)^2] ln \frac{E_{beam}}{m_e}, \qquad x = \frac{(m_{\tilde{e}} + m_{\tilde{\gamma}})^2}{s}, \qquad \hat{s} = y \cdot s$$

The cross section for $e\gamma \rightarrow \tilde{e}\tilde{\gamma}$ for arbitrary photino masses can be found in appendix A.

Background for the single electron topology can come from the QED version of this process: the virtual compton scattering configuration of Bhabha scattering $e^+e^- \rightarrow (e)e\gamma$ where one electron is scattered under small angle and the photon escapes through holes in the electromagnetic calorimetry of the detector. The photon in the competing QED process, however, must balance the transverse momentum

of the large angle electron. Therefore, since the single electron from the $\tilde{e}$ decay is very energetic in the mass region of interest ($m_{\tilde{e}} > E_{beam}$), only calorimeter holes under relatively large angle with respect to the beam direction are dangerous.

2.1.3 Single Photons from Photino Pair Production

Even higher scalar electron masses can be reached by tagging (invisible) photino pair production by a photon radiated in the initial state:

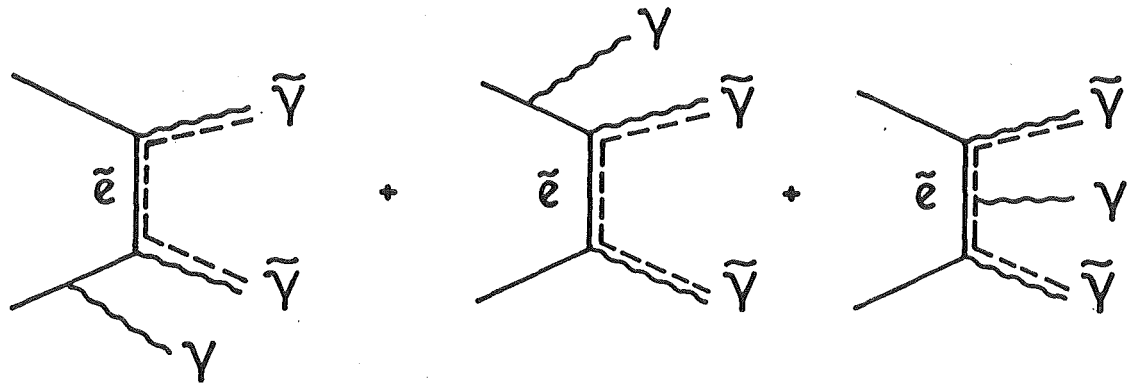

Figure 2.8: Diagrams for radiative photino pair production. The third amplitude can be safely negelected since here the (massive) $\tilde{e}$ propagator enters twice (as done in (2.6)).

Since the $\tilde{e}$ occurs as a t-channel propagator, this process is sensitive to scalar electron masses even above the e^+e^- center of mass energy. The cross section for this process is [24]

$$\frac{\mathrm{d}^2\sigma(e^+e^- \to \gamma X)}{\mathrm{d}x\mathrm{d}y} = \frac{2\alpha}{\pi}\frac{1}{x(1-y^2)}\,\sigma(e^+e^- \to X, \hat{s}) \qquad (2.6)$$

with $x = E_\gamma/E_{beam}$, $y = cos\theta_\gamma$, and $\hat{s} = s(1-x)$. The cross section for $e^+e^- \to \tilde{\gamma}\,\tilde{\gamma}$ is given in appendix A.

The experimental signature is a single photon in the detector, very similar to the ν-counting reaction $e^+e^- \to \gamma\nu\nu$. The photon spectrum is of the Bremsstrahlung type peaked at low energies and small angles with respect to the electron beam. This requires a low trigger threshold for single photons and a large acceptance for the 'trigger photon'. In order to be able to reject QED background from radiative Bhabha scattering and photon pair production hermetic calorimetry down to small angles is essential. The ultimate background for this reaction are single photons from radiative neutrino pair production.

2.2 Scalar Quarks

Scalar quarks can be pair produced in e^+e^- one photon annihilation in the same way as scalar leptons with a cross section

$$\sigma(e^+e^- \to \tilde{q}_R\tilde{q}_R) = 3\ Q^2\frac{1}{4}\beta^3\sigma_{\mu\mu}\ , \qquad |Q| = \frac{1}{3}\ \text{or}\ \frac{2}{3} \tag{2.7}$$

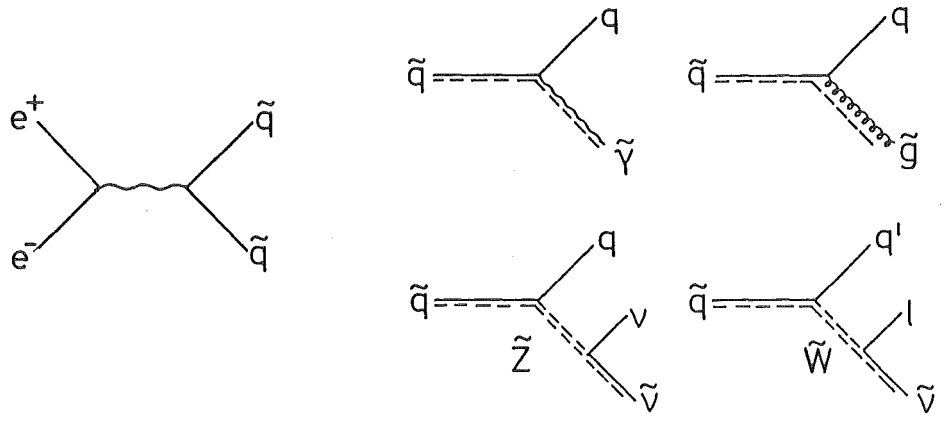

Figure 2.9: Feynman diagram for scalar quark pair production and decay.

This cross section should be doubled in case of degeneracy between the partners of the left and right handed quarks.

The decay and thus the experimental signatures depend on the supersymmetric mass hierarchy:

heavy gluino ($m_{\tilde{g}} > m_{\tilde{q}}$):
The scalar quark decays into quark and photino. The signature then is an acoplanar pair of jets.

light gluino ($m_{\tilde{g}} < m_{\tilde{q}}$):
If the decay into quark and gluino is allowed kinematically it will be dominant because the strong $\tilde{q}q\tilde{g}$ coupling is large compared to the $\tilde{q}q\tilde{\gamma}$ electromagnetic coupling. With the subsequent decay $\tilde{g} \to q\bar{q}\tilde{\gamma}$ the final state will consist of 6 'jets' with relatively little missing energy. For a heavy scalar quark this leads to rather spherical multihadronic final states.

light scalar neutrino ($m_{\tilde{\nu}} < m_{\tilde{q}}$):
If both the photino and gluino mass lie above the scalar quark mass and if the scalar neutrino is light, three body decays via wino or zino exchange are expected. In the first case one would observe acoplanar jet pairs with a large amount of missing energy. If the decay proceeds mainly via a wino the signature is practically the same as for a new quark flavour. Note, however, that the production cross section is very small compared to a new spin 1/2 quark (c.f. Fig. 2.2 on page 15).

2.3 Gauginos

The weak vector bosons $W^{\pm}$ and Z^0 are too heavy to be produced at present energy e^+e^- colliders. On the other hand, many models predict their supersymmetric partners, the wino $\tilde{w}$ and zino $\tilde{z}$, to be lighter. For definiteness, here it is assumed that the $\tilde{z}$ and $\tilde{w}$ to are unmixed.

2.3.1 Winos

2.3.1.1 Pair Production

Winos can be pair produced via one photon annihilation and via t-channel sneutrino exchange:

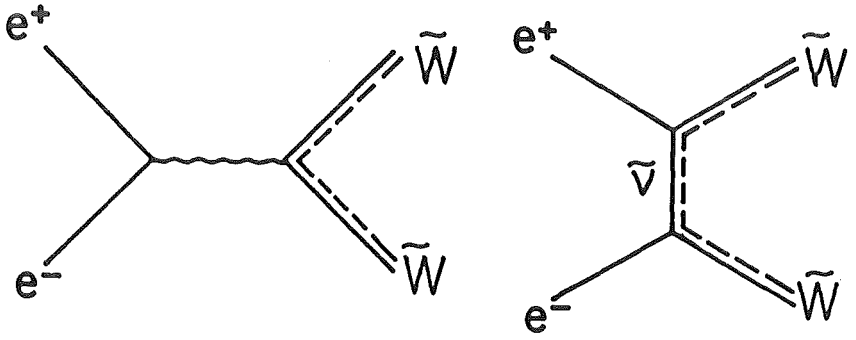

Figure 2.10: Feynman diagram for wino pair production

with a cross section of at least (neglecting $\tilde{\nu}$ exchange)

$$\sigma(e^+e^- \to \gamma \to \tilde{w}^+\tilde{w}^-) = \frac{\beta(3-\beta^2)}{2}\,\sigma_{\mu\mu}. \tag{2.8}$$

The contribution from $\tilde{\nu}$ exchange, which of course depends on the $\tilde{\nu}$ mass, is always positive as the interference between the γ and $\tilde{\nu}$ exchange amplitudes is always constructive [27]. The full expression for the cross section can be found in

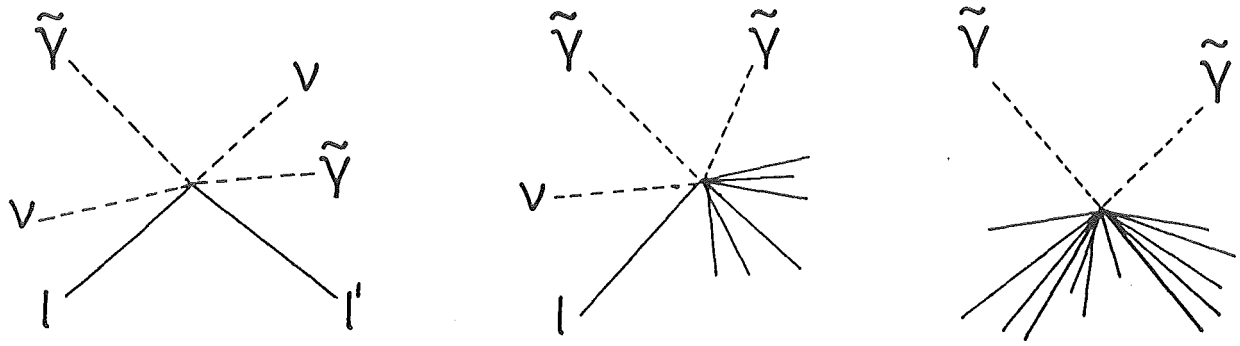

Figure 2.11: Signatures of wino pair production and three body decay.

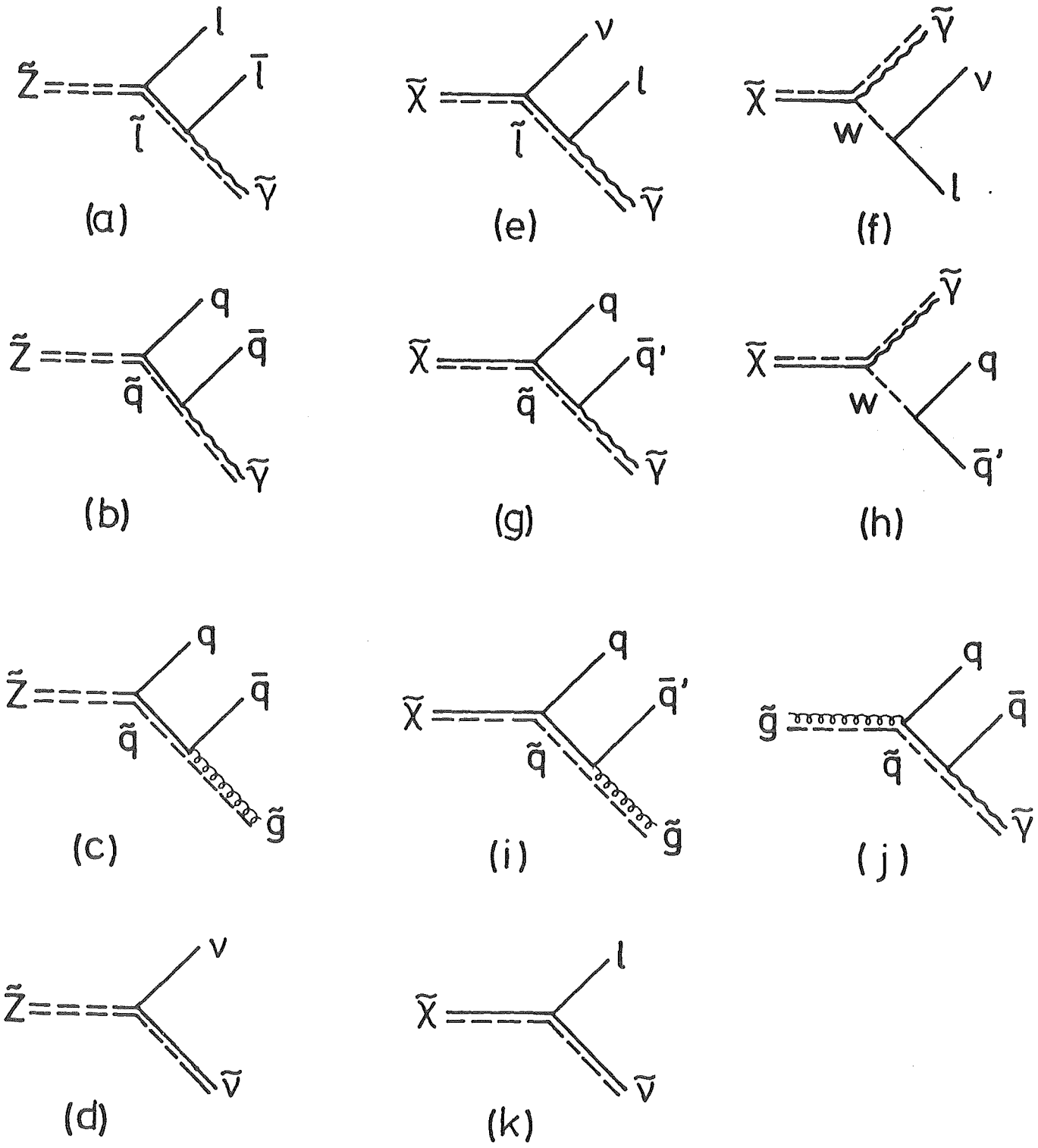

Figure 2.12: Possible $\tilde{z}$ and $\tilde{w}$ decay modes ($\tilde{\chi}$ stands for a chargino, a mixture of $\tilde{w}$ and charged higggsino $\tilde{h}^{\pm}$). For a discussion of the various decay modes see text.

appendix A. Since the wino is a spin 1/2 particle, its production cross section is considerably larger than for scalar quarks or leptons.

The experimental signature for this reaction of course depends on the decay modes of the wino. Depending on the unknown supersymmetric mass spectrum, various scenarios are possible (c.f. Fig. 2.12):

heavy gluino ($m_{\tilde{g}} > m_{\tilde{w}}$), heavy sneutrino ($m_{\tilde{\nu}} > m_{\tilde{w}}$):
The wino decays into $l\nu\tilde{\gamma}$ or $q\bar{q}'\tilde{\gamma}$ via W or via scalar exchange (Fig. 2.12 e-h) with a leptonic branching fraction of O(10%) per lepton generation. A general signature is missing energy and momentum carried away by photinos and neutrinos (Fig. 2.11). In particular one expects acoplanar lepton pairs (not necessarily of the same flavour) and hadronic final states with missing energy/momentum.

light gluino ($m_{\tilde{g}} < m_{\tilde{w}}$):
The wino decays dominantly hadronically into $q\bar{q}'\tilde{g}$, followed by $\tilde{g} \rightarrow q\bar{q}\tilde{\gamma}$ (Fig. 2.12 i,j). Winos are pair produced, so that one has 8 'jets' in the final state resulting in spherical events with relatively small missing p_t.

light sneutrino ($m_{\tilde{\nu}} < m_{\tilde{w}}$):
Perhaps the scalar neutrino is light, possibly it even is the lightest supersymmetric particle [26]. In this case the winos decays exclusively into a two body $l\tilde{\nu}$ final state (Fig. 2.12k) with the sneutrino escaping unseen. Wino pair production then gives acoplanar lepton final states.

2.3.1.2 Single Production

If the scalar neutrino is light, wino masses above the beam energy can be probed by the single production of winos in $e\gamma$ collisions very similar to the single production of scalar electrons discussed above.

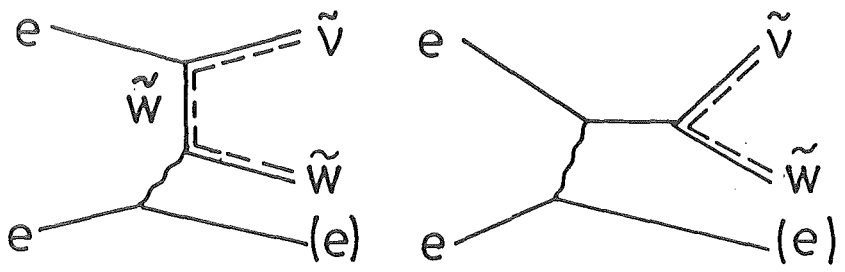

Figure 2.13: Dominant diagrams for single wino production if the final electron is scattered under small angle.

The cross section for $e^+e^- \rightarrow (e)\tilde{w}\ \tilde{\nu}$ can be computed from $\sigma(e\gamma \rightarrow \tilde{w}\tilde{\nu})$ using the equivalent photon approximation (2.5). The $e\gamma \rightarrow \tilde{w}\tilde{\nu}$ cross section can be found in appendix A.

As in the case of single $\tilde{e}$ production the electron is scattered under small angle and escapes unobserved along the beam pipe and the signature is a single hard lepton (e, μ, or τ) together with an escaping sneutrino from the wino decay $\tilde{w} \rightarrow l\tilde{\nu}$.

2.3.1.3 Radiative $\tilde{\nu}$ Pair Production via $\tilde{w}$ Exchange

Even if the wino mass lies above the available c.m. energy wino exchange would affect the rate of radiative $\tilde{\nu}$ pair production via $\tilde{w}$ and Z^0 exchange [36]:

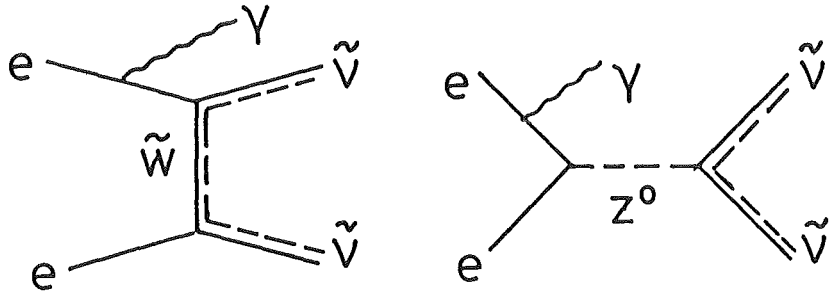

Figure 2.14: Radiative pair production of scalar neutrinos. A third diagram with the photon attached to the exchanged wino may be safely neglected for higher wino masses as here the wino propagator $\propto 1/m_{\tilde{w}}^4$ enters twice.

As in the case of $e^+e^- \rightarrow\gamma\tilde{\gamma}\tilde{\gamma}$ the cross section can be computed from $e^+e^- \rightarrow \tilde{\nu}\ \tilde{\nu}$ (as given in appendix A) using the factorization relation (2.6).

2.3.2 Zinos

In e^+e^- interactions zinos can be produced together with a $\tilde{\gamma}$ via $\tilde{e}$ exchange.

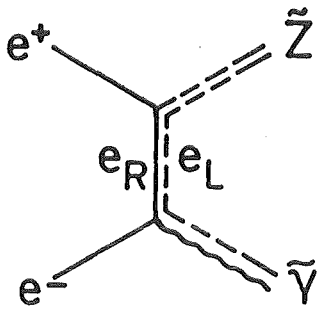

Figure 2.15: Feynman diagram for single zino production

The cross section depends on $\tilde{z}$, $\tilde{\gamma}$, and $\tilde{e}$ masses and can be found in Appendix A.

Similar to the wino case various decay scenarios are possible:

heavy gluino ($m_{\tilde{g}} > m_{\tilde{z}}$), heavy sneutrino ($m_{\tilde{\nu}} > m_{\tilde{z}}$):
In this case the zino decays via scalar exchange into an fermion anti-fermion pair and a photino (diagram a,b in Fig. 2.12). In case of equal scalar quark and lepton masses and a zino mass far above the $b\bar{b}$ threshold one expects a leptonic (hadronic) branching fraction of 3*13 % (60 %).

light gluino ($m_{\tilde{g}} < m_{\tilde{z}}$):
In this case the dominant zino decay would be hadronically into $q\bar{q}\tilde{g}$ followed by $\tilde{g} \rightarrow q\bar{q}\tilde{\gamma}$ (diagrams c,j in Fig. 2.12), due to the stronger hadronic $\tilde{q}q\tilde{g}$ coupling.

light sneutrino ($m_{\tilde{\nu}} < m_{\tilde{z}}$):
If the $\tilde{\nu}$ is light the zino would decay exclusively into an invisible $\tilde{\nu}\nu$ final state (Fig. 2.12d) and the only possibility to put limits on its mass would be initial state radiation tagging of zino production $e^+e^- \rightarrow \gamma\tilde{\gamma}\tilde{z}$ similar to $e^+e^- \rightarrow \gamma\tilde{\gamma}\tilde{\gamma}$ discussed above.

The process $e^+e^- \rightarrow \tilde{\gamma}\tilde{z}$ followed by the decay $\tilde{z} \rightarrow e^+e^-\tilde{\gamma}$ leads to the signature of an acoplanar electron pair with momentum and energy carried away by the two unobserved photinos. In analogy, the decay $\tilde{z} \rightarrow q\bar{q}\tilde{\gamma}$ gives rise to a pair of acoplanar jets which for smaller zino masses are boosted into a single hemisphere giving rise to one handed 'zen' like event topologies. If the zino decays predominantly into $q\bar{q}\tilde{g}$ the average momentum of the decay photino is reduced but the general feature of missing energy and momentum, although less distinctive for high zino masses, is maintained. Thus signatures of zino production and decay in e^+e^- collisions will be jets or lepton pairs with missing energy and momentum.

2.4 Higgsinos

The lightest charginos and neutralinos may be mainly gaugino like or higgsino like or anything in between. After having discussed the case of pure gauginos in the previous section we will now consider the other extreme case, namely production and decay of pure higgsinos.

2.4.1 Charged Higgsinos

Charged higgsinos can be pair produced via one photon annihilation with the same cross sections as a new heavy lepton.

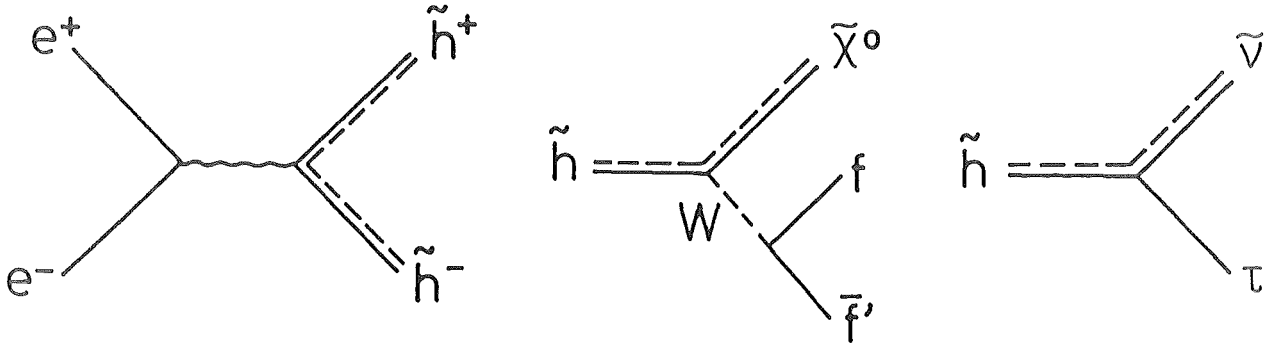

Figure 2.16: Feynman diagram for pair production and the potential decay modes of a charged higgsino.

The $\tilde{\nu}$ exchange amplitude in pair production as well as single production and the higgsino contribution to $\tilde{\nu}$ pair production are negligible due to the small $He\nu = \tilde{h}e\tilde{\nu}$ coupling which is proportional to m_e. For the $\tilde{h}^{\pm}$ decay one has to consider two cases depending on the supersymmetric mass hierarchy:

heavy sneutrino ($m_{\tilde{\nu}} > m_{\tilde{h}}$):
The decay into the lightest neutralino $\tilde{\chi}_1^0$, be it photino or a neutral higgsino, and a virtual W will be dominant due to the small $\tilde{h}f\bar{f}$ coupling. This will lead to acoplanar lepton pairs and hadronic final states with missing energy/momentum in the same way as wino pair production discussed in the previous section. Due to the small $\tilde{h}q\bar{q}$ coupling this will be the dominant decay even if the gluino is lighter than the $\tilde{h}^{\pm}$.

light sneutrino ($m_{\tilde{\nu}} < m_{\tilde{h}}$):
If the scalar neutrino is light the two body decay $\tilde{h} \rightarrow l\tilde{\nu}$ is allowed and will be dominant. As the decay width $\Gamma(\tilde{h} \rightarrow l\tilde{\nu})$ is proportional to m_l^2 the decay $\tilde{h} \rightarrow \tau\tilde{\nu}_\tau$ will be dominant, yielding acoplanar tau pair events.

2.4.2 Neutral Higgsinos

If the two lowest lying neutralinos are higgsinos (or mostly higgsino like) they can be produced via a virtual Z^0 [37]

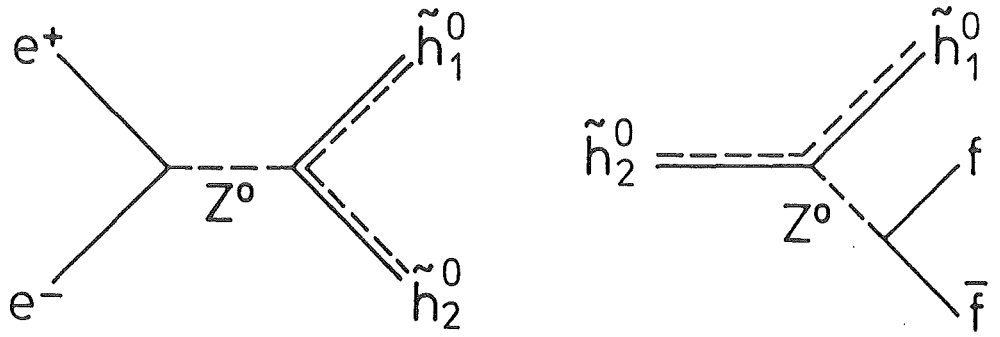

Figure 2.17: Associated production of the lightest and second lightest neutral higgsino. The heavier $\tilde{h}_2^0$ decays into the lighter $\tilde{h}_1^0$ and a virtual Z^0.

An advantage of this reaction (as compared to $e^+e^- \rightarrow \tilde{\gamma}\,\tilde{z}$) is that the production rate does not depend on the unknown scalar electron mass.

The heavier $\tilde{h}_2^0$ will decay into the $\tilde{h}_1^0$ and a virtual Z^0 giving rise to a pair of leptons and jets. Note that this will be the only decay mode of a purely higgsino like $\tilde{h}_2^0$ even if the gluino or scalar neutrino is lighter than the $\tilde{h}_2^0$. The $\tilde{h}q\bar{q}$ coupling is small and scalar neutrinos and higgsinos decouple (at tree level) in case of massless neutrinos. A small gaugino admixture in $\tilde{h}_2^0$, however, may cause the decays discussed in section 2.3.2 to become relevant. Above (below) $b\bar{b}$ threshold (and for a light $\tilde{h}_1^0$) one expects an hadronic branching ratio of $\sim$ 70 % (64 %) and a leptonic one of 3.4 % (4.1 %) per lepton generation. If the lighter higgsino is invisible (either being stable as the LSP or being long lived or decaying into an invisible final state such as $\nu\tilde{\nu}$) the experimantal signature of $e^+e^- \rightarrow \tilde{h}_1^0$ $\tilde{h}_2^0$ is identical to the one of single zino production $e^+e^- \rightarrow \tilde{\gamma}\,\tilde{z}$ discussed before. It ranges from spectacular one sided monojet like events for a relatively low mass $\tilde{h}_2^0$ to acoplanar jet pairs with missing energy/momentum for $m_{\tilde{h}_2^0} \lesssim \sqrt{s}$.

2.5 Summary

After having discussed a wide variety of supersymmetric reactions in e^+e^- interactions we observe that many processes have common experimental signatures. Table 2.2 summarizes the characteristic supersymmetric signatures together with the relevant background reactions from standard processes.

	signature	$e^+e^- \rightarrow$ SUSY final state
(a)	acoplanar lepton pairs (same flavour)	$e^+e^- \rightarrow \tilde{l}\tilde{l}, \tilde{\gamma}\tilde{z}, \tilde{h}_1^0\tilde{h}_2^0, \tilde{\chi}^+\tilde{\chi}^-$
(b)	acoplanar lepton pairs (different flavour)	$e^+e^- \rightarrow \tilde{\chi}^+\tilde{\chi}^-$
(c)	acoplanar photons	$e^+e^- \rightarrow \tilde{\gamma}\,\tilde{\gamma}$, unstable $\tilde{\gamma}$
(d)	acoplanar jets	$e^+e^- \rightarrow \tilde{q}\tilde{q}, \tilde{\gamma}\tilde{z}, \tilde{h}_1^0\tilde{h}_2^0, \tilde{\chi}^+\tilde{\chi}^-$
(e)	lepton + jets	$e^+e^- \rightarrow \tilde{\chi}^+\tilde{\chi}^-$
(f)	single electrons	$e^+e^- \rightarrow (e)\tilde{e}\tilde{\gamma},\ (e)\tilde{w}\tilde{\nu}$
(g)	single photons	$e^+e^- \rightarrow \gamma\tilde{\gamma}\tilde{\gamma},\ \gamma\tilde{\nu}\tilde{\nu}$
(h)	single jets	$e^+e^- \rightarrow \tilde{\gamma}\tilde{z},\ \tilde{\chi}_1^0\tilde{\chi}_2^0$
(i)	aplanar (spherical) events	$e^+e^- \rightarrow \tilde{q}\tilde{q},\ \tilde{\chi}^+\tilde{\chi}^-$

	signature	$e^+e^- \rightarrow$ background reactions
(a)	acoplanar lepton pairs (same flavour)	$e^+e^- \rightarrow ll(\gamma), (ee)ll$
(b)	acoplanar lepton pairs (different flavour)	$e^+e^- \rightarrow \tau\tau(\gamma), \tau\tau\gamma, (e)e(l)l$
(c)	acoplanar photons	$e^+e^- \rightarrow \gamma\gamma(\gamma)$
(d)	acoplanar jets	$e^+e^- \rightarrow q\bar{q}(\gamma), (ee)q\bar{q}$
(e)	lepton + jets	$e^+e^- \rightarrow b\bar{b}, (e)eq\bar{q}$
(f)	single electrons	$e^+e^- \rightarrow (e)e(\gamma)$
(g)	single photons	$e^+e^- \rightarrow (ee)\gamma, (\gamma\gamma)\gamma$, cosmic showers
(h)	single jets	$e^+e^- \rightarrow q\bar{q}(\gamma)$
(i)	aplanar (spherical) events	$e^+e^- \rightarrow q\bar{q}g, q\bar{q}gg$ (higher order QCD)

Table 2.2: Typical signatures of supersymmetric processes in e^+e^- interactions and the most important backgrounds from conventional sources. Undetected particles are put in brackets.

Chapter 3

Experimental Apparatus

The data was taken using the CELLO detector at the PETRA (Positron Electron Tandem Ring Accelerator) electron positron storage ring at DESY (Deutsches Elektronen SYnchroton) in Hamburg.

3.1 PETRA

The electron positron storage ring PETRA was built in the years 1976 to 1978. It has been designed for a peak c.m. energy around 40 to 50 GeV with luminosities in the order of $10^{31}\ cm^{-2}s^{-1}$. The data used in this analysis was accumulated in the period from spring 1983 until end of 1985 after a major energy increase made possible by the installation of additional RF cavities in fall of 1982. In April 1984 PETRA reached the world record e^+e^- collision energy of 46.78 GeV. Until the startup of TRISTAN it remains the world's highest energy e^+e^- collider.

The general layout can be seen in Fig. 3.1. The ring with a circumference of 2.3 kilometers and a magnet bending radius of 192 meters has four interaction regions. The radius of curvature is 256 meters. Electrons are initially accelerated in LINAC I and then injected into the DESY synchroton where they are accelerated up to the PETRA injection energy of 7 GeV and then transfered into PETRA. Positrons are created in LINAC II and are accumulated in PIA (Positron Intensity Accumulator). Then like the electrons they are injected via DESY into PETRA. When electron and positron injection is complete the bunches are accelerated from injection energy to the desired beam energy. Typical times for injection and energy ramping are 15 to 20 minutes. The beams are kept for luminosity running for 2 to 4 hours with gradually decreasing luminosity. Then the beams are dumped and a new fill is prepared.

In total CELLO has accumulated an integrated luminosity of 48.6 pb^{-1} at c.m. energies above 40 GeV. Since the beginning of 1986 PETRA has collected another 90 pb^{-1} at $\sqrt{s} = 35$ GeV. The reason for going back to this reduced

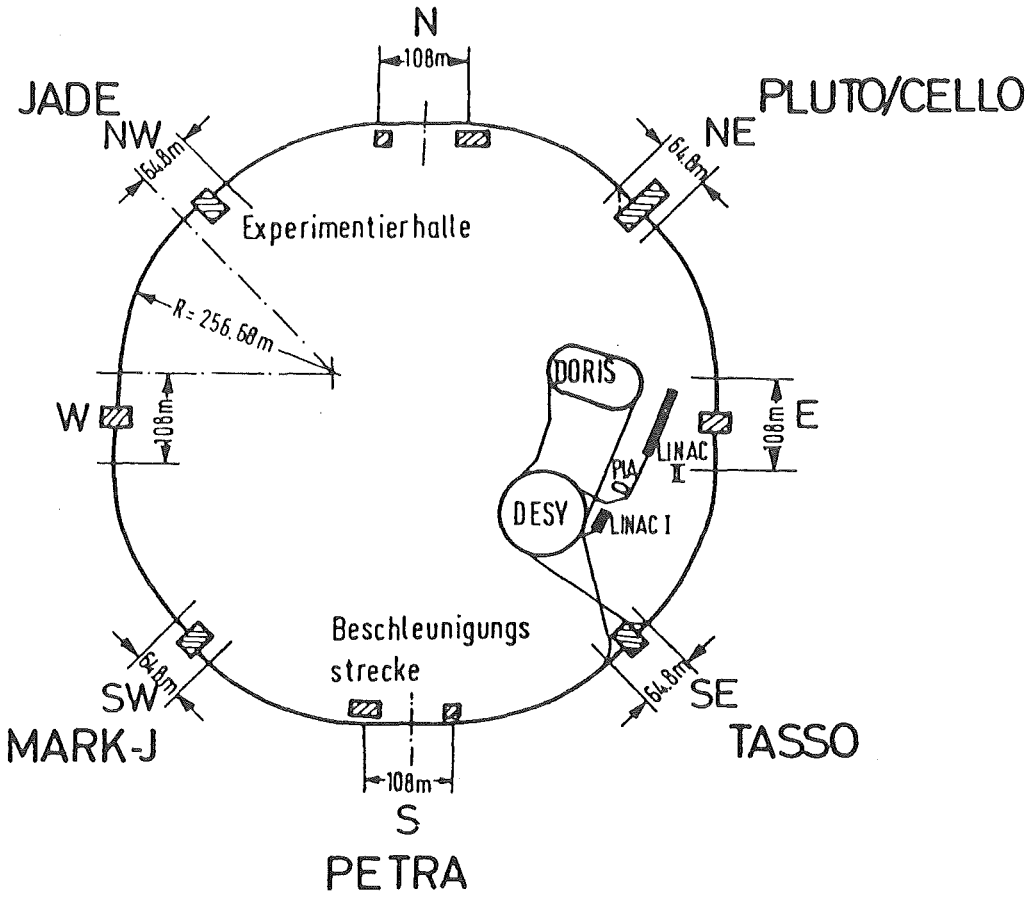

Figure 3.1: Accelerators on the DESY site

energy was a more than threefold increase in luminosity compared to the high energy running as well as greatly improved background conditions in the detector's tracking chambers.

3.2 CELLO

The objective of a colliding beam detector is to measure the particles emerging from e^+e^- interactions as completely and as precisely as possible, and to identify different particle species (hadrons, electrons, muons, photons). A real detector is always a compromise taking into account partly contradicting requirements, the technological possibilities, and the finite amount of funds available.

The good experience with the MARK I and PLUTO detectors at the SPEAR and DORIS storage rings have made the cylinder symmetrical arrangement with a solenoidal magnetic field parallel to the beam axis the so called standard detector. It features

- position measurement by cylindrical chambers inside the solenoidal magnet for the measurement of direction and momentum of charged particles.

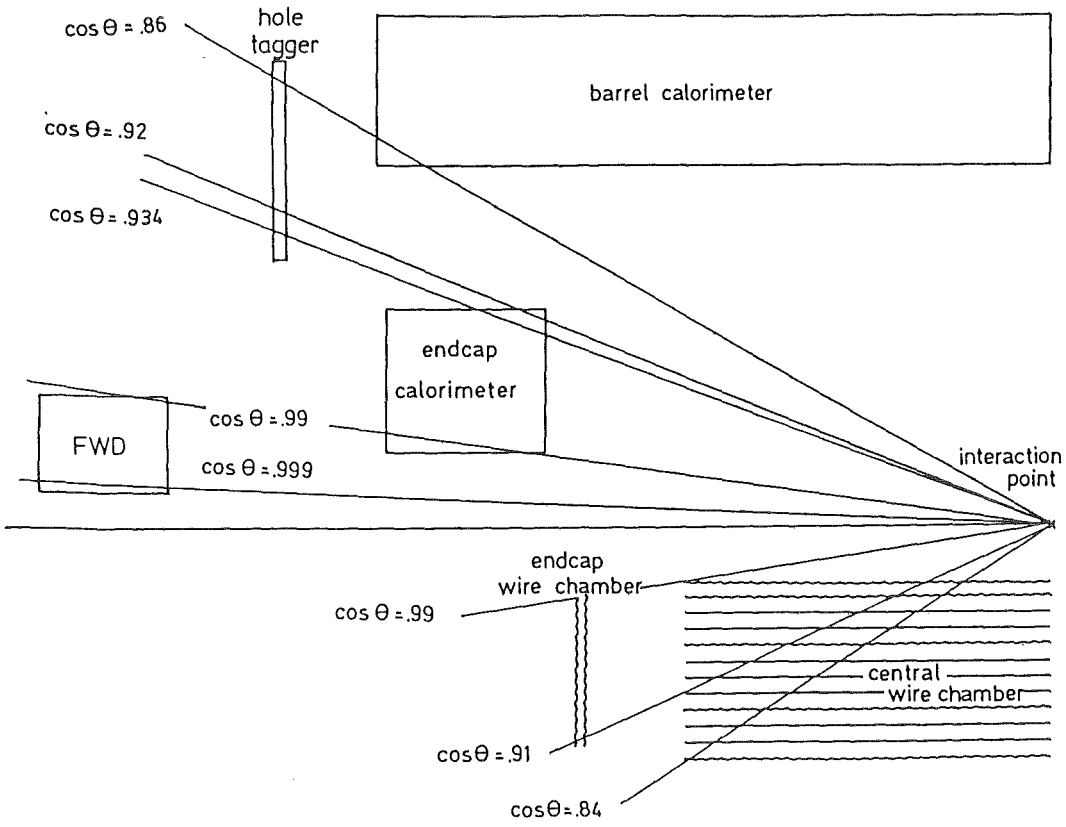

Figure 3.2: Overview of the CELLO solid angle coverage for tracking (lower half) and calorimetry (upper half). The wiggled lines represent proprtional chambers, the others are drift chambers. The coverage of the barrel and end cap liquid argon calorimeters is complemented by the 'hole tagger' veto counters. At small angles a lead glass array forward detector (FWD) extends calorimetry down to 50 mrad.

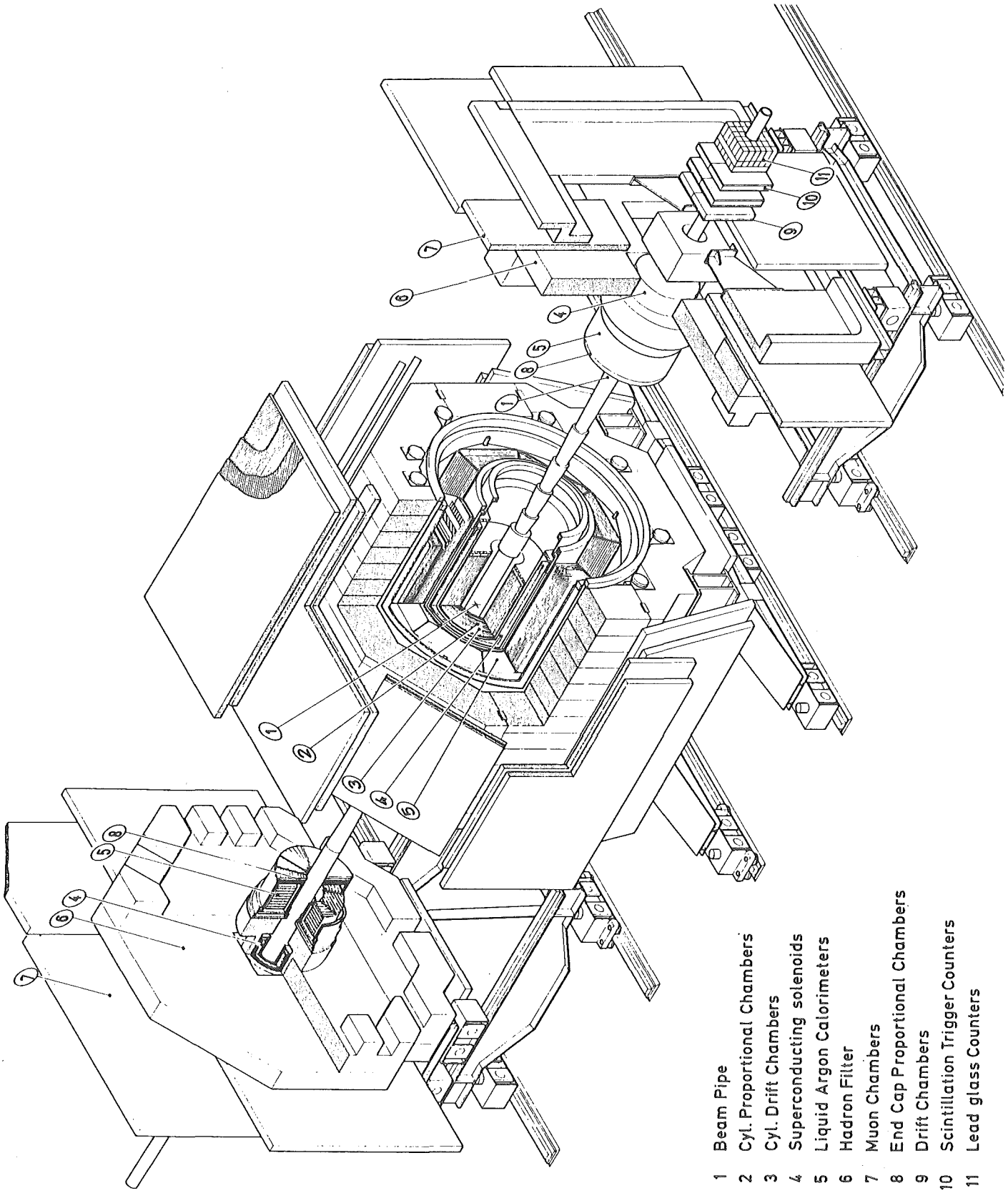

Figure 3.3: Perspective view of the CELLO detector

- an electromagnetic calorimeter for direction and energy measurement of photons and for the separation of electrons from hadrons on the basis of their different showering behaviour.
- a hadron absorber surrounded by chambers for the detection of non showering muons.

The design of the CELLO e^+e^- detector [56] follows these principles. Emphasis is put on photon identification and lepton hadron separation in combination with a large and homogeneous solid angle coverage at the expense of only limited hadron identification capabilities. Other important features are an hermetic electromagnetic calorimetry down to angles of 50 mrad with respect to the beam direction and the ability to trigger on an energy deposition as low as 2 GeV in a single calorimter module. Figure 3.2 gives an overview of the solid angle coverage of CELLO for tracking and calorimetry. The good detection capabilities for leptons and escaping ν-like particles make CELLO ideally suited for new particle searches.

Figure 3.3 shows an perspective view of the CELLO detector. In the following I will give a brief description of the important features of the detector components. A more complete discussion can be found in Ref. [56].

3.2.1 Tracking

Charged particle tracking is done by a set of interleaved drift and proportional chambers in a solenoidal magnetic field of 1.3 T produced by a thin (1/2 radiation length) superconducting coil. The chamber properties are summarized in Table 3.1. The beam pipe has a thickness of 4 % of a radiation length corresponding to a photon conversion probability of $\sim$ 3.2 %.

The drift chambers provide an accurate position determination ($\sigma \sim 380\mu m$) in the $r\phi$ plane perpendicular to the beam and thus an accurate momentum measurement.

The five proportional chambers feature anode wires spaced at 2.09 to 2.86 mm and two planes of cathode strips with analog readout running at 90° and 30° with respect to the anodes. This allows an unambigious reconstruction of space points and a good track separation in high multiplicity events. The spatial resolution in z direction parallel to the beam is $\sigma \sim 600\mu m$ facilitating a good polar angle and invariant mass resolution.

Track angular resolutions are 2 mrad in both polar and azimuthal angle and the momentum resolution obtained including the interaction vertex can be described by $\Delta p_t/p_t = 2\%\ p_t$ (p in GeV.) The resolution figures are averaged values determined from Bhabha scattering events collected over a long running period.

layer	type	radius (cm)	cell width (mm)	acceptance $\lvert\cos\Theta\rvert$	material $10^{-4}X_0$
1	DC	10.9	5.35	-	60
2	DC	11.4	5.60	-	60
3	PC	17.0	2.09	-	34
4	PC	21.0	2.58	-	34
5	DC	25.5	15.41	.974	8
6	DC	30.4	14.92	.964	8
7	PC	35.7	2.19	.951	34
8	DC	40.2	15.03	.939	8
9	DC	45.1	14.76	.925	8
10	DC	50.0	15.10	.910	8
11	PC	55.3	2.26	.893	34
12	DC	59.8	14.68	.878	8
13	DC	64.7	15.88	.862	8
14	PC	70.0	2.86	.844	34

Table 3.1: Properties of the CELLO tracking chambers

At smaller angles $.91 > |cos(\Theta)| > .99$ tracking is complemented by two layers of end cap proportional chambers.

3.2.2 Calorimetry

The relatively small inner detector of CELLO allows a relatively elaborate electromagnetic calorimetry using the lead liquid argon calorimeter technique. Important design goals were a good spatial and energy resolution even for low energy ($>$ 200 MeV) photons and a good electron hadron separation over a large solid angle. This was achieved by a barrel shaped central calorimeter covering the region $|cos(\Theta)| < .86$ complemented by two end caps covering the range $.93 < |\cos\Theta| < .99$. The barrel part is made up of 2*8 lead modules in a single cryostat (see Fig. 3.4), the end cap cryostates contain two half circular modules each.

A module consists of a stack of alternating layers of continous lead plates and 2.3 cm wide strips running at 0° , 45° , and 90° with respect to the beam direction (Fig. 3.5). For readout the strips are grouped into seven independent electronic layers each containing strips at 0° , 45° , and 90° allowing an independent re-

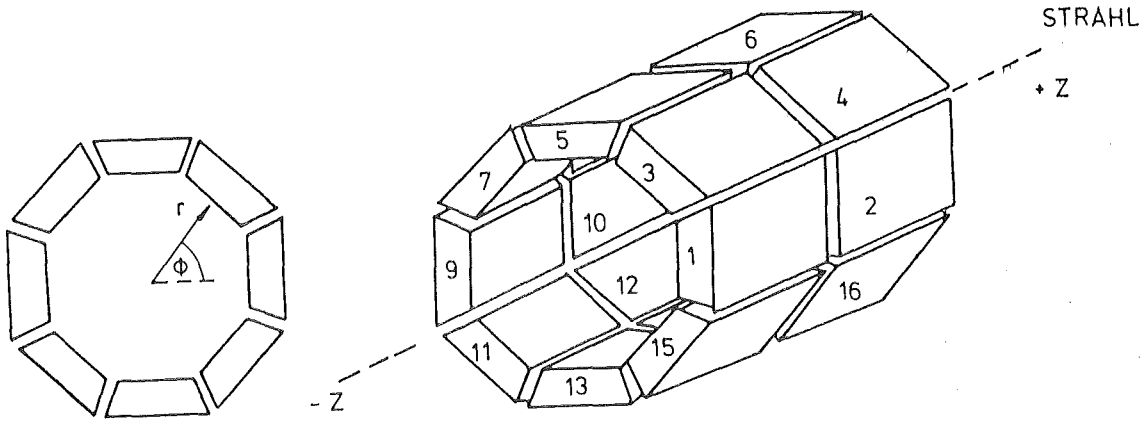

Figure 3.4: Arrangement of the barrel calorimeter modules.

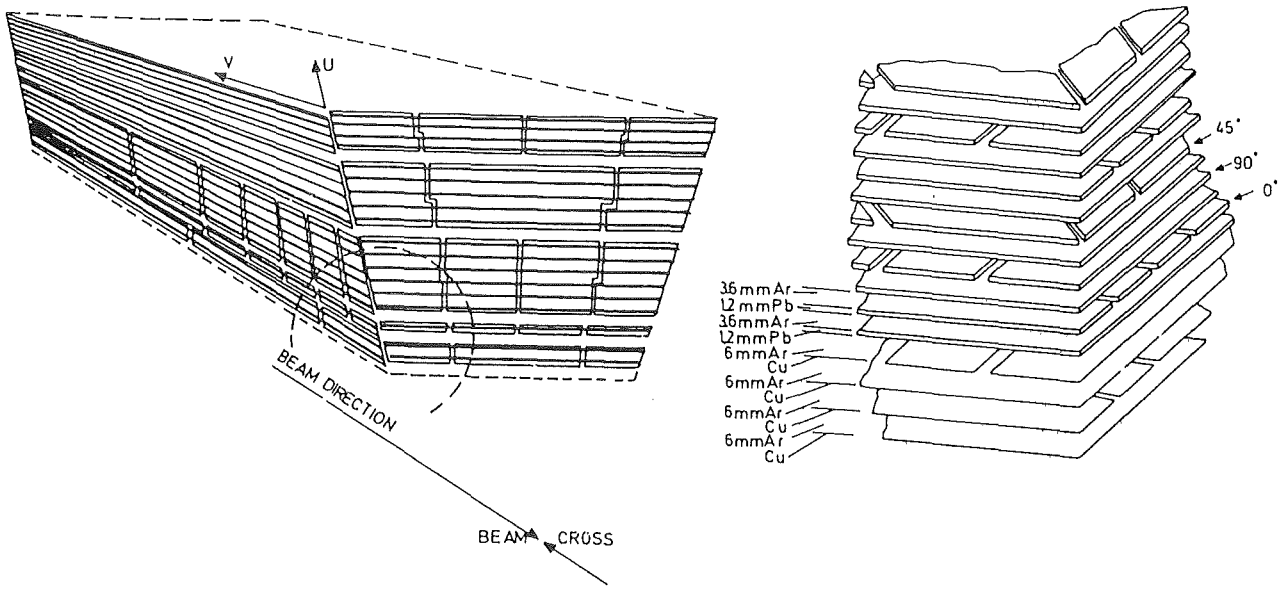

Figure 3.5: Structure of a central calorimeter module.

construction of shower clusters for each layer (Fig. 3.6). The gaps between the single lead modules are only 2 cm wide which is important for the hermeticity of the calorimetry. This was made possible by the arangement of the modules in a single cryostat. The fine lateral and longitudinal sampling provides a good spatial and energy resolution. In addition the fine sampling in depth allows to exploit the characteristic differences in the shower development for electron-hadron separation. The thin coil ($1/2\ X_0$) facilitates the detection of very low energy photons. A depth of 20 radiation lengths results in a good linearity even for highest energy electrons and photons.

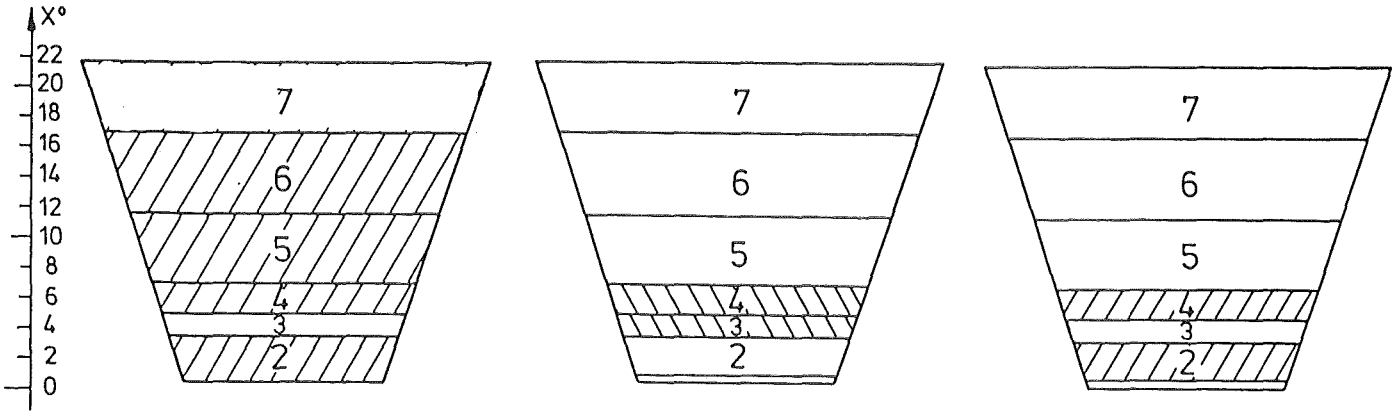

Figure 3.6: Longitudinal segmentation of the barrel calorimeter modules into seven independent electronic layers. (The first layer consists of copper plated epoxy and serves to tag showers which started in the $\sim 1X_0$ material before the calorimeter (coil, tank).) The layers used in the formation of the three trigger sums SUM A (left), SUM B (center), and SUM C (right) are indicated (see subsection 3.2.4).

The spatial resolution for electromagnetic showers is $\sim$ 5 mm corresponding to an angular resolution for photons from the interaction point of 5 mrad. The energy resolution can be described by $\Delta E/E = 5\% + 10\%/\sqrt{E}$ (E in GeV). These numbers were determined from large angle Bhabha scattering and from electrons from radiative Bhabha events averaged over all modules and over a long running period.

In spring 1984 the photon acceptance gap between the barrel and end cap calorimeters was closed by the installation of a two layer lead scintillator sandwich, the so called 'hole tagger'. It is segmented eightfold in ϕ with a sampling after 4 and 8 radiation lengths. Although its energy resolution is poor it can be efficiently used for vetoing purposes. At small angles calorimetry is complemented by lead glass arrays covering the region from 120 mrad (end of end cap acceptance) down to 50 mrad. Thus, with the installation of the hole tagger, CELLO has complete calorimetric coverage down to 50 mrad.

3.2.3 Muon Identification

Muons are detected by 32 large area proportional chambers behind the calorimeter ($\sim$ 1 absorption length λ) and 6 .. 8 absorption lengths of iron which at the same time serves as flux return yoke. They cover 92 % of the full solid angle (see Fig. 3.7). The chambers consist of anode wires spaced at 1.3 cm and cathode strips of 1.1 cm width running at $\pm 34°$ with respect to the anodes. The spatial resolution is $\sim$ 6 mm both parallel and perpendicular to the anodes. This can be compared with a track extrapolation error due to multiple scattering and the error in the track measurement of $\sim$ 5 cm for 10 GeV muons.

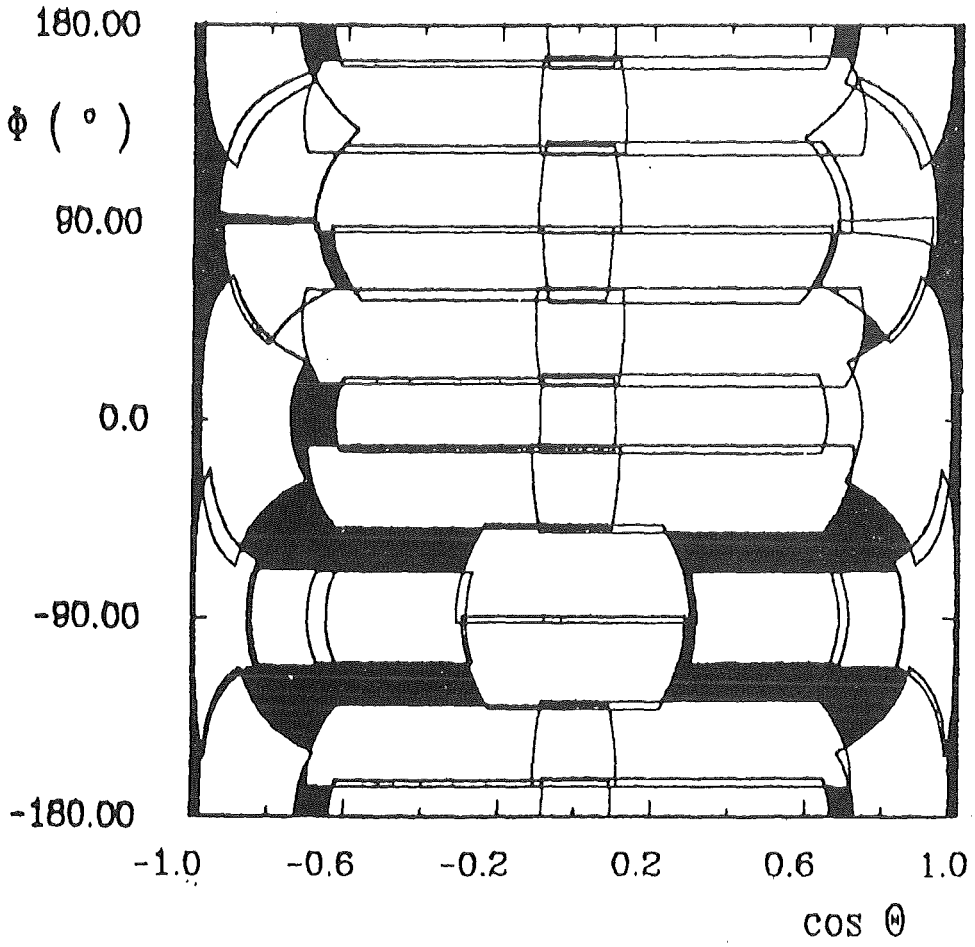

Figure 3.7: Acceptance of the 32 muon chambers of CELLO.

3.2.4 Trigger

The task of the trigger system is to reduce the bunch crossing rate of PETRA (250 kHz) to a manageable read out rate of $\sim$ 2 Hz. In CELLO this reduction factor of 10^5 is achieved by a one level trigger system. This means that the trigger decision must be available $3\mu s$ after the bunch crossing to avoid dead time. ($\sim 1\mu s$ is needed to reset the muon chamber system.) Triggers relevant for this analysis were the calorimeter trigger based on energy sums available for each calorimeter module and the charged particle trigger based on the information from the central proportional and drift chambers.

3.2.4.1 Calorimeter Trigger

For each calorimeter module 3 independent analog energy sums are formed (SUM A, B, and C, see Fig. 3.6 on page 40). They are fed into 7 bit FADC's. SUM B is sampled twice around its maximum pulse height. Critical background in particular for the low threshold purely neutral single module trigger are electronics noise and

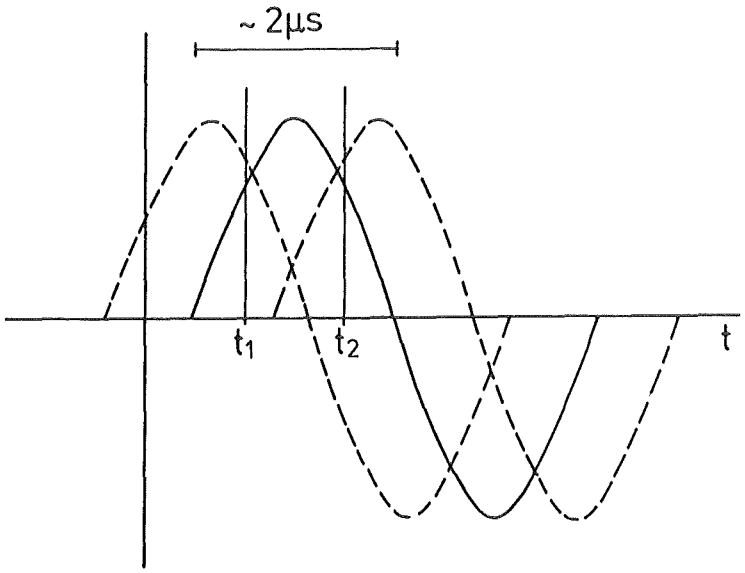

Figure 3.8: Shape of the liquid argon signal pulse. Indicated are the times t_1 and t_2 of the two samplings of SUM B. Out of time signals from cosmic showers (dashed lines) are rejected by requiring a proper correlation between SUM B_1 and SUM B_2.

cosmic showers. Electronic noise triggers are supressed by requiring a coincidence between SUM A and SUM B. A correlation condition between the two samplings of SUM B yields a timing resolution of 120 ns (see Fig. 3.8). This allows to supress cosmic showers which are not in time with the beam crossing. The correlation conditions are realized by feeding the FADC output signals into a RAM logic. In a refined analysis of the trigger sum signals in the offline filter a timing resolution of $\sim$ 25 ns is achieved. A detailed description of the CELLO calorimeter trigger can be found in Ref. [57].

The calorimeter trigger efficiency is shown in Fig. 3.9. It is determined for each running period with electrons from radiative Bhabha events triggered independently by a tag in the forward or end cap calorimeter [59].

3.2.4.2 Charged Particle Trigger

For triggering on charged tracks in the inner detector and avoiding at the same time triggers due to chamber noise or beam gas events with many low p_t tracks a hardware track finding processor is employed.

It uses the signals from the proportional chamber 90° cathodes to look for straight tracks pointing to the vertex in the rz projection (rz trigger). Signals from the proportional chamber anode wires plus two drift chamber layers serve as input for the rϕ trigger which looks for curved tracks with some minimum transverse momentum.

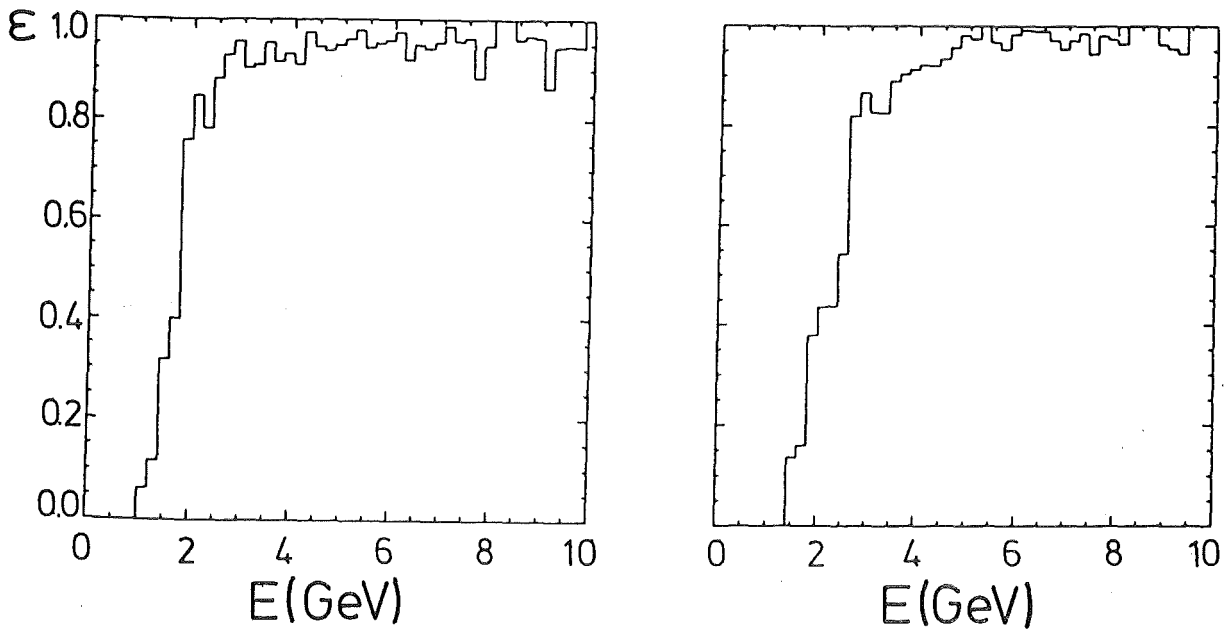

Figure 3.9: Efficiency of the calorimeter trigger as a function of the energy deposited in a module.

a.) purely neutral single module trigger.

b.) Trigger condition used in conjunction with at least one track candidate in the inner detector.

This is realized by feeding the chamber signals into the address lines of a programable random access memory. For each valid combination of input lines (mask) a logical one is stored in the RAM, indicating that a track candidate has been found. To reduce the number of masks the signal wires are grouped into into 64 sectors in rϕ and 37 in rz, covering the polar range $|\cos\Theta| < .87$. Since the RAM can be loaded from the online computer, the trigger can be adapted easily to the experimental conditions. Typical conditions in the high energy running (above 40 GeV c.m. energy) were a minimum p_t of 650 MeV and at least 6 out of 7 possible chamber hits. The trigger efficiency is determined for each running period from large angle Bhabha scattering events.

For a more detailed description of the CELLO charged particle trigger see Ref. [58].

3.2.4.3 Trigger Conditions

The trigger signals from the calorimeter trigger, the charged particle trigger, and the forward detector are used to define the actual trigger conditions. The following conditions were relevant in this analysis:

- one charged particle candidate and at least $\sim$ 1.8 GeV in a barrel calorimeter module.
- an energy deposition of at least $\sim$ 2 GeV in one of the barrel modules.
- an energy deposition of at least 1.8 GeV in each of two barrel modules separated by at least 45° in azimuth.

These partly redundant conditions give a very high combined efficiency for the reactions under study.

3.2.5 Data Aquisition

The detector is read out by a CAMAC ROMULUS system [60]. It is organized in branches, one branch for each detector component. The A2 controller in each branch master crate permits concurrent access to the branch by both the online computer and by a micro computer located in the crate. This micro computer in each detector branch is used to test, calibrate, and monitor its detector component.

The online computer, a PDP 11/44, reads out the detector branches, forms the event records, and does an event buffering. It drives the shift operator console, performs various monitoring and histogramming tasks which provide an online check of the detector components, and passes the event records via a fast data link to the online system which runs on one of the IBM mainframes of the DESY computer center. Here the events are buffered on disk for some hours and eventually dumped on tape.

The online computer also flags Bhabha and multihadron event candidates which are transferred to a separate ring buffer on the IBM mainframe. Here the events can be inspected parallel to data taking using a graphics display and the standard CELLO event display program. In regular intervals of a few hours the events are passed to the reconstruction program. They allow a fast determination of luminosity and total hadronic cross section and a calibration and efficiency determination for various detector components.

Chapter 4

Data Sample and Analysis Chain

The data used in this analysis was accumulated in the period from May 1983 until November 1985. It can be seperated into two parts:

A 11 pb^{-1} collected in an energy scan extending from 40.090 GeV to 46.780 GeV c.m. energy in 30 MeV steps in a search for narrow resonances. The average integrated luminosity per energy point was 50 nb^{-1} (experiments 26 to 30).

B 37 pb^{-1} collected at fixed energies with an average c.m. energy of $\sqrt{< s >} =$ 43 GeV (experiments 32 to 40).

Tab. 4.1 shows a summary of the various running periods. **The hole tagger veto counters were installed only after the energy scan period.** The integrated luminosity was determined from large angle Bhabha scattering.

4.1 The CELLO Analysis Chain

The bunch crossing rate of PETRA is 250 kHz. The hardware trigger logic reduces this to a readout rate of typically 2 Hz. These events are dumped on tape ('dump tapes'). The overwhelming majority of them are background and electronic noise triggers (see Tab. 4.2). The full reconstruction of an events takes several seconds of CPU time on a large IBM mainframe (such as for instance a /370 model 3084). Therefore, it is essential to reduce the number of background events before reconstruction in order to save computer time.

This task is performed by a filter program which essentially verifies the trigger conditions based on a fast track recognition and a more detailed analysis of the calorimeter trigger sums [48]. It is implemented on a /370 emulator running in parallel with data taking. It accesses the online disk in the computer center and flags the events to be kept for full reconstruction. A typical reduction factor of $\sim$ 15 is achieved in this first quasi-online filtering step.

	Exp. #	$\sqrt{< s >}$	$\sqrt{s}$	$\int L\ dt$	time period	remarks
	26	41.2	40.09 - 43.18	4.2	May 83 to Jul 83	
A	28	44.2	43.15 - 45.22	3.4	Sep 83 to Dec 83	energy scan,
	30	46.0	45.19 - 46.78	3.4	Jan 84 to Apr 84	no hole tagger
Σ(A)		43.6		11.0	May 83 to Apr 84	
	32	44.2	44.2	9.2	Jun 84 to Nov 84	
	34	46.6	46.6	1.2	"	
B	36	43.6	43.6	17.0	Mar 85 to Sep 85	hole tagger
	38	43.45	43.45	1.4	Sep 85 to Oct 85	installed
	40	38.28	38.28	8.9	Oct 85 to Nov 85	
Σ(B)		42.7		37.6	Jun 84 to Nov 85	
Σ		43.0		48.6	May 83 to Nov 85	

Table 4.1: Summary of the data sample used in this analysis. Energies are in GeV, the integrated luminosity is in pb^{-1}.

All events passing the filter are subjected to a full reconstruction of tracks, showers, and muon hits (see next section). Even after the filtering, for a running period of a few months this reconstruction takes several hundred hours of CPU time on large IBM mainframes. Moreover, it blows up the number of tapes considerably since the reconstruction increases the amount of data per event by a factor of $\sim$ 3.

In order to reduce the number of tapes to be handled in later analysis a further filtering step based on reconstructed tracks and showers (DST filter) was introduced [49]. The basic requirements are at least one track together with very little energy deposition in the calorimeter ($E_{cal} > .05E_{beam}$) or at least one shower with $E_{shower} > .10E_{beam}$. It reduces the number of tapes by a factor of $\sim$ 6. Table 4.2 show a summary of the data reduction steps in the CELLO analysis chain.

4.2 Event Reconstruction

The reconstruction of tracks in the inner detecor and showers in the calorimeter is done by three processors: CELPAT does the track finding in the inner detector, CELGEOM performs a re-fit for the tracks found by CELPAT taking into account the exact magnetic field and the position of the interaction vertex. LATRAK re-

	events	tapes	type	reduction factor
bunch crosses	$\sim 2 \cdot 10^{12}$	—	—	
triggered	$\sim 30 \cdot 10^{6}$	1330	RDT	10^5
RDT filter	$\sim 1.8 \cdot 10^{6}$	$\sim$ 150	RDT	~ 15
after reconstruction	"	274	DST	—
DST filter	$\sim 2 \cdot 10^{5}$	40	DST	~ 6
multihadrons	6000	2	DST	~ 30

Table 4.2: Number of events and number of tapes in the various analysis stages for a period typical for the high energy running of PETRA (exps. 36 to 40, 27.3 pb^{-1} at $\sqrt{s} \sim$ 42.0 GeV). RDT stands for 'Raw Data Tape', i.e. before reconstruction. DST stands for 'Data Summary Tape', i.e. after full reconstruction.

constructs showers in the calorimeter. In addition, the processor MUCH performs a muon identification. These processors are called by a general frame program for offline reconstruction ('OFFRAM') which does the management of event records, detector constants, etc.

CELPAT consists of two parts:

ANOCAT reconstructs space points in the cylindrical proportional chambers by making associations between 90° and 30° cathode strips and the anode wires.

RFIPAT looks for tracks in the $r\phi$ projection perpendicular to the beam axis using both drift and proportional chambers. To reduce the number of combinations the $r\phi$ projection is divided into overlapping sectors. The track circle is required to lie within one sector, so the sector width corresponds to an implicit momentum cut. Searching for tracks within these sectors is done by a road method. Hits which have been used in an accepted track are eliminated for further searches.

After the track finding in the $r\phi$ projection, RZPAT looks for tracks in the rz projection using only cathode hits which are associated with anode hits belonging to tracks in $r\phi$.

Great flexibility is achieved by specifying parameters such as track quality criteria, sector width, search order, etc. in a program steering matrix ('PROM'). The normal mode of operation is to run CELPAT in several subsequent passes with the cuts loosened from pass to pass. So stiff tracks from the vertex are found and eliminated first and in further passes a good efficiency is maintained even for low momentum tracks which do not point to the interaction region, as for instance K_s^0 decays.

Because of the worsened background conditions in the high energy running of PETRA it turned out to be necessary to include the interaction point into the CELPAT track search. The interaction point is determined per machine filling by subjecting both tracks of collinear large angle Bhabha scattering events to a common fit. The PETRA beam spot has a vertical width of $\sigma_y \sim 20\mu m$ and a horizontal width of $\sigma_x \sim 500\mu m$.

CELGEOM

This program refits each track using the points found by CELPAT. For this it takes into account the real (slightly inhomogeneous) magnetic field and, optionally, also the interaction point. The inclusion of the interaction point increases the lever arm of the track measurement. Since the CELLO inner detector is relatively small this improves the momentum resolution drastically.

LATRAK

This processor reconstructs showers in the calorimeter. The first step is the reconstruction of two dimensional clusters in each of the six electronic layers (each layers contains 0° , 90° , and 45 ° projections). Then the clusters are checked for a possible structure indicating a double cluster from overlapping showers. All tracks from the central detector are extrapolated into the calorimeter and it is checked whether it is possible to assign a three dimensional sequence of clusters (i.e. a shower) to the track. A line fit taking into account the center of gravity of the used 2D clusters and the extrapolated entry point of the track into the calorimeter is performed. From the remaining 2D clusters three dimensional clusters are built using the three dimensional correlation between cells. The shower axis is determined by a line fit including the interaction point. Care is taken to resolve overlapping showers and assign the proper energy to each of them.

MUCH

first reconstructs threedimensional space points from the wires hit in the muon chambers. Then all tracks are extrapolated through the iron into the muon chambers taking into account the magnetic field. To the extrapolated end point in the muon chamber an error is assigned taking into account both multiple scattering and the full track error matrix from CELGEOM. For each track with a reconstructed muon chamber hit close to its endpoint a quality factor $Q = d/\sigma_{extrap.}$ is calculated. d is the distance of the muon chamber hit from the extrapolated track endpoint.

Chapter 5

Event Selection

In this thesis searches for scalar electrons, scalar taus, zinos, winos, and charged and neutral higgsinos are described. A summary of the reactions and their respective signatures was shown in Table 2.1 on page 16. Many of these reactions have common experimental signatures and thus also common selection procedures. Table 2.2 on page 31 summarized potential signatures of supersymmetry in e^+e^- interactions together with the relevant conventional backgrounds. To avoid duplication a detailed account of the relevant selections will be summarized in this chapter. The following signatures were investigated:

- acoplanar leptons (section 5.1)
- single electrons (section 5.3)
- acoplanar jets (section 5.4)
- single jets (section 5.4)
- an excess of spherical hadronic events (section 5.5)

In searching for escaping neutral particles in e^+e^- interactions missing transverse momentum and acoplanarity are better cut quantities than just missing momentum and acollinearity.[1] This is due to 2 photon collision events and e^+e^- interactions with initial state radiation which is emitted preferentially along the beam electron direction. In these conventional processes unobserved electrons or photons emitted at small angle may carry considerable missing momentum and produce acollinear events. The transverse momentum, however, tends to be balanced in both cases. (This is in some respect similar to pp or $p\bar{p}$ collisions were the unobserved spectator jets carry away an undefined amount of longitudinal momentum.)

[1] Acoplanarity is defined here as 180° - ϕ where ϕ is the angle between two tracks (or jets) in the projection into the plane perpendicular to the beam axis. If the transverse momentum is conserved the acoplanarity is 0. Acollinearity is 180° - δ where δ is the opening angle between the two tracks.

5.1 Search for Acoplanar Leptons

Here a selection of acoplanar two track events will be described. It is sensitive to ee and $e\mu$ final states.[2] In addition, $\tau\tau$ final states are covered since the two prong topology covers $\sim$ 75 % of the tau pair decays [51]. The average momentum of the charged track however on average is only 1/3 of the original tau momentum which in turn on average carries half the momentum of the original scalar tau. This leads to a significantly weakened momentum spectrum as can be visualized by curve A in Fig. 5.3. In contrast to $\mu\mu$ final states tau pairs generally deposit sufficient energy in the calorimeter to fulfill the trigger condition. Fig. 5.1 shows the energy deposition in the barrel calorimeter for scalar tau pair production (c.f also Fig. 3.9 on page 43). Our selection is sensitive to the following supersymmetric processes:

$$\begin{aligned}
e^+e^- &\to \tilde{e}\tilde{e}, & \tilde{e} &\to e\tilde{\gamma} \\
e^+e^- &\to \tilde{\tau}\tilde{\tau}, & \tilde{\tau} &\to \tau\tilde{\gamma} \\
e^+e^- &\to \gamma\tilde{z}, & \tilde{z} &\to l\bar{l}\tilde{\gamma} \\
e^+e^- &\to \tilde{w}\tilde{w}, & \tilde{w} &\to l\nu\tilde{\gamma} \\
e^+e^- &\to \tilde{w}\tilde{w}, & \tilde{w} &\to l\tilde{\nu} \\
e^+e^- &\to \tilde{h}^+\tilde{h}^- & \tilde{h} &\to \tau\tilde{\nu}
\end{aligned} \qquad (5.1)$$

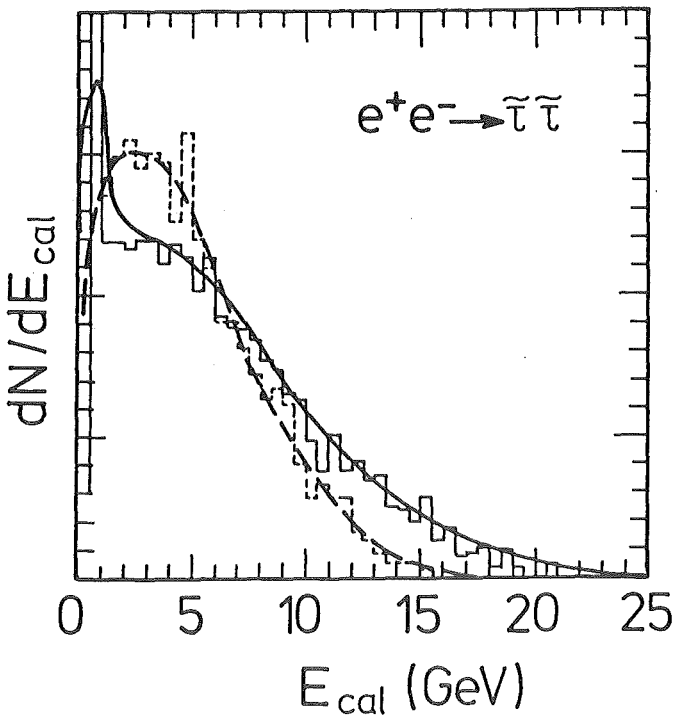

Figure 5.1: Energy deposition in the barrel calorimeter for $e^+e^- \to \tilde{\tau}\tilde{\tau}$ events fulfilling the selection cuts **C1 - C5**. The full line shows the total energy. The broken line indicates the highest energy deposited in a single calorimeter module. The latter curve can be compared with the efficiency of the calorimeter trigger depicted in Fig. 3.9 on page 43.

[2] A trigger for acoplanar μ pair final states without additional elecromagnetic energy deposition in the calorimeter was available only for a limited running period. An account of a search for this final state can be found elsewhere [15].

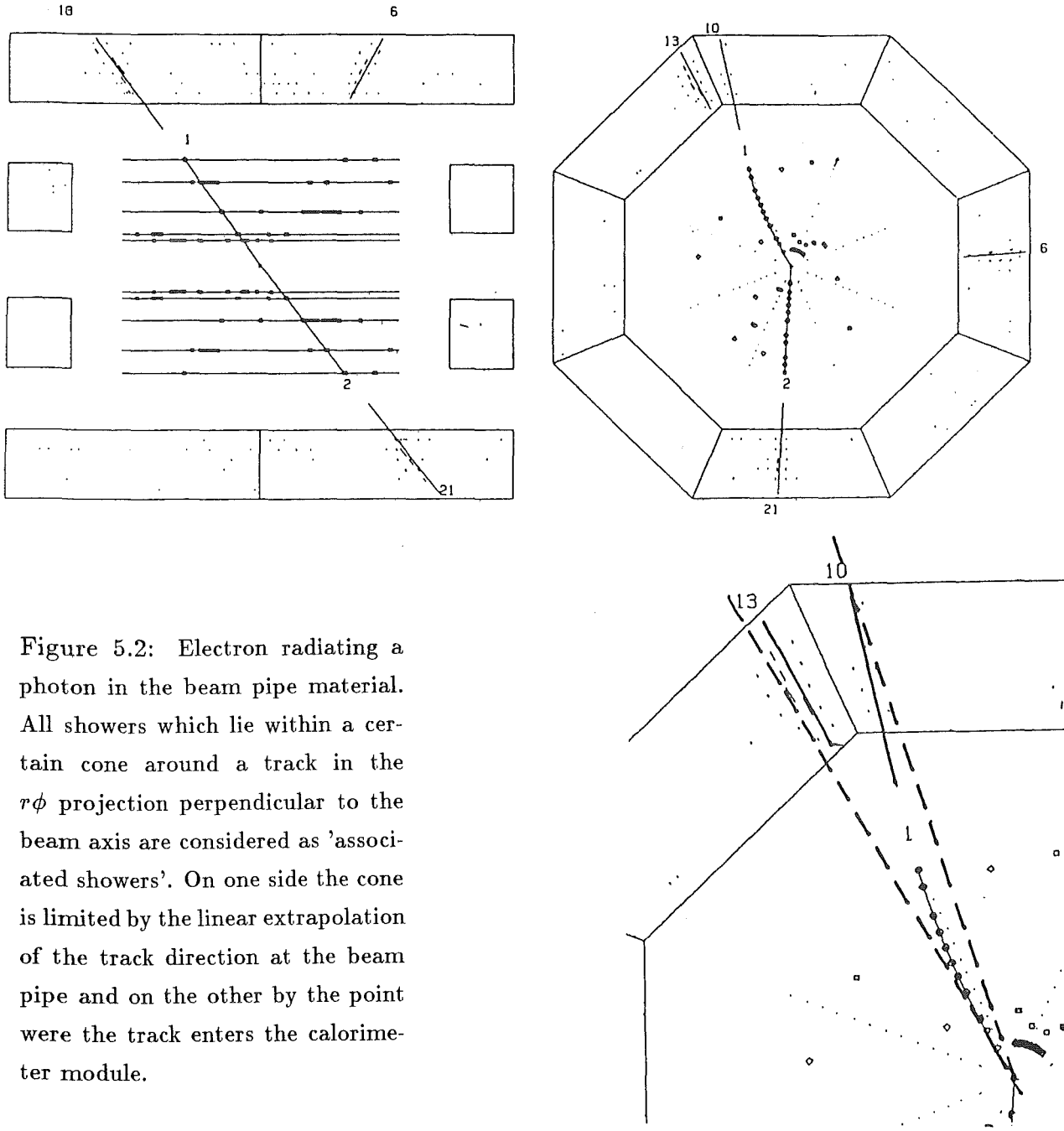

Figure 5.2: Electron radiating a photon in the beam pipe material. All showers which lie within a certain cone around a track in the $r\phi$ projection perpendicular to the beam axis are considered as 'associated showers'. On one side the cone is limited by the linear extrapolation of the track direction at the beam pipe and on the other by the point were the track enters the calorimeter module.

The philosophy applied in the automatic selection of events was to keep the cuts loose in order to be as unbiased as possible against the unexpected. Moreover, radiative lepton pair production $e^+e^- \rightarrow ll\gamma$ events were kept. They provide a useful cross check for the efficiency calculation (see next section). The following cuts were applied:

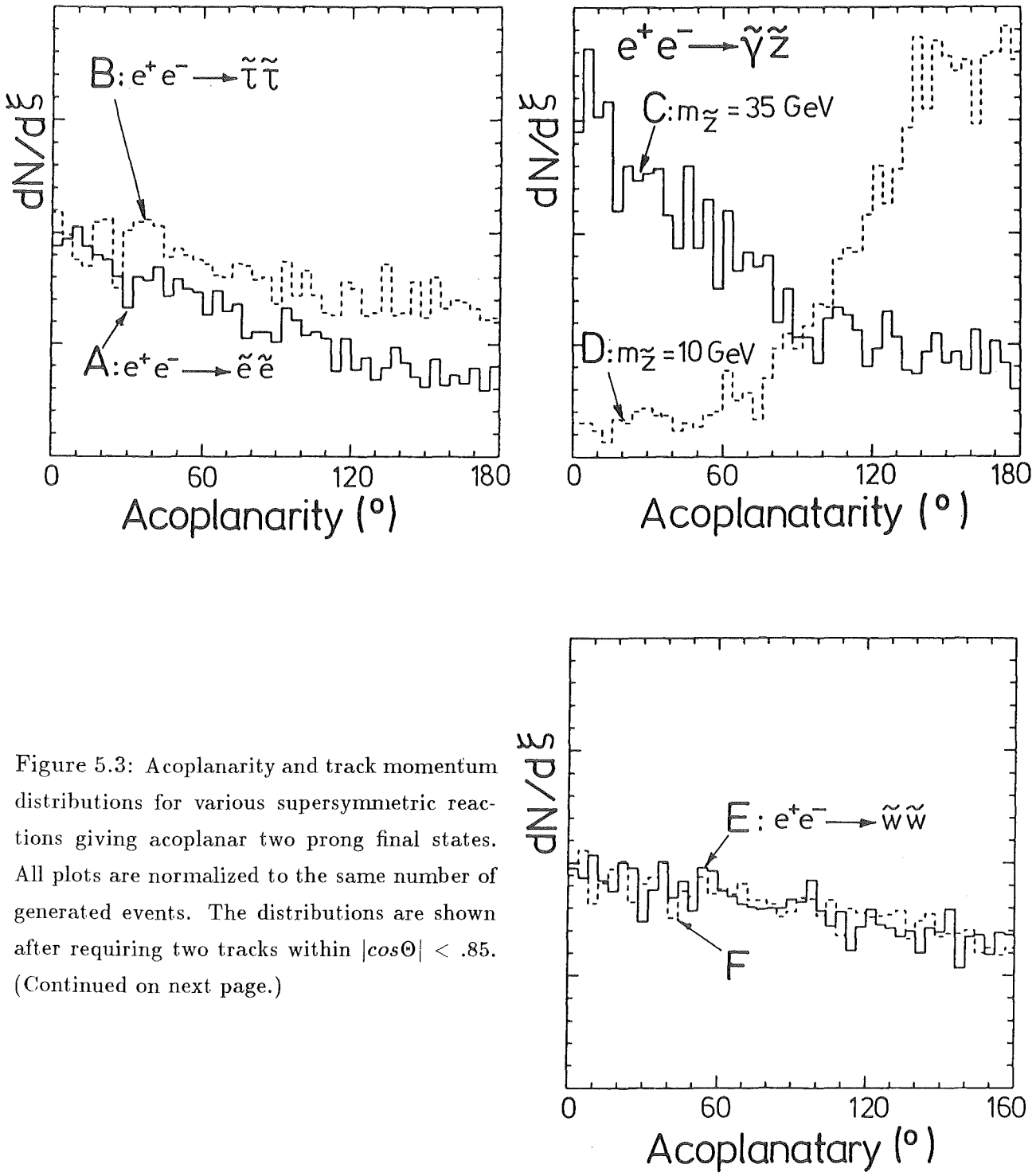

Figure 5.3: Acoplanarity and track momentum distributions for various supersymmetric reactions giving acoplanar two prong final states. All plots are normalized to the same number of generated events. The distributions are shown after requiring two tracks within $|cos\Theta| < .85$. (Continued on next page.)

C1 two tracks in the barrel region ($|cos\Theta| < .85$) originating from the vertex,

C2a track momenta $p_{1,max}$, $p_{2,max} > 2.5GeV$ [3] or

C2b $p_{1,max} > 1GeV$ and $p_{2,max} > 6GeV$,

[3] p_{max} is defined as track momentum or energy of the associated shower(s), whatever is larger (for a definition of an associated shower see Fig. 5.2). This quantity was used in order to retain events where an electron radiates a photon in the beam pipe material.

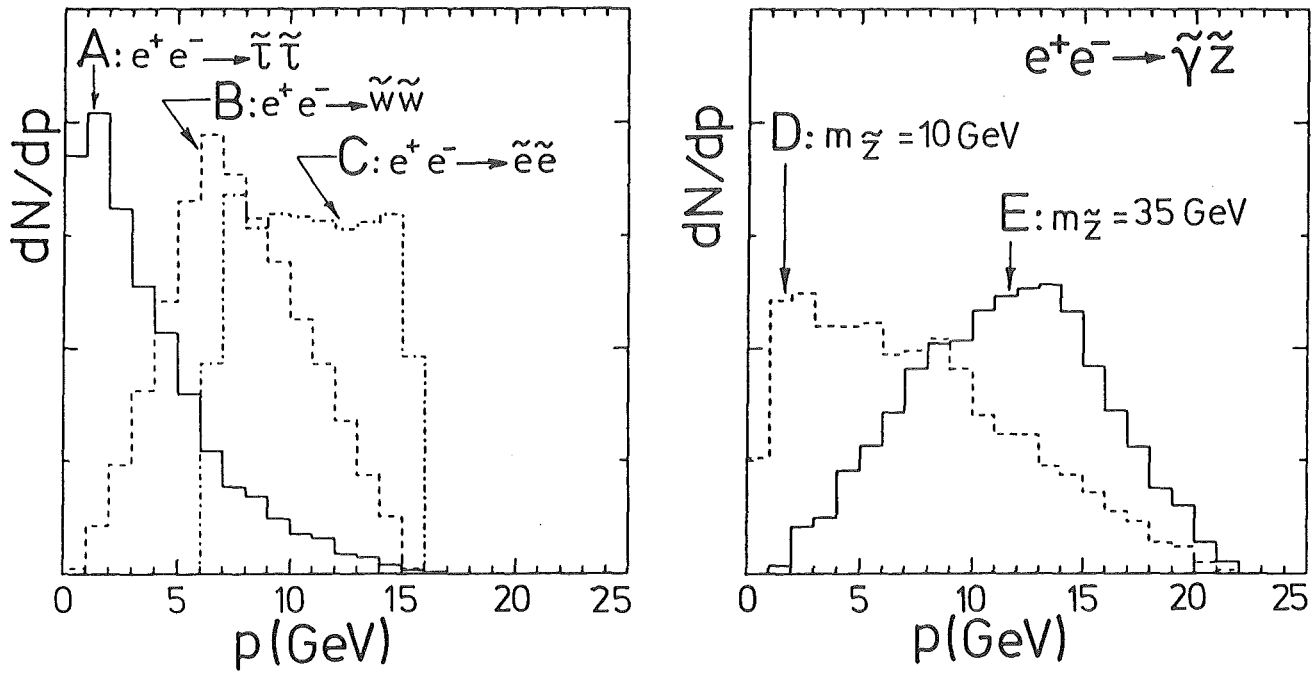

Figure 5.3 (continued)

C3 acoplanarity of the two tracks between 35° and 170° ,

C4 transverse momentum $p_t > 3GeV$.

For $\tau\tau$ final states in addition we required

C5 acoplanarity of the jet axis, as obtained by using both the tracks and the neutral particles, greater than 20° .

Cut **C3** removes collinear lepton pair production and cuts **C2, C3,** and **C4** effectively suppress lepton pairs from two photon scattering which tend to be balanced in p_t. Cut **C5** removes events from tau pair production with two very acoplanar tracks of which one has low momentum. Fig. 5.3 shows the distributions in the relevant cut quantities acoplanarity and track momentum for the SUSY reactions listed above. The 846 events remaining after the automatic selection were all visually scanned on an interactive graphics display. They can be grouped into the following categories:

50 % radiative Bhabhas ($ee\gamma$) with the photon in the barrel calorimeter (Fig. 5.5 a)

5 % $ee\gamma$ with the photon in the end cap calorimeter

2 % $ee\gamma$ with the photon in the hole tagger veto counters (4 events were recorded before the installation of the hole tagger. They were rejected because the reconstructed missing momentum pointed into the acceptance hole which was filled by the hole tagger later) (Fig. 5.5 b)

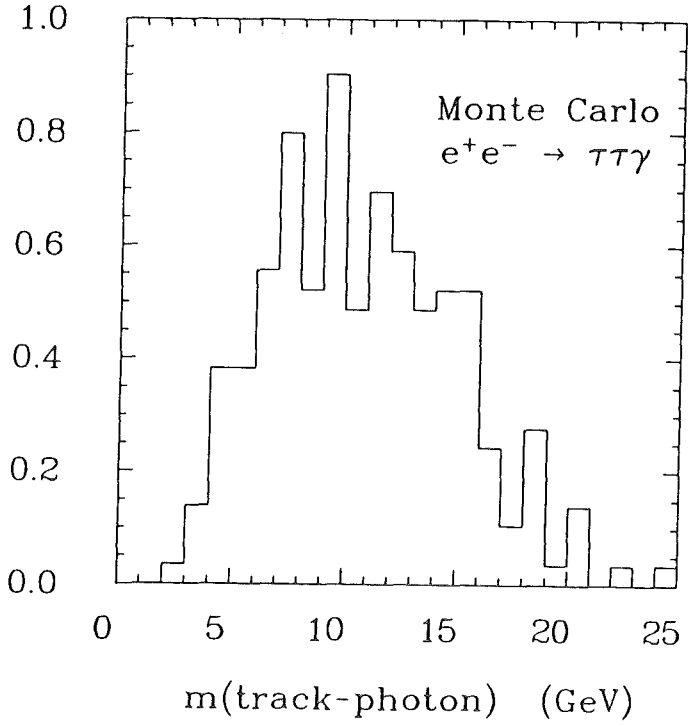

Figure 5.4: Track-photon invariant mass spectrum for $e^+e^- \rightarrow \tau\tau\gamma$ events (Monte Carlo) after cuts **C1 - C4** of the acoplanar two prong selection. Only the radiative photon is shown. Photons originating from π^0's from τ decays must have m(track-γ) $< m_\tau$. The spectrum is normalized to the number of events expected in the data sample used for the acoplanar τ search (sample B, 37 pb^{-1}).

7 % $\mu\mu\gamma$ final states (Fig. 5.5 c)

3 % $\tau\tau\gamma$ final states (Fig. 5.5 d)

10 % (e)eee final states from two photon interactions where one electron is scattered into the end cap calorimeter (Fig. 5.5 e)

6 % (e)e$\mu\mu$ final states (Fig. 5.5 f)

13 % garbage (cosmics, beam gas and beam wall interactions, electronics noise)

2 % other physics that sneaked into the event sample due to bad reconstruction, e.g. Bhabhas, τ pairs, etc.

2 events with an acoplanar e and μ of opposite charge in the barrel region and an additional muon going under small angle ($\lesssim$ 20 °) detected in the end cap proportional chambers and the end cap liquid argon calorimeter. A Monte Carlo calculation [32] shows that we expect $\sim$ 3.3 events of this type in our data sample.

$\tau\tau\gamma$ final states were rejected only if the minimum invariant mass between the photon and the tracks was larger than 2 GeV in order to avoid a bias against acoplanar τ pairs with photons originating from π^0's from τ decays. Fig. 5.5 shows the track-photon invariant mass spectrum for $\tau\tau\gamma$ final states within cuts **C1 - C4**. It is apparent that the radiative photon can be well separated from photons originating from τ decays.

reaction	decay	final states	p cut	data sample
$e^+e^- \rightarrow \tilde{e}\tilde{e}$	$\tilde{e} \rightarrow e\tilde{\gamma}$	$e-e$	2a	A and B
$e^+e^- \rightarrow \tilde{\tau}\tilde{\tau}$	$\tilde{\tau} \rightarrow \tau\tilde{\gamma}$	$\tau-\tau$	2a or 2b	B
$e^+e^- \rightarrow \tilde{h}^+\tilde{h}^-$	$\tilde{h} \rightarrow \tau\tilde{\nu}$	$\tau-\tau$	2a or 2b	B
$e^+e^- \rightarrow \tilde{w}\tilde{w}$	$\tilde{w} \rightarrow l\nu\tilde{\gamma}$	$e-e, e-\mu$	2a	A and B
$e^+e^- \rightarrow \tilde{w}\tilde{w}$	$\tilde{w} \rightarrow l\tilde{\nu}$	$e-e, e-\mu$	2a	A and B
$e^+e^- \rightarrow \tilde{\gamma}\tilde{z}$	$\tilde{z} \rightarrow ee\tilde{\gamma}$	$e-e$	2a or 2b	A and B

Table 5.1: Summary of the investigated supersymmetric reactions leading to an acoplanar lepton pair. The selection is sensitive to $e-e$, $e-\mu$, and $\tau-\tau$ final states. No candidate was observed in either final state. For $\tau-\tau$ final states and for the $\tilde{z}$ analysis a relaxed momentum cut (cut **2a** or **2b**) was used. For the acoplanar τ analysis only data sample B (37 pb^{-1} with the hole tagger) was considered.

The expected background from the processes $e^+e^- \rightarrow ee\gamma$, $\mu\mu\gamma$, and $eeee$ is negligible. They are vetoed effectively by the hermetic calorimetry of CELLO. A Monte Carlo simulation shows that also the background from $e^+e^- \rightarrow ee\tau\tau$ is negligible. It is removed effectively by cuts **C2, C3**, and **C4**.

After the scan we are left with one acoplanar τ pair events recorded before the installation of the hole tagger. Here the missing momentum direction can not be precisely reconstructed due to unobserved neutrinos from the τ decay. For this reason data sample A (11 pb^{-1} without the hole tagger) was not considered in the acoplanar τ analysis.

Tab. 5.1. shows a summary of the selection cuts and the data samples considered for the various analyses.

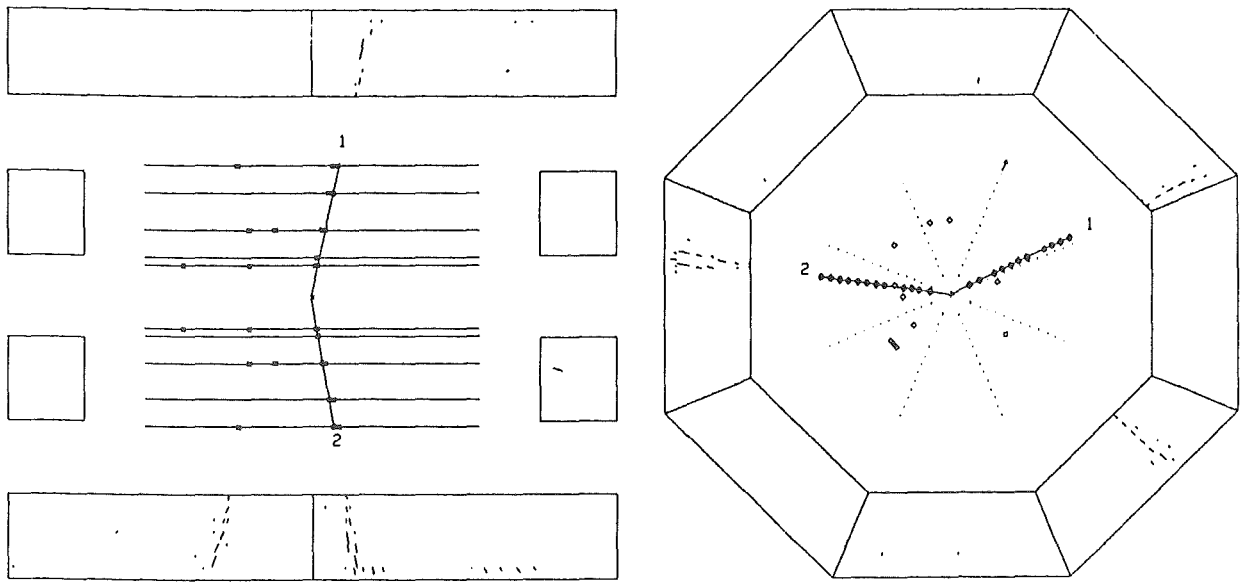

Figure 5.5: a.) $e^+e^- \rightarrow ee\gamma$ rejected due to the additional photon.

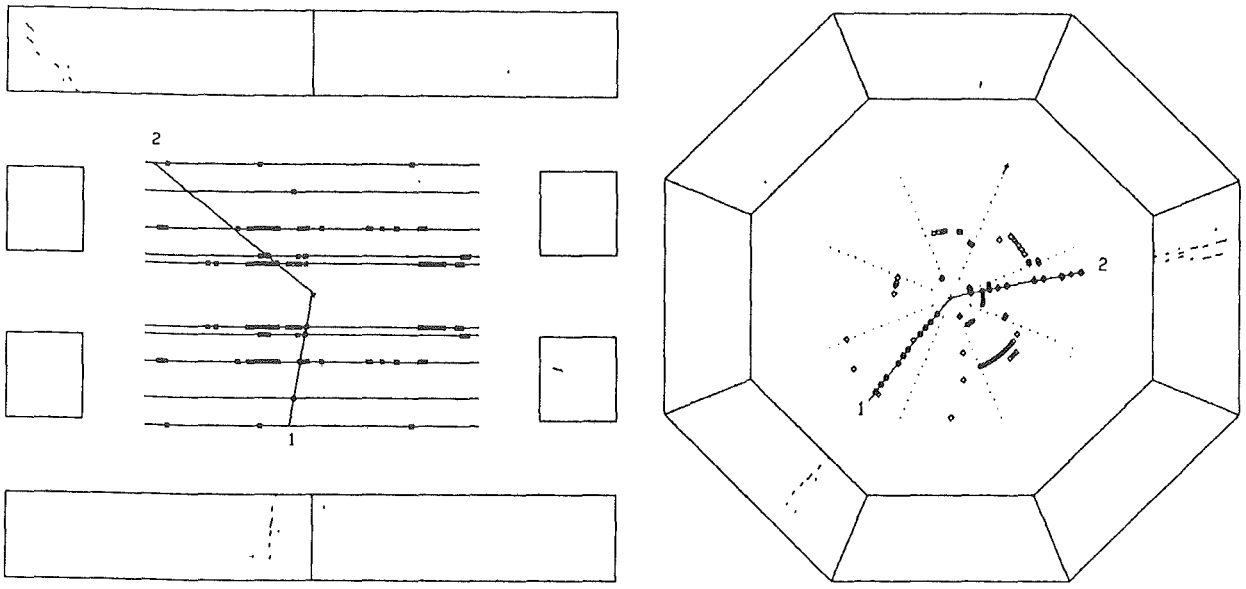

Figure 5.5: b.) $e^+e^- \rightarrow ee\gamma$ rejected due to a hit in the hole tagger veto counter. The photon polar angle as reconstructed from the observed electrons is $cos\Theta_\gamma = .89$, i.e. the missing momentum points into the hole between barrel and end cap calorimeter.

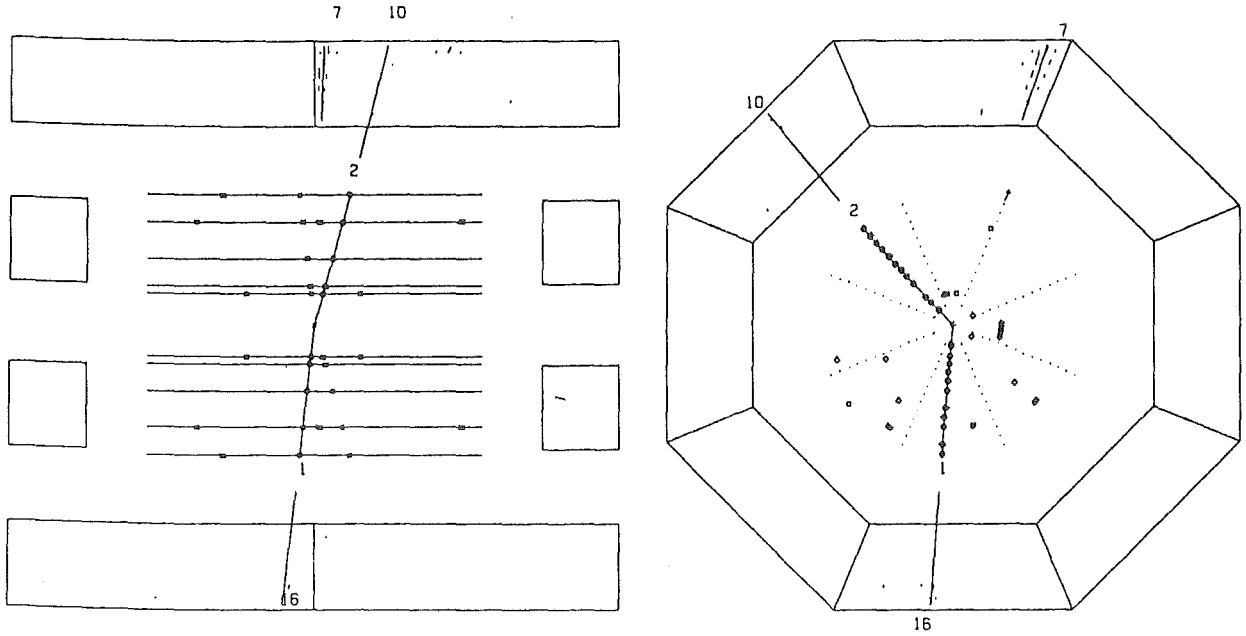

Figure 5.5: c.) $e^+e^- \rightarrow \mu\mu\gamma$ rejected due to the additional photon. Both tracks are clearly identified as muons by both their minimum ionizing behaviour in the LAr calorimeter and by an associated hit in the muon chambers.

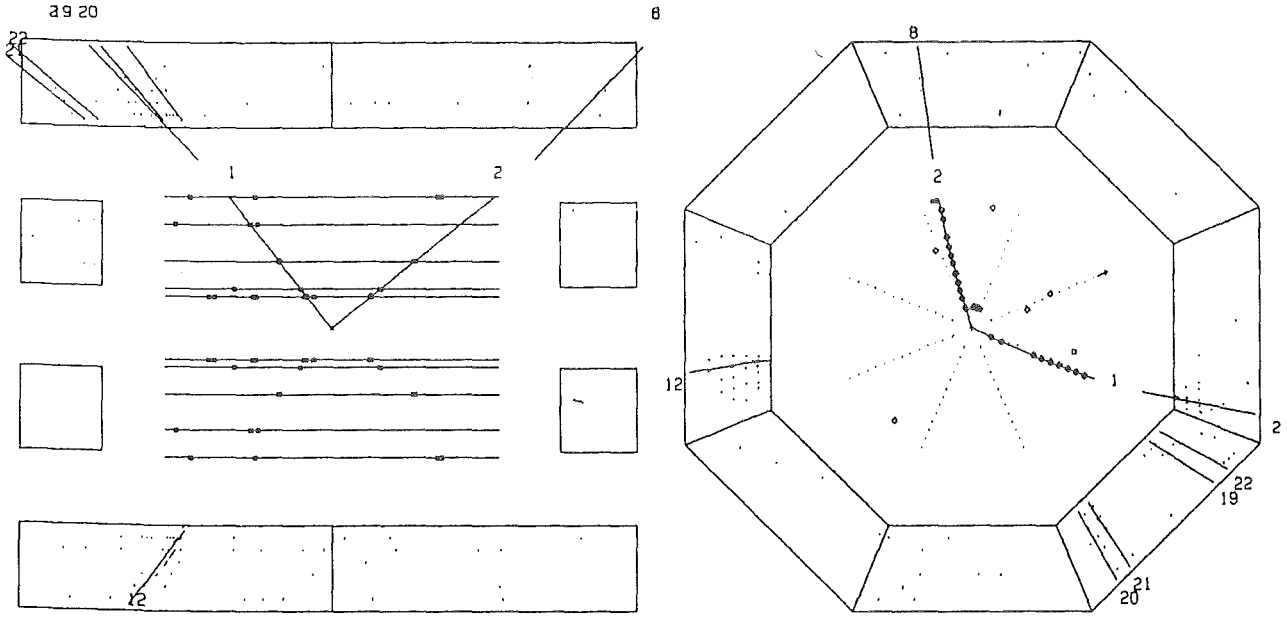

Figure 5.5: d.) $e^+e^- \rightarrow \tau\tau\gamma$ rejected due to an additional photon (shower line 12). Track 2 is identified as a muon while track 1 together with showers 2, 19, 20, 21, and 22 belongs to a multi pion decay of a tau. The invariant mass between the tracks and the isolated photon are $m(\mathrm{trk}_1, \gamma) = 7.0GeV$ and $m(\mathrm{trk}_2, \gamma) = 8.9GeV$ indicating that the photon can not be due to a π^0 from one of the tau decays.

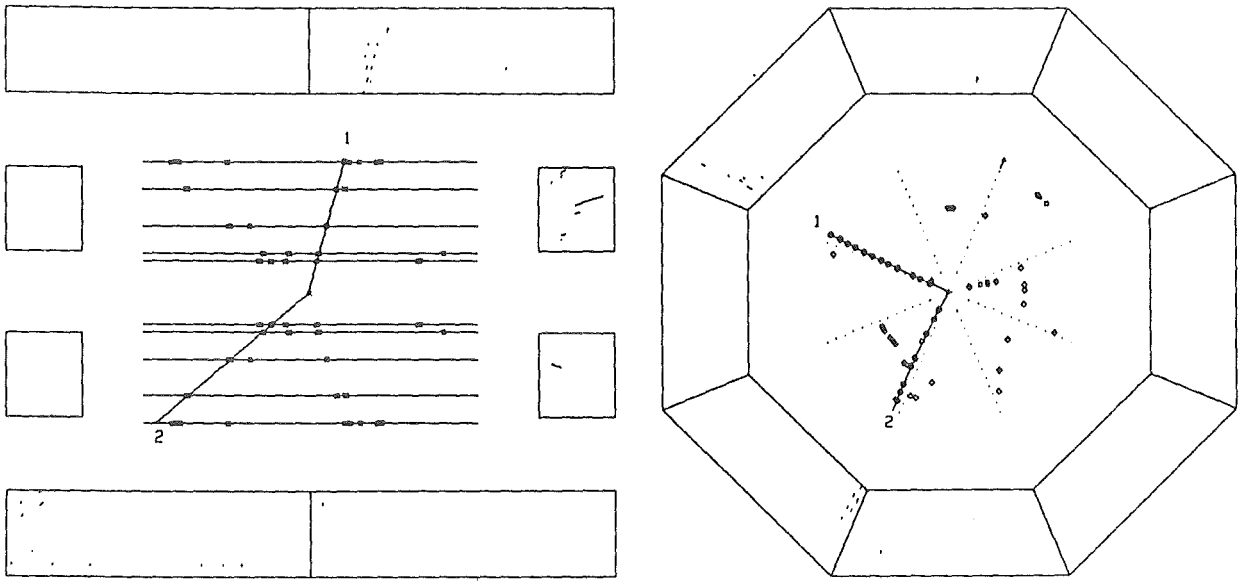

Figure 5.5: e.) $e^+e^- \rightarrow (e)eee$ with two electrons in the barrel region and one electron hitting the end cap calorimeter. A third unreconstructed track at small angle is clearly visible in the projection perpendicular to the beam.

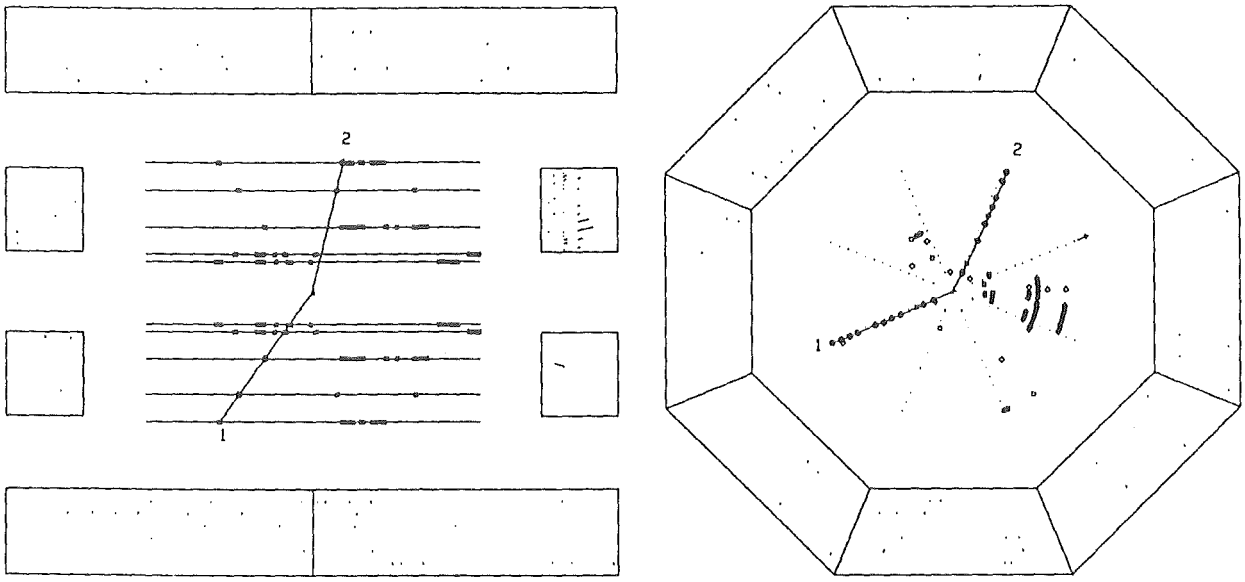

Figure 5.5: f.) $e^+e^- \rightarrow (e)e\mu\mu$. Both tracks are clearly identified muons. An additional electron with almost the full beam energy is visible in the end cap calorimeter.

5.2 Comparison of $e^+e^- \rightarrow ee\gamma$ with QED

As a cross check to monitor losses in the two prong selection a selection of $ee\gamma$ final states was made from the data sample obtained in the acoplanar lepton selection and compared with the QED prediction. The following additional cuts were applied:

- one photon with $E > .20E_{beam}$ in the barrel calorimeter ($|cos\Theta| < .85$), isolated from the tracks within 10° .
- both tracks and the photon must not point into a crack between the calorimeter modules.
- shower energy and track momentum matching ($.5 < E/p < 2$) for at least one of the two tracks.

These additional cuts yield a clean sample of 203 $ee\gamma$ events. (The residual background determined by scanning is $\sim$ 2 %.) This sample was compared to Monte Carlo events generated according to QED of order α^3 [33] with the correct weighting of the different c.m. energies. Fig. 5.6 shows the observed $e\gamma$ mass spectrum, electron acoplanarity, and the photon angular distribution. They agree well with the QED expectation. After applying corrections for tracking inefficiencies and photon conversion (for a discussion of these corrections see Chapter 6) we obtain for the total cross section

$$\frac{\sigma(e^+e^- \rightarrow ee\gamma)}{\sigma_{QED}} = .98 \pm .08 \pm .03 \qquad (5.2)$$

were the first error is statistical and the second one systematic. From this result we can conclude that we understand the efficiency of our 2 lepton selection.

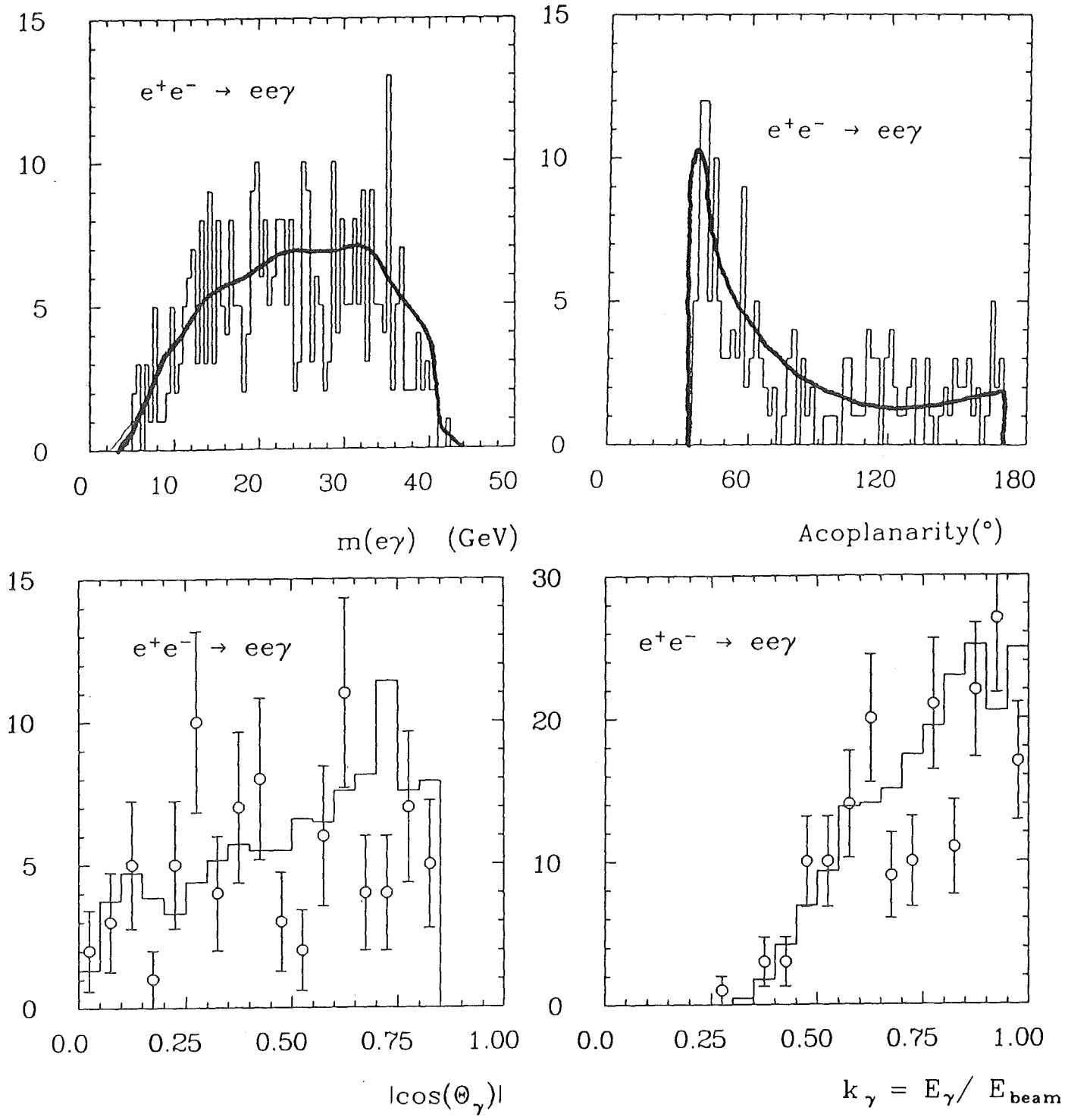

Figure 5.6: $e^+e^- \to ee\gamma$

a.) Electron-photon invariant mass spectrum. The mass resolution obtained by kinematic fitting allowing for an additional initial state radiation photon emitted under 0° (3-C fit) gives a mass resolution of $\sim$ 300 MeV. Good agreement with QED in order α^3 (full lines) is observed. In particular there is no indication of a significant peak as one would expect from the single production of an excited electron ($e^+e^- \to ee^*, e^* \to e\gamma$).

b.) Acoplanarity of the electron tracks

c.) Angular distribution of the radiated photon

5.3 Search for Single Electrons

Events with only one electron observed in the final state (together with a second electron at small angle staying in the beam pipe) are expected from single $\tilde{e}$ and single $\tilde{w}$ production in $e\gamma$ collisions:

$$\begin{aligned} e\gamma &\rightarrow \tilde{e}\tilde{\gamma} \quad \tilde{e} \rightarrow e\tilde{\gamma} \\ e\gamma &\rightarrow \tilde{w}\tilde{\nu} \quad \tilde{w} \rightarrow e\tilde{\nu} \end{aligned} \tag{5.3}$$

In the mass region of interest ($m_{\tilde{e}}$ or $m_{\tilde{w}} > E_{beam}$) the decay electron is energetic and almost isotropically distributed (see Fig 5.7).

The following cuts were applied in an automatic selection of such events:

C1 one track in the barrel region ($|cos\Theta| < .85$) originating from the vertex

C2 an associated transverse shower energy of $E_t > .3E_{beam}$ (for the definition of an associated shower see Fig. 5.2 in the previous section)

C3 no other showers in the barrel or end cap caloriometer

C4 no signal in the hole tagger veto counter

Again the veto cuts against additional showers in barrel, end cap, or hole tagger were kept loose in the automatic selection. The 266 events remaining after the selection were scanned. They can be grouped in the following categories:

31 % additional track visible

22 % additional shower in barrel or end cap calorimeter not fulfilling the loose veto cuts

20 % hole tagger hit not fulfilling the loose veto cuts

22 % instrumental difficulties (wrong beam energy in data record, hot channels in the calorimeter, hole tagger not operational (1.05 pb^{-1}))

5 % garbage (cosmics, beam gas or beam wall interactions, electronic junk)

Three events remaining after the scan verification could be removed by the following cut:

C5 the track must not point into one of the eight cracks between the calorimeter modules in the $r\phi$ projection within $\pm 15mrad$

Background from radiative Bhabha scattering with only one electron visible in the detector is removed effectively by cut **C2**, which forces either the electron or

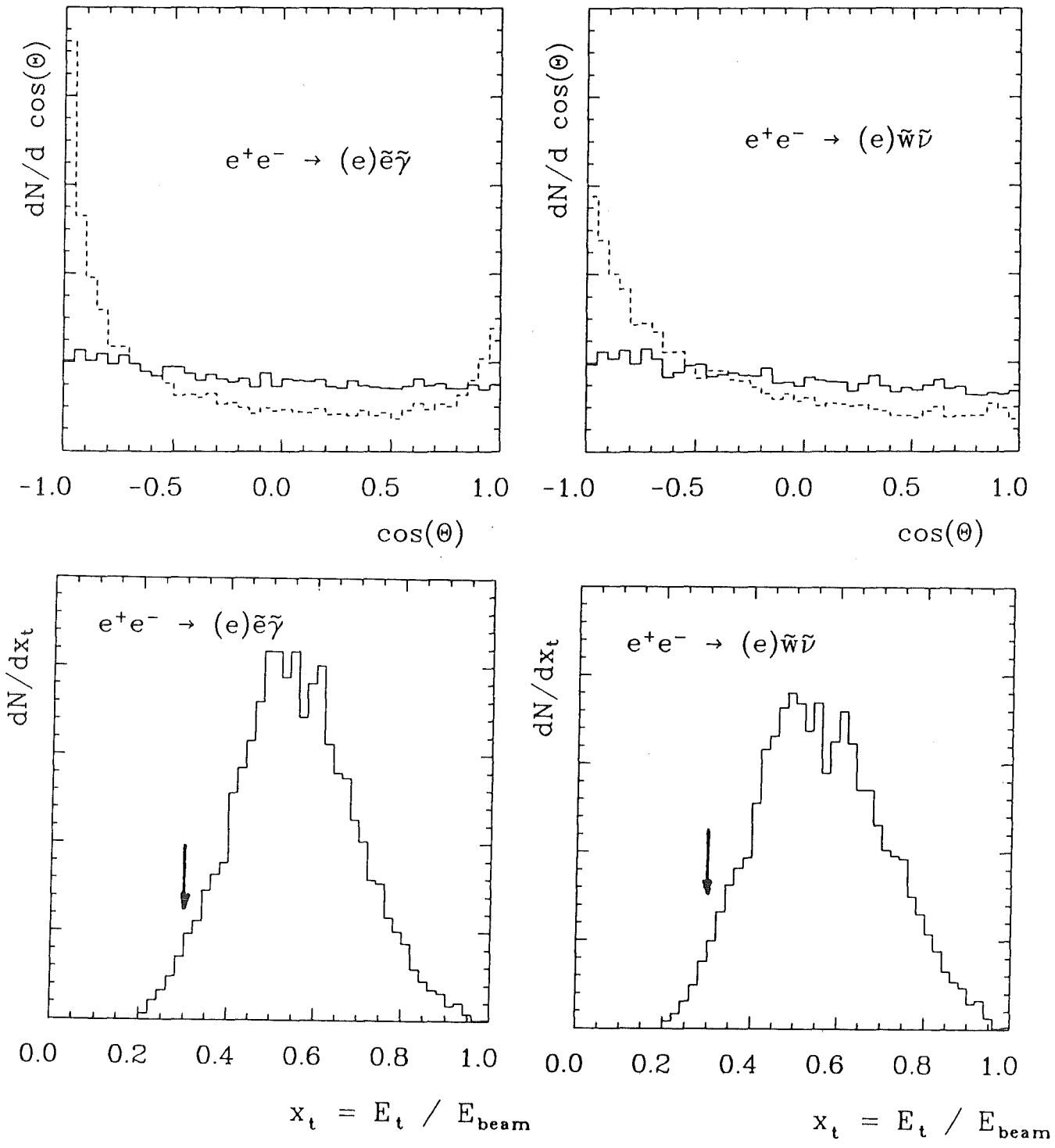

Figure 5.7: Decay electron angular and transverse energy distribution after the track acceptance cut ($|cos\Theta_e| < .85$). Also indicated is the original $\tilde{e}$ ($\tilde{w}$) angular distribution (dashed line).
$\sqrt{s} = 44\ GeV$, $m_{\tilde{e}} = m_{\tilde{w}} = 27\ GeV$, $m_{\tilde{\gamma}} = m_{\tilde{\nu}} = 0$

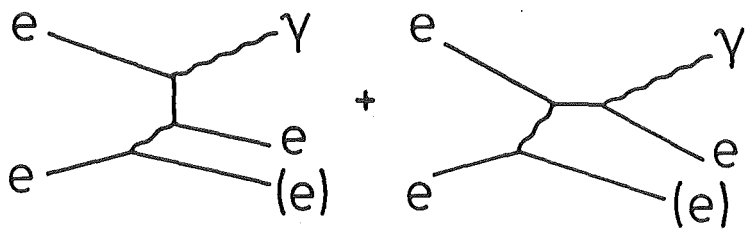

Figure 5.8: Feynman diagrams and resulting event configuration for the 'virtual Compton' process $e^+e^- \rightarrow (e)e\gamma$. If the photon is not detected this is a background in the single electron search. Note that $p_t(\gamma) = p_t(e)$. Having measured the electron it is possible to calculate the photon direction and energy assuming the other electron to be scattered at zero degree.

the photon into end cap acceptance to balance p_t. Another potentially dangerous background comes from the 'virtual compton' process $e\gamma \rightarrow e\gamma$ (the QED analogue to the process $e\gamma \rightarrow \tilde{e}\tilde{\gamma}$ shown in Fig. 2.7) where the spectator electron is scattered at small angle and the photon goes into the gap between the barrel and the end cap calorimeter (see Fig. 5.8). This QED process can be removed either by kinematic reconstruction of the photon direction from electron direction and energy and assuming the second electron to be scattered at zero degree, or by using the hole tagger as a veto against additional photons (cut **C4**). Without the hole tagger veto we expect $\sim$ 700 events with this kinematic configuration. For this reason we constrain the single electron analysis to data sample B where the hole tagger was fully installed. Cut **C5** removes 3 'virtual Compton' events where the photon escapes through one of the 2 cm wide cracks between the barrel calorimeter lead modules. After these cuts there is no candidate event left with only a single energetic electron.

5.4 Search for Hadronic Final States with Missing p_t

The following SUSY reactions give rise to hadronic final states with missing energy and momentum:

$$\begin{aligned} &(a) \quad e^+e^- \to \tilde{\gamma}\tilde{z} \ , \ \tilde{z} \to q\bar{q}\tilde{\gamma} \ , \\ &(b) \quad e^+e^- \to \tilde{\gamma}\tilde{z} \ , \ \tilde{z} \to q\bar{q}\tilde{g} \ , \ \tilde{g} \to q\bar{q}\tilde{\gamma} \\ &(c) \quad e^+e^- \to \tilde{w}\tilde{w}, \ \tilde{w} \to q\bar{q}'\tilde{\gamma}, \end{aligned} \tag{5.4}$$

The hadronic decay of a singly produced zino gives rise to a pair of acoplanar jets with missing energy and momentum carried away by photinos (Fig. 5.9a). For smaller zino masses its decay products are boosted into a single hemisphere giving rise to a monojet like event topology (Fig 5.9b). If the zino decays dominantly into $q\bar{q}\tilde{g}$ the average momentum of the decay photino is reduced but the general feature of missing energy and momentum, although less distinctive for higher zino masses, is maintained.

Wino pair production followed by the decay $\tilde{w} \to q\bar{q}'\tilde{\gamma}$ also gives hadronic final states with considerable missing energy and momentum. However, the missing p_t selections described below are not sensitive to the wino decay $\tilde{w} \to q\bar{q}'\tilde{g}$, $\tilde{g} \to q\bar{q}\tilde{\gamma}$ since here the photino is relatively soft due to the cascade decay.

The following requirements have been made in a preselection:

- a total energy of at least 2 GeV in the central liquid argon calorimeter
- at least 1 track within $|cos\Theta| < .85$ originating from the interaction point with a transverse momentum $p_t > 400MeV$, one additional track with $p_t > 120MeV$, and a total energy of the charged tracks $> .05\sqrt{s}$.

Then all particle momenta were projected onto the plane perpendicular to the beam axis ($r\phi$ projection) and the event was divided into two half planes in the

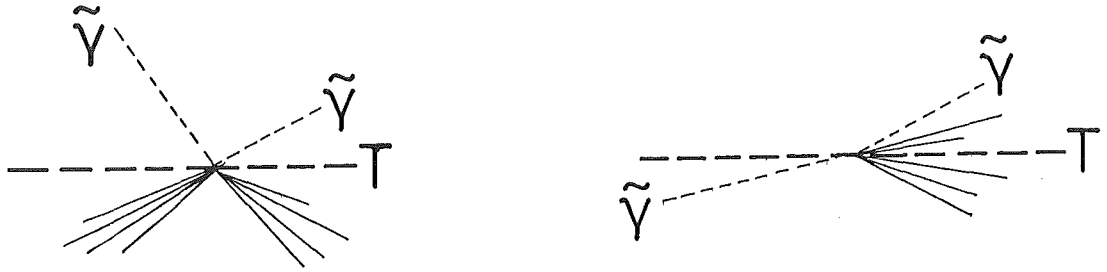

Figure 5.9: Acoplanar jet and single jet topologies expected from the single production of a heavy ($m \gtrsim E_{beam}$) or a relatively light zino. See also Fig. 5.12 for an example event of each type.

reaction	decay		$0\|X$	$X\|X$
$e^+e^- \to \tilde{\gamma}\tilde{z}$	$\tilde{z} \to q\bar{q}\tilde{\gamma}$	$m_{\tilde{z}} = 10\ GeV$	78.0(43.0) %	.3(.3) %
"	"	$m_{\tilde{z}} = 35\ GeV$	24.5(17.2) %	55.5(15.1) %
"	$\tilde{z} \to q\bar{q}\tilde{g}$	$m_{\tilde{z}} = 10\ GeV$	81.0(55.0) %	.4(1.00) %
"	"	$m_{\tilde{z}} = 35\ GeV$	3.7(1.6) %	85.4(8.8) %
$e^+e^- \to \tilde{w}\tilde{w}$	$\tilde{w} \to q\bar{q}'\tilde{\gamma}$	$m_{\tilde{w}} = 20\ GeV$	3.3(1.4) %	88.9(20.0) %

Table 5.2: Distribution of reactions (5.4) into the topological classes $0|X$ (single jet topology) and $X|X$ (two jet topology). X stands for at least two charged particle tracks in one hemisphere. The numbers in brackets are the detection efficiencies after applying the final cuts **S1**, **S2** or **A1**, **A2** respectivley (see also efficiency plots, Fig. 6.4 on page 80).

$r\phi$ projection by a plane through the interaction point and normal to the thrust axis of the projected momenta (c.f. Fig. 5.9). Then two topological classes were selected: a single jet or $0|X$ topology and a two jet or $X|X$ topology. (X stands for at least two charged particle tracks in the corresponding hemisphere.)

5.4.1 Single jet topology

Single jets have been selected by requiring

S1 one hemisphere without charged particles and at most 0.5 GeV electromagnetic energy

S2 a missing transverse momentum of all charged and neutral particles exceeding $.15\ \sqrt{s}$.

Multihadronic final states from $e^+e^- \to q\bar{q}(\gamma)$ and from 2 photon collisions tend to be balanced in p_t and are effectively removed by cut **S2**. Fig. 5.10 shows the missing p_t distribution for the reactions under study. The events remaining after this selection were scanned and residual background from beam gas interactions and due to non-reconstructed tracks or an additional photon in the hole tagger were removed. After the scan we are left with one spectacular candidate event which is shown in Fig. 5.12 a. It can be explained by quark pair production with hard initial state radiation, where the photon escapes through one of the 2 cm wide gaps between the barrel calorimeter lead modules. The probability for a photon to leave our calorimeter unseen can be estimated from data by comparing our study of the 'virtual Compton' configuration of Bhabha scattering $e^+e^- \to (e)e\gamma$ [47] with the 3 events of this type with an escaping photon observed in the single

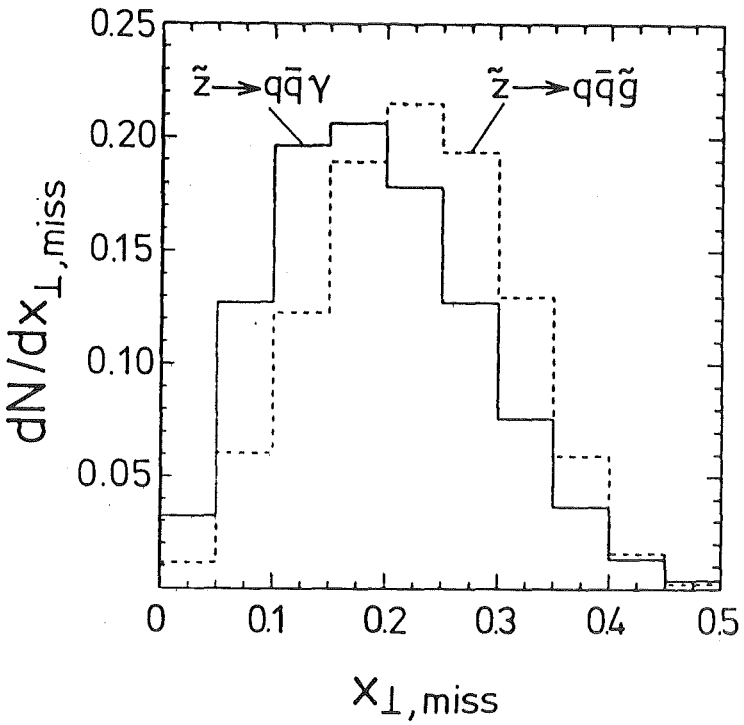

Figure 5.10: Missing transverse momentum distribution for the processes $e^+e^- \to \tilde{\gamma}\tilde{z}$, $\tilde{z} \to q\bar{q}\tilde{\gamma}$ (full line) and $\tilde{z} \to q\bar{q}\tilde{g}$ (dashed line) ($0|X$ toplogy only). Both distributions are normalized to the same number of generated events. $m_{\tilde{z}} = 10GeV, m_{\tilde{\gamma}} = 2GeV$, $m_{\tilde{g}} = 5GeV$

electron selection (c.f. previous section and Fig. 5.8). The comparison yields a probability for a photon to escape the barrel calorimeter unseen of $\sim (.28 \pm .16)\%$. Folding this with the expected number of events from $e^+e^- \to q\bar{q}\gamma$ with a hard photon in the barrel recoiling against hadrons ($k_\gamma > .95$ and $|\cos\Theta_\gamma| < .85$) tells us that we expect $\sim .5 \pm .3$ events of this type in our data sample. Taking this event as a candidate, this corresponds to a 95 % C.L. upper limit on the visible monojet cross section of .098 pb.

5.4.2 Acoplanar jet topology

To select acoplanar jets the following cuts have been made:

A1 a total visible energy from charged and neutral particles of at least $.30\sqrt{s}$

A2 an acoplanarity of the two jets (formed from all particles in the respective hemisphere) of at least 50° .

Again the few remaining events were scanned and residual background was removed. Fig. 5.11 shows the relevant distributions for the reactions under study. Fig. 5.12 b shows an acoplanar jet event which was rejected because of an additional photon hitting the hole tagger. Without this photon the event would be a typical candidate for reaction (5.4) a. After the scan we are left with one candidate event recorded before installation of the hole tagger. A Monte Carlo study shows that in our data sample we expect $\sim$ 1.2 events from multihadron pair production.

Note that the two selections for single and for acoplanar jets are completely orthogonal.

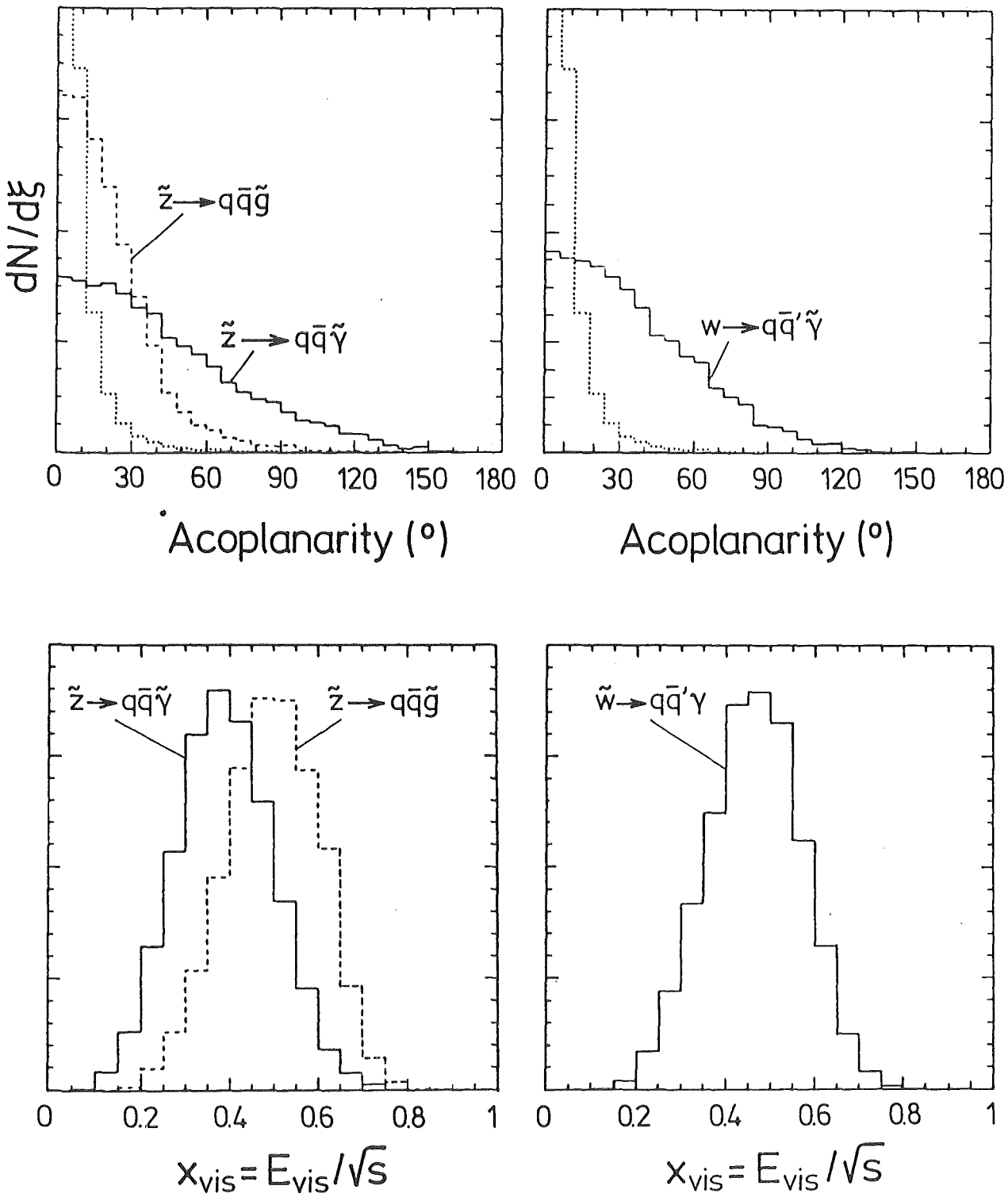

Figure 5.11: Acoplanarity and visible energy distributions for $X|X$ events. All distributions are normalized to the same number of generated events. For comparison, the acoplanarity distribution is shown also for multihadronic events from $e^+e^- \to q\bar{q}$ (dotted line).
$\sqrt{s} = 44\ GeV$, $m_{\tilde{z}} = 35\ GeV$, $m_{\tilde{w}} = 20\ GeV$, $m_{\tilde{\gamma}} = 2GeV$, $m_{\tilde{g}} = 5\ GeV$.

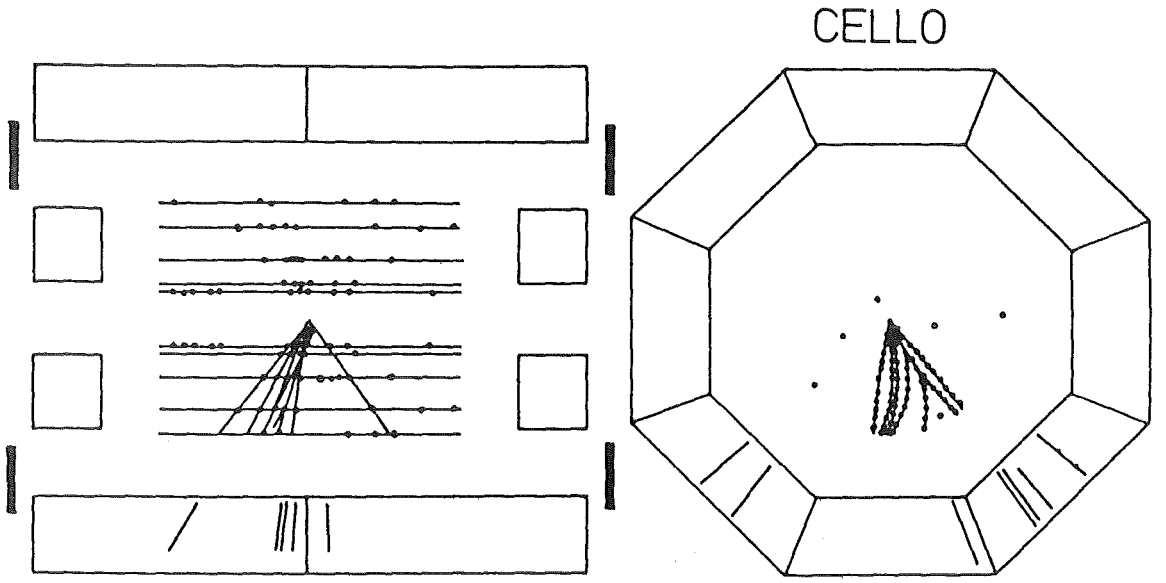

Figure 5.12:
a.) The monojet candidate event. Its most likely origin is quark pair production with hard initial state radiation with the photon escaping through a crack between the barrel calorimeter lead modules. This event topology would be expected for the decay of a relatively light (few GeV) zino.

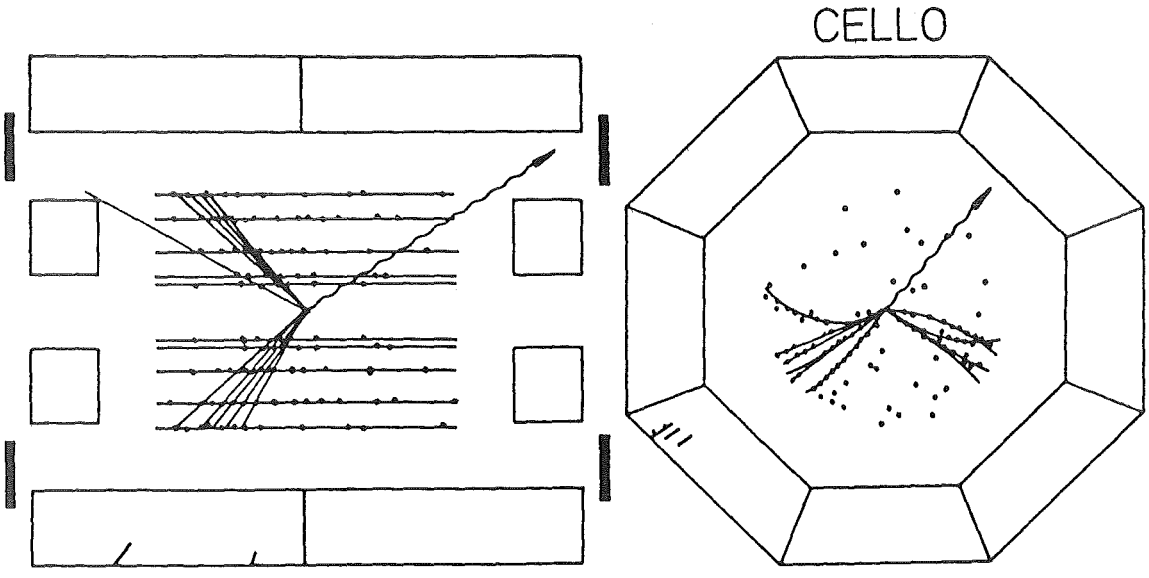

b.) An acoplanar jet candidate rejected due to a photon hitting the hole tagger counter (wiggled line) indicating radiative quark pair production $e^+e^- \rightarrow q\bar{q}(\gamma)$. This event topology is expected for the hadronic decay of a relatively massive zino ($m_{\tilde{z}} >$ beam energy).

5.5 Search for Spherical Events

An excess of spherical multihadronic events can be an indication for the production of a heavy new particle close to threshold such as for instance a new quark flavour. In the context of a search for supersymmetry, wino pair production $e^+e^- \to \tilde{w}^+\tilde{w}^-$ followed by the decay cascade $\tilde{w} \to q\bar{q}'\tilde{g}$, $\tilde{q} \to q\bar{q}\tilde{\gamma}$ would give rise to spherical events. Fig. 5.5 shows the aplanarity distribution expected for wino pair production close to threshold together with the one from normal $q\bar{q}$ production.

We made a search for such events in our multihadron data at highest PETRA c.m. energies (exp. 34, 1.1 pb^{-1} at $\sqrt{s} = 46.6$ GeV) selected by our standard cuts [40]:

- ≥ 5 charged particles within $|\cos\Theta| < .86$
- $p_{vis} > .15\sqrt{s}$
- $E_{neutral} > .08\sqrt{s}$
- $E_{vis} = p_{vis} + E_{neutral} > .40\sqrt{s}$

by requiring in addition

- Aplanarity $A > .1$ (A is defined as $3E_1/2$ where E_1 is the smalles Eigenvalue of the sphericity tensor.)

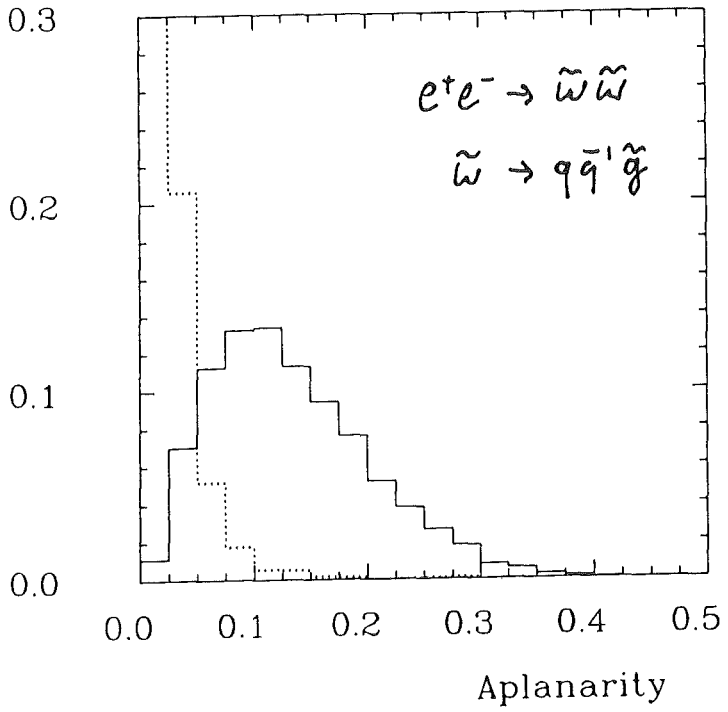

Figure 5.13: Aplanarity distribution expected from pair production of a 22 GeV wino at $\sqrt{s} = 46.6$ GeV followed by the decay $\tilde{w} \to q\bar{q}'\tilde{g}$. For comparison, the dotted curve indicates the aplanarity distribution of $e^+e^- \to q\bar{q}(g)$. Both curves are normalized to the same number of generated events.

We observe 9 events. This has to be compared with 8.3 events expected from the aplanarity distribution observed in our data at $E_{beam} = 19$ GeV. (Wino masses below 21 GeV are excluded from the total hadronic cross section.) Note that this number is determined from data and thus is independent of a Monte Carlo simulation. This is important since the correct simulation of the tail of the aplanarity distribution of multihadronic events from $e^+e^- \rightarrow q\bar{q}(g)$ is critical since it depends critically on higher order QCD contributions and also on detector effects. The aplanarity distribution for high mass wino production on the other hand is mainly determined by kinematics. Therefore, details of the Monte Carlo simulation used to determine the excess expected due to wino events play a less impotant role.

Chapter 6

Monte Carlo Methods and Efficiency Calculation

The non-observation of a signal in the signatures discussed in the previous chapter can be used to constrain the mass spectrum of supersymmetric particles. Supersymmetry unambigiously predicts the couplings of the new particles to be the same as the ones of their ordinary partners. These couplings may be modified due to mixing between the weak interaction eigenstates. If one neglects mixing, as we will do for the following discussion, supersymmetric phenomenology is only a function of the supersymmetric mass spectrum. In order to be able to exclude certain mass ranges for new particles we have to know how many events we would expect to observe in our data sample for a given process $e^+e^- \rightarrow X$ as a function of the masses of the particles involved:

$$N_{exp}(\widetilde{m}) = \epsilon(\widetilde{m})(1+\delta)\sigma(e^+e^- \rightarrow X, \widetilde{m}) \int L dt \tag{6.1}$$

ϵ is the detection efficiency in our detector and within our selection cuts. The factor δ describes radiative corrections.

The condition for a 95 % C.L. limit on a parameter f is according to Poisson statistics

$$\mathcal{P}(N_{obs}, N_{exp}(f)) = \sum_{n=0}^{N_{obs}} P_{N_{exp}}(n) \quad < \quad .05 \tag{6.2}$$

where $\mathcal{P}(N_{obs}, N_{exp})$ is the probability to observe N_{obs} events while N_{exp} where expected and $P_{\bar{n}}(n) = e^{-\bar{n}}\bar{n}^n/n!$ is the Poisson distribution. To give a specific example: If no events were observed ($N_{obs} = 0$) f is excluded at 95 % C.L. in a range where at least 3 events would have been expected (N_{exp}(f) > 3) since

$$\mathcal{P}(0,3) = \sum_{n=0}^{0} P_3(n) = e^{-3} = .050 \quad \Longrightarrow \quad N_{exp}(f) > 3$$

Or, to give another example, one event is observed and kept as a candidate. Then

$$\mathcal{P}(1,\ 4.7) = \sum_{n=0}^{1} P_{4.7}(n) = e^{-4.7} + e^{-4.7} \cdot 4.7 = .05 \quad \Longrightarrow \quad N_{exp}(f) > 4.7$$

i.e. the range in f where $N_{exp}(f) > 4.7$ is excluded. In case of a combined limit from two (or more) independent searches as for instance in the case of the zino search, where both the single jet and the acoplanar jet topology were considered, the condition

$$\prod_{i=1}^{N_{search}} \mathcal{P}(N_{obs,i}, N_{exp,i}(f)) < .05 \tag{6.3}$$

has to be fulfilled in the region where f is excluded at 95 % C.L.. N_{search} is the number of independent searches studied.

The detection efficiency ϵ as a function of the masses of the particles involved was determined by a Monte Carlo simulation of the process under study. This chapter deals with the applied Monte Carlo techniques and the correction for detector acceptance and inefficiencies.

6.1 Radiative Corrections

The lowest order cross section in e^+e^- interactions is modified by higher order QED processes. The observed cross section can be represented as the lowest order cross section σ_0 and a radiative correction δ:

$$\sigma = (1 + \delta(k_{max}))\sigma_0$$

The probability to emit a photon of energy k is proportional to $1/k$. The size of the correction δ is a function of the maximum energy k_{max} allowed for a radiated photon. Taking into account radiation only on the initial $e^{\pm}$ lines one gets [55]:

$$\delta(k_{max}) = \frac{2\alpha}{\pi}\left[(-1 + 2\ln\frac{\sqrt{s}}{m_e})(\ln k_{max} + \frac{13}{12}) - \frac{17}{36} + \frac{\pi^2}{6}\right] \quad \text{with} \quad k_\gamma = \frac{E_\gamma}{E_{beam}} \tag{6.4}$$

Note that this expression is strictly true only for one photon annihilation. Fig. 6.1 shows the radiative correction $(1 + \delta)$ to the lowest order cross section as a function of k_{max}. The radiation of an initial state photon reduces the effective center of mass energy: $\hat{s} = s(1 - k_\gamma)$. From this observation it is clear that radiative corrections are of particular importance for the production of a heavy particle close to threshold.

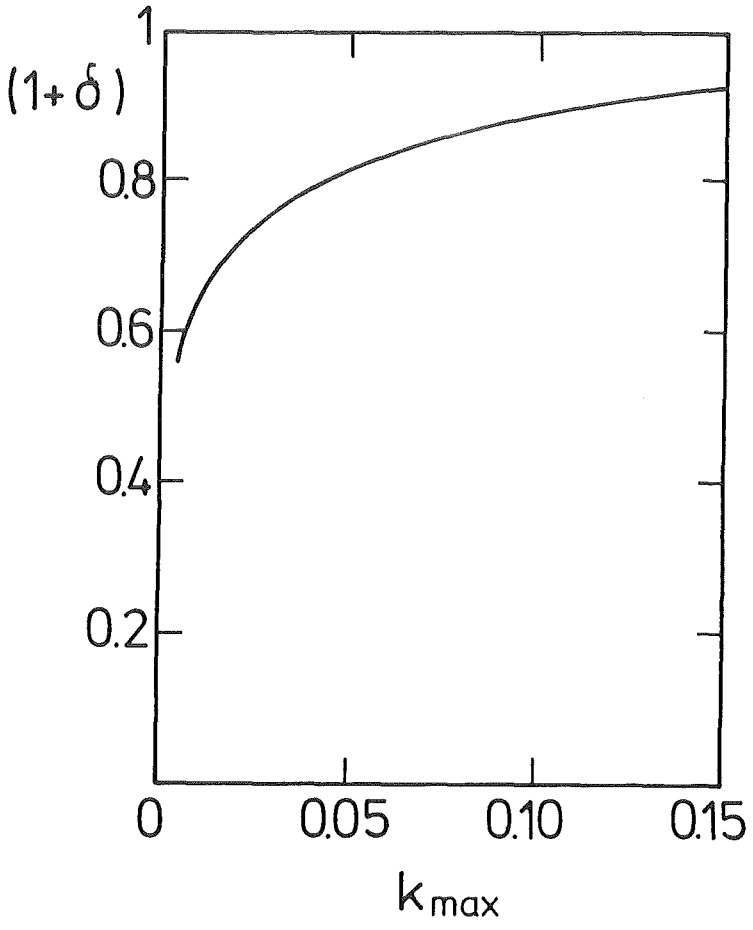

Figure 6.1: Radiative correction to the lowest order cross section as a function of the maximum energy k_{max} allowed for a radiative photon.

In calculating the expected number of events for a given process we accounted for initial state radiation as follows:

$$N_{exp} = (1 + \delta(k_{min})\epsilon(s)\sigma_0(s) + \int_{k_{min}}^{k_{max}} F(k)\epsilon(\hat{s})\sigma_0(\hat{s})\mathrm{d}k \tag{6.5}$$

where

$$\hat{s} = s(1-k) \quad \text{and} \quad F(k) = \frac{\mathrm{d}\delta(k)}{\mathrm{d}k}$$

The detection efficiency ϵ was determined as a function of the center of mass energy neglecting radiation. We used $k_{min} = .01$ and $k_{max} = .15$. This means that we conservatively neglected the contribution from events with $k_\gamma > .15$. Since initial state radiation photons are mainly emitted along the beam direction and therefore does not affect the event topology in the plane perpendicular to the beam we assumed that below $k_\gamma = .15$ the detection efficiency is essentially unaffected, except for a reduced visible energy due to a reduced effective center of mass energy which is accounted for by the c.m. energy depence of $\epsilon(s)$. This is a very conservative approach not only because the contribution from events with $k_\gamma > .15$ is neglected but also because hadronic and leptonic vacuum polarization, which increase the cross section, were not taken into account.

6.2 Event Generation

6.2.1 Production

For the processes

$$\begin{aligned} e^+e^- &\to \tilde{e}\tilde{e} \\ e^+e^- &\to \tilde{\tau}\tilde{\tau} \\ e^+e^- &\to \tilde{w}\tilde{w} \\ e^+e^- &\to \tilde{h}^+\tilde{h}^- \\ e^+e^- &\to \tilde{\gamma}\tilde{z} \\ e^+e^- &\to \tilde{h}_1^0\tilde{h}_2^0 \end{aligned} \tag{6.6}$$

events were generated according to the differential cross sections compiled in Appendix A. To avoid a sensitivity of the results to the scalar neutrino mass and to a possible higgsino admixture to the wino the $\tilde{\nu}$ exchange amplitude was neglected for $e^+e^- \to \tilde{w}^+\tilde{w}^-$.

Things are a bit more involved in single $\tilde{e}$ and single $\tilde{w}$ production in $e\gamma$ collisions. Here events were generated according to the double differential cross section (see also Equ. (2.5) on page 21)

$$\frac{\mathrm{d}^2\sigma(e^+e^- \to (e)X)}{\mathrm{d}\cos\hat{\Theta}\mathrm{d}y} = F(y)\frac{\mathrm{d}(\sigma(e\gamma \to X, \hat{s})}{\mathrm{d}\cos\hat{\Theta}} \tag{6.7}$$

Table 6.1: Branching ratios used in the simulation of τ decays. Cabbibo suppressed channels (e.g. $\tau \rightarrow K\nu_\tau$, $\tau \rightarrow K^*\nu_\tau$) were neglected.

τ decay channel	branching ratio
$e\nu_e\nu_\tau$	.175
$\mu\nu_\mu\nu_\tau$	.175
$\pi\nu_\tau$	.120
$\rho\nu_\tau$	.240
$A_1\nu_\tau,\ A_1 \rightarrow \pi\pi^0\pi^0$	.045
$A_1\nu_\tau,\ A_1 \rightarrow \pi\pi\pi$	.045
$\nu_\tau\pi + n\pi^0$	.100
$\nu_\tau\pi\pi\pi + n\pi^0$	.100

where $\hat{s} = y \cdot s$ and $\hat{\Theta}$ are c.m. energy and scattering angle in the $e\gamma$ rest frame. The energy of the radiated photon $y = E_\gamma/E_{beam}$ is kinematically limited to the interval $[y_{min}, 1]$ with $y_{min} = (m_{\tilde{e}} + m_{\tilde{\gamma}})^2/s$. Then the produced $\tilde{e}$ (or $\tilde{w}$) was boosted back into the laboratory frame and decayed.

6.2.2 Decay

For $\tilde{l} \rightarrow l\tilde{\gamma}$ and $\tilde{w} \rightarrow l\tilde{\nu}$ isotropic two body decays were performed. τ decays were generated according to the branching ratios summarized in Tab. 6.1. Cabbibo suppressed channels were neglected.

For the decays $\tilde{z} \rightarrow f\bar{f}\tilde{\gamma}$, $\tilde{z} \rightarrow f\bar{f}\tilde{g}$, $\tilde{w} \rightarrow f\bar{f}'\tilde{\gamma}$, $\tilde{w} \rightarrow f\bar{f}'\tilde{g}$, and $\tilde{g} \rightarrow f\bar{f}\tilde{\gamma}$, (see diagrams a, b, c, e, g, i, and j in Fig. 2.12 on page 25) the matrix element given in Ref. [52] was used. For wino decay via W exchange (diagrams f and h) we used the standard weak decay matrix element.

The relative amount of the kinematically possible quark flavours in hadronic zino, wino, and gluino decays was choosen according to the known couplings and the available phase space. The Lund fragmentation scheme [53] was used to model the hadronization of the emerging quark - antiquark pairs.

6.3 Simulation of Detector Effects

The determination of the efficiency function $\epsilon(\widetilde{m}_i)$ which in most cases depends on more than just one mass requires a lot of Monte Carlo runs for different mass values $\widetilde{m}_i$. Therefore, a full simulation of the detector response including the simulation of electromagnetic and hadronic showers in the detector material with subsequent event reconstruction by the standard programs (in the following referred to as 'full Monte Carlo' a brief description of which can be found for instance in Ref. [54]) is not feasible.

	single e	$e-e$	$e-\mu$
trigger	.95	1	.99
cal. gaps	.95	1	.95
tracking	.95	.90	.90
total	.86	.90	.85

Table 6.2: Global corrections applied to the selection efficiencies for $e-e$, $e-\mu$, and single electron final states. The calorimeter gap factor is a conservative estimate. It stems from requiring at least one of the electrons to be 2 cm away from a calorimeter module edge.

For the simple topologies $e-e$, $e-\mu$, and single electrons track momenta and shower energies were smeared according to measured resolutions. Then the selection cuts discussed in the previous chapter were applied. Global corrections were made for track and calorimeter trigger inefficiencies, the small gaps between the calorimeter modules, and for tracking losses (see Tab. 6.2). The quoted trigger efficiency is a combined value calculated from the single efficiencies of the relevant triggers which were determined experimentally (see Chapter 3). The tracking efficiency was measured using large angle Bhabha scattering events. Of course, this figure is valid only for low multiplicity events. No correction was applied for photons radiated from electrons in the beam pipe material since special care was taken in the selection to keep these events (see previous chapter).

The strategy to keep a simulation of detector effects as simple as possible and to apply corrections using measured efficiencies later was adopted also for $\tau-\tau$ final states with the only exception that a detailed simulation of the calorimeter trigger was performed. For this purpose the energy deposition of electrons, photons, muons, and pions was summed separately for each calorimeter module. Muons and pions were treated as minimum ionizing particles which deposit typically 300 MeV/sinΘ in our calorimeter. The energy deposition of $\tilde{\tau}\ \tilde{\tau}$ events was shown in Fig. 5.1 on page 50. Then the calorimeter trigger conditions were simulated taking into account the measured energy dependence of the trigger efficiencies (see Fig. 3.9 on page 43) which varied somewhat from one experimental period to the other. Since $\tau\tau$ final states may contain many photons from π^0 decays an additional correction had to be applied for photon conversion in the beam pipe material which leads to additional tracks distorting the two track topology. The photon conversion probability is $\sim$ 3.2 %/sinΘ. A comparison of the MC method described above with the full Monte Carlo where photon conversion in the detector material is accounted for and tracking is done with the same programs as for data

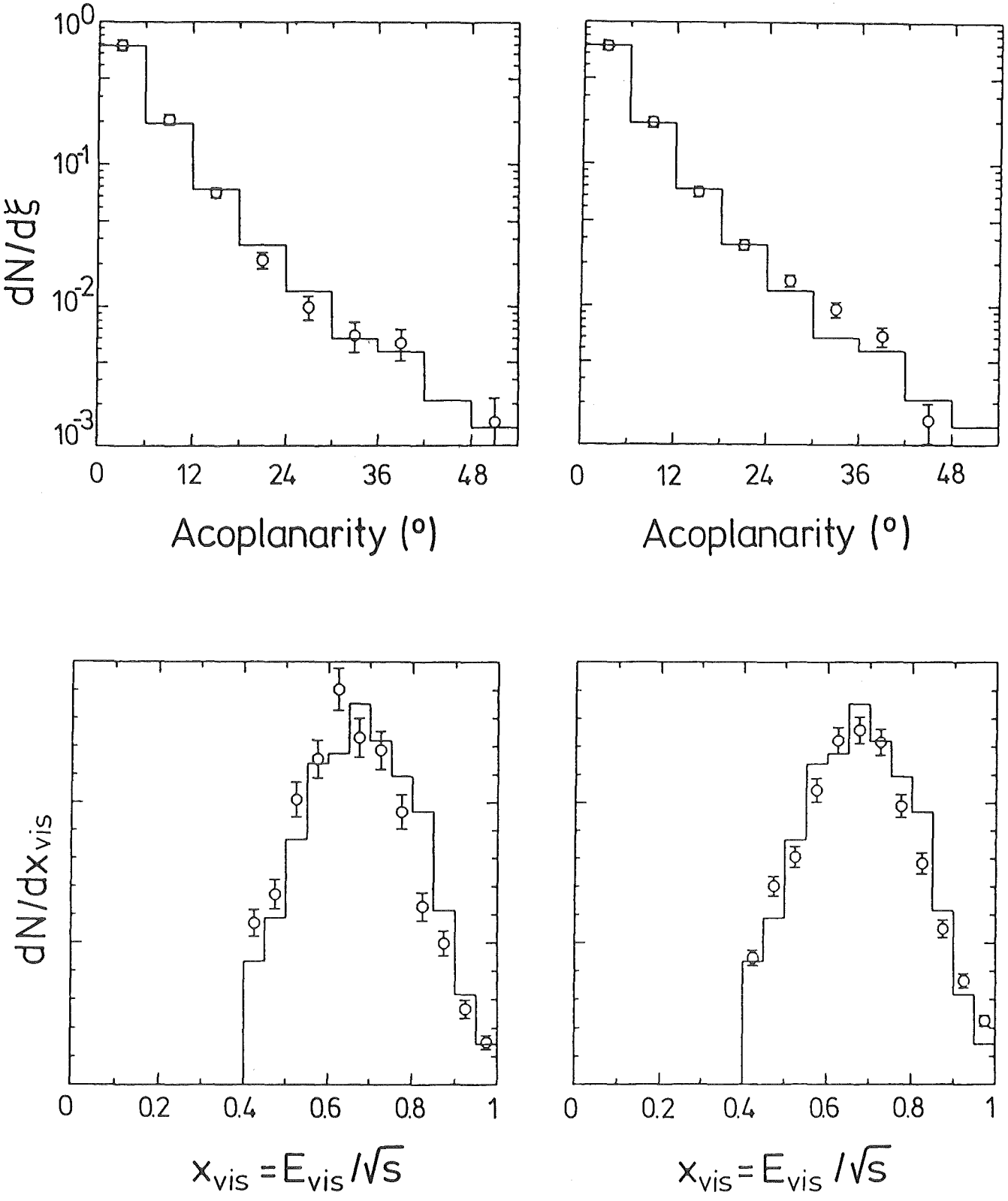

Figure 6.2: Comparison of the fast detector simulation (full line) with data (left) and with the full detector simulaltion (right) for $e^+e^- \to q\bar{q}(g)$ within the standard multi-hadron selection cuts (see page 69). Shown are visible energy, jet acoplanarity, and event aplanarity. (continued on next page.)

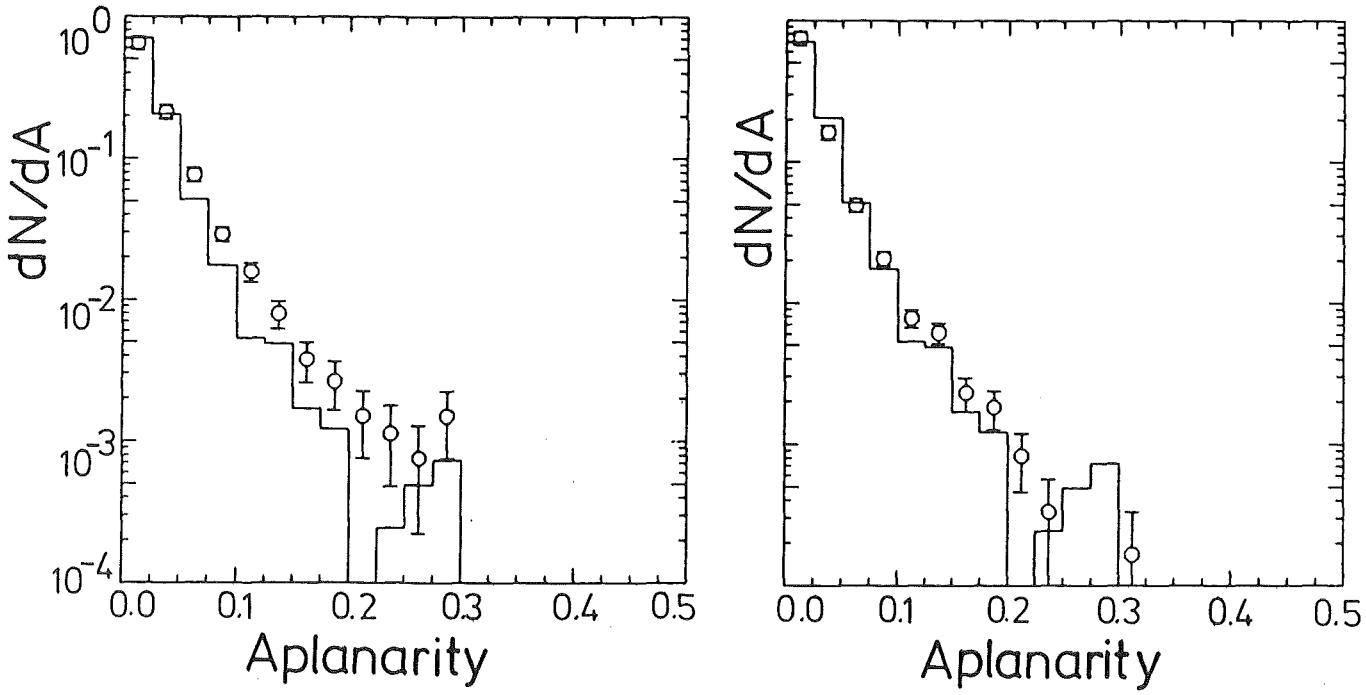

Figure 6.2 (continued)

shows a very good agreement.

A simplified modelling of detector effects was used in the simulation of hadronic final states. It takes into account detector acceptance, tracking losses, track - photon overlap, shower finding efficiencies, and hadron absorption and photon conversion in the beam pipe. It was tuned to reproduce distributions observed both in multihadron data and in the full detector simulation. Fig. 6.2 shows a comparison with both multihadron data and the full detector Monte Carlo for total visible energy, jet acoplanarity, and event aplanarity.

6.4 Discussion

Figs. 6.3 and 6.4 summarize the detection efficiencies obtained for the various processes under discussion. In the case of pair production followed by the decay into lepton or jet(s) plus unobserved neutral(s) (Figs. 6.3 a and b, 6.4 a and b) with rising masses the efficiency rises because the events become more and more acoplanar. (For small masses all decay products are boosted into the original direction of the parent particle.) What can not be observed from the figures is that the efficiency drops as the mass of the neutral particle comes close to the mass of the parent particle. This is because then the energy of the visible decay product(s) drops below the selection requirements. Note that the detection efficiency for acoplanar $\tau\tau$ final states (Fig. 6.3b) is significantly lower than for ee

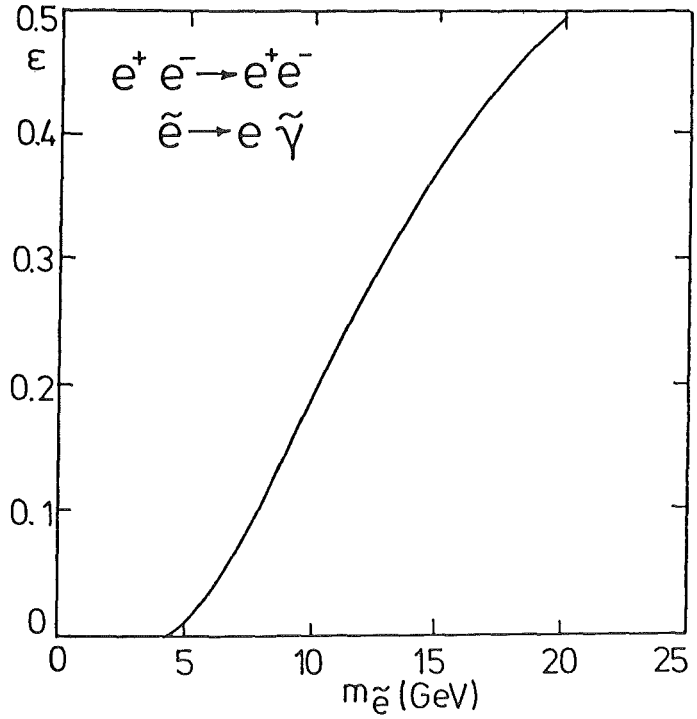

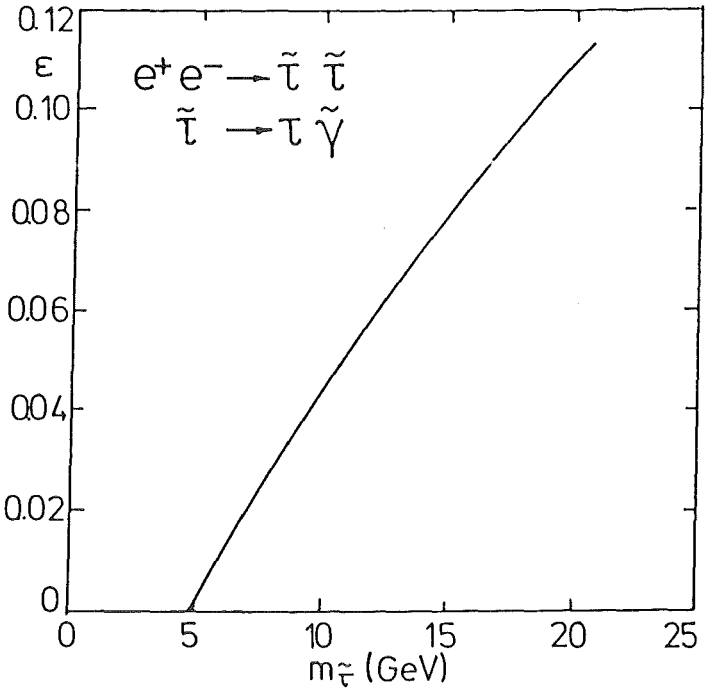

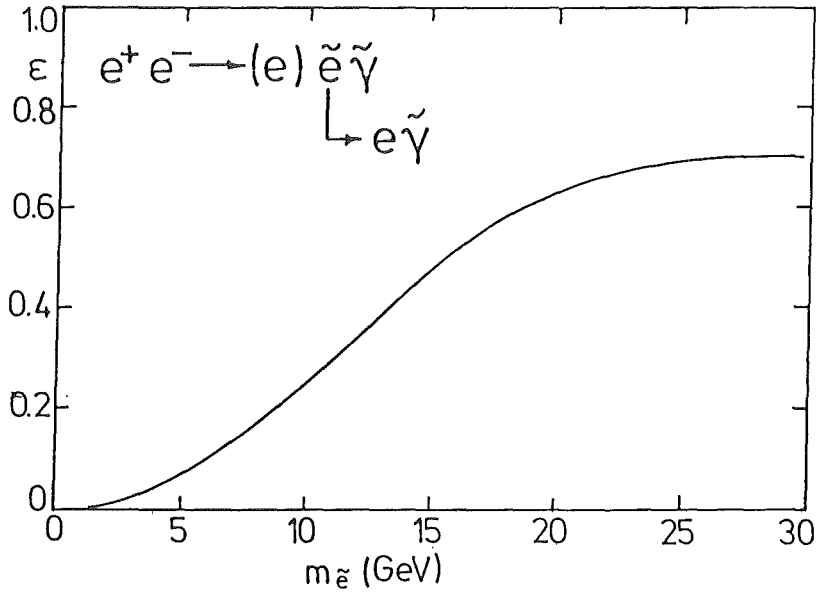

Figure 6.3: Detection efficiencies for
(a) $e^+e^- \to \widetilde{ee}$
(b) $e^+e^- \to \widetilde{\tau}\widetilde{\tau}$
(c) $e^+e^- \to (e)\widetilde{e}\widetilde{\gamma}$
$\sqrt{s} = 44$ GeV, $m_{\widetilde{\gamma}} = 0$

or $e\mu$ (Figs. 6.3a and 6.4b). This is on one hand because we considered only two track final states and on the other because the track momentum is considerably reduced by the τ decay.

In case of single $\tilde{e}$ or $\tilde{w}$ production the decay electron is distributed almost isotropically (c.f. Fig. 5.7 on page 62) for the mass region of interest ($m > E_{beam}$), giving a detection efficiency of $\sim$ 70 % in both cases (Fig. 6.3c, only $e^+e^- \to (e)\widetilde{e}\widetilde{\gamma}$

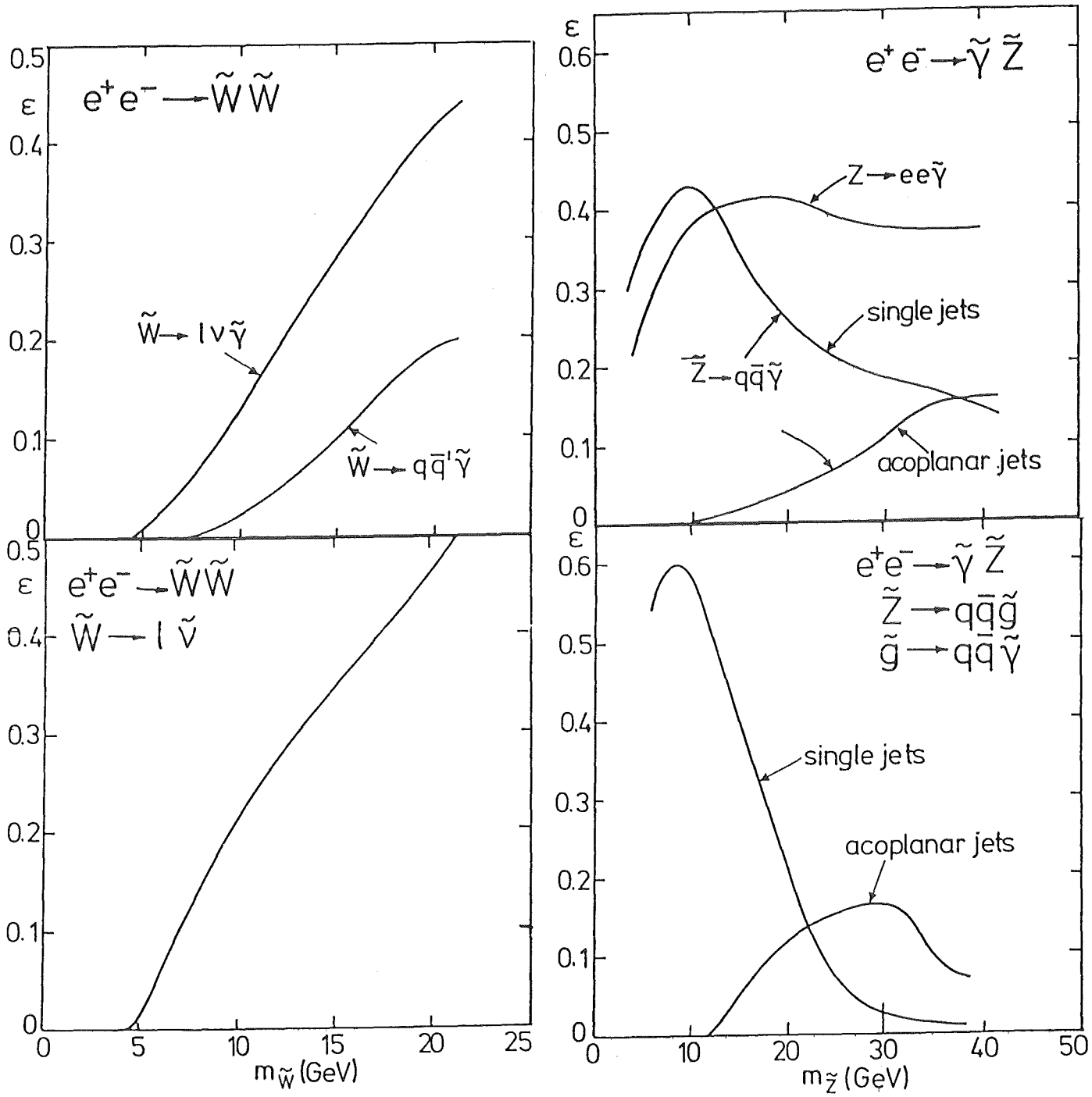

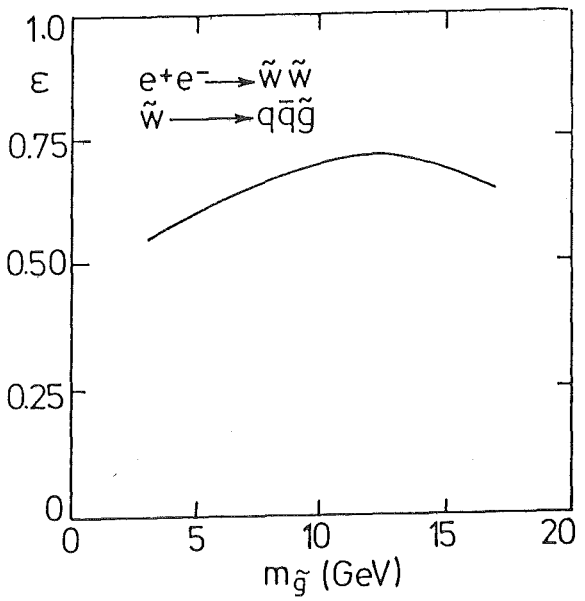

Figure 6.4: Detection efficiencies for
(a) $e^+e^- \to \tilde{w}^+\tilde{w}^-, \tilde{w} \to f\bar{f}'\tilde{\gamma}$
(b) $e^+e^- \to \tilde{w}^+\tilde{w}^-, \tilde{w} \to l\tilde{\nu}$
(c) $e^+e^- \to \tilde{\gamma}\tilde{z}, \tilde{z} \to f\bar{f}\tilde{\gamma}$
(d) $e^+e^- \to \tilde{\gamma}\tilde{z}, \tilde{z} \to q\bar{q}\tilde{g}$
(e) $e^+e^- \to \tilde{w}^+\tilde{w}^-, \tilde{w} \to q\bar{q}'\tilde{g}$
$\sqrt{s} = 44GeV, m_{\tilde{g}} = 5GeV, m_{\tilde{\gamma}} = 0, m_{\tilde{\nu}} = 0$

is shown), mainly determined by detector acceptance ($\sim$ .80) and triggering ($\sim$ .95) and tracking ($\sim$ .95) efficiencies.

For zino production in association with an invisible photino the detection efficiency for electronic final states is $\sim$ 40 %, degrading slowly for lower zino masses due to the requirement of a minimum opening angle of 10° between the electrons. It varies only slowly with the scalar electron mass. For $m_{\tilde{e}} < m_{\tilde{z}}$ the zino can decay into an electron and a real scalar electron. This leads to a variation of the detection efficiency along the line $m_{\tilde{e}} = m_{\tilde{z}}$. A scalar electron mass only slightly smaller than the zino mass leads to a soft electron from the zino decay together with an energetic electron from the decay of the scalar electron. The momentum cut of 1 GeV for the lower energy electron therefore leads to a small efficiency gap along the line $m_{\tilde{e}} = m_{\tilde{z}}$. Generally, our detection efficiency is ~50% if the scalar electron is lighter than the zino.

In case of the hadronic zino decay $\tilde{z} \rightarrow q\bar{q}\tilde{\gamma}$ (Fig. 6.4 c), as expected, at low zino masses the monojet selection is sensitive, while for higher zino masses the acoplanar jet selection becomes effective too. Note that both selections are completely orthogonal. The combined efficiency is above 30 %. A similar pattern is observed for the gluinic zino decay $\tilde{z} \rightarrow q\bar{q}\tilde{g}$ (Fig. 6.4 d). Here the monojet efficiency is higher for low zino masses due to the larger visible energy but it drops dramatically as the zino mass rises. Here the acoplanar jet selection takes over. It drops however also for zino masses above 30 GeV as here the photino produced together with the zino becomes weaker, thus giving less missing momentum. (The photino from the zino decay is relatively soft in any case due to the long decay cascade.) All said above for wino and zino decays applies equally to charged and neutral higgsinos.

Finally, Fig. 6.4 e shows the efficiency of the aplanar event selection for the process $e^+e^- \rightarrow \tilde{w}^+\tilde{w}^-$, $\tilde{w} \rightarrow q\bar{q}'\tilde{q}$, $\tilde{g} \rightarrow q\bar{q}\tilde{\gamma}$. Only a weak dependence on the gluino mass is observed. Our limit was obtained assuming a gluino mass of 5 GeV.

Chapter 7

Results and Discussion

Combining (a) the production cross sections as summarized in Appendix A with (b) the detection efficiencies determined as described in Chapter 6 and (c) luminosities determined from large angle Bhabha scattering and (d) applying radiative corrections as discussed in Section 6.1 we are able to calculate the expected number of events for a given process as function of the masses of the supersymmetric particles involved:

$$N_{exp}(\widetilde{m}) = \epsilon(\widetilde{m})(1+\delta)\sigma_0(\widetilde{m}) \int L\mathrm{d}t \tag{7.1}$$

Combining this number with the number of events actually observed in the relevant final states (Chapter 5) and with the number of events expected from conventional sources, if any, allows us to exclude certain mass ranges for supersymmetric particles (SPs). All quoted mass limits are at 95 % C.L.

In the following discussion we make the assumption that either the $\tilde{\gamma}$ or the $\tilde{\nu}$ is the LSP (lightest supersymmetric particle) unless explicitly stated otherwise. Note that the exact mass hierarchy between $\tilde{\gamma}$ and $\tilde{\nu}$ does not really matter since the decay (via one loop diagrams) will be invisible [35] in both cases ($\tilde{\nu} \rightarrow \tilde{\gamma}\nu$ or $\tilde{\gamma} \rightarrow \tilde{\nu}\nu$). If neither the $\tilde{\gamma}$ nor the $\tilde{\nu}$ are the LSP separate considerations are needed. These will be given in section 7.5.

7.1 Scalar Leptons

7.1.1 Scalar Electrons

Scalar electrons can be produced in pairs (Fig. 2.6 on page 20), or singly in assciation with a photino (Fig. 2.7 on page 21), or affect the rate of raditive photino pair production (Fig. 2.8 on page 22). Here we will consider only the first two cases. An account of a search for radiative photino pair production by CELLO is given in Ref. [50].

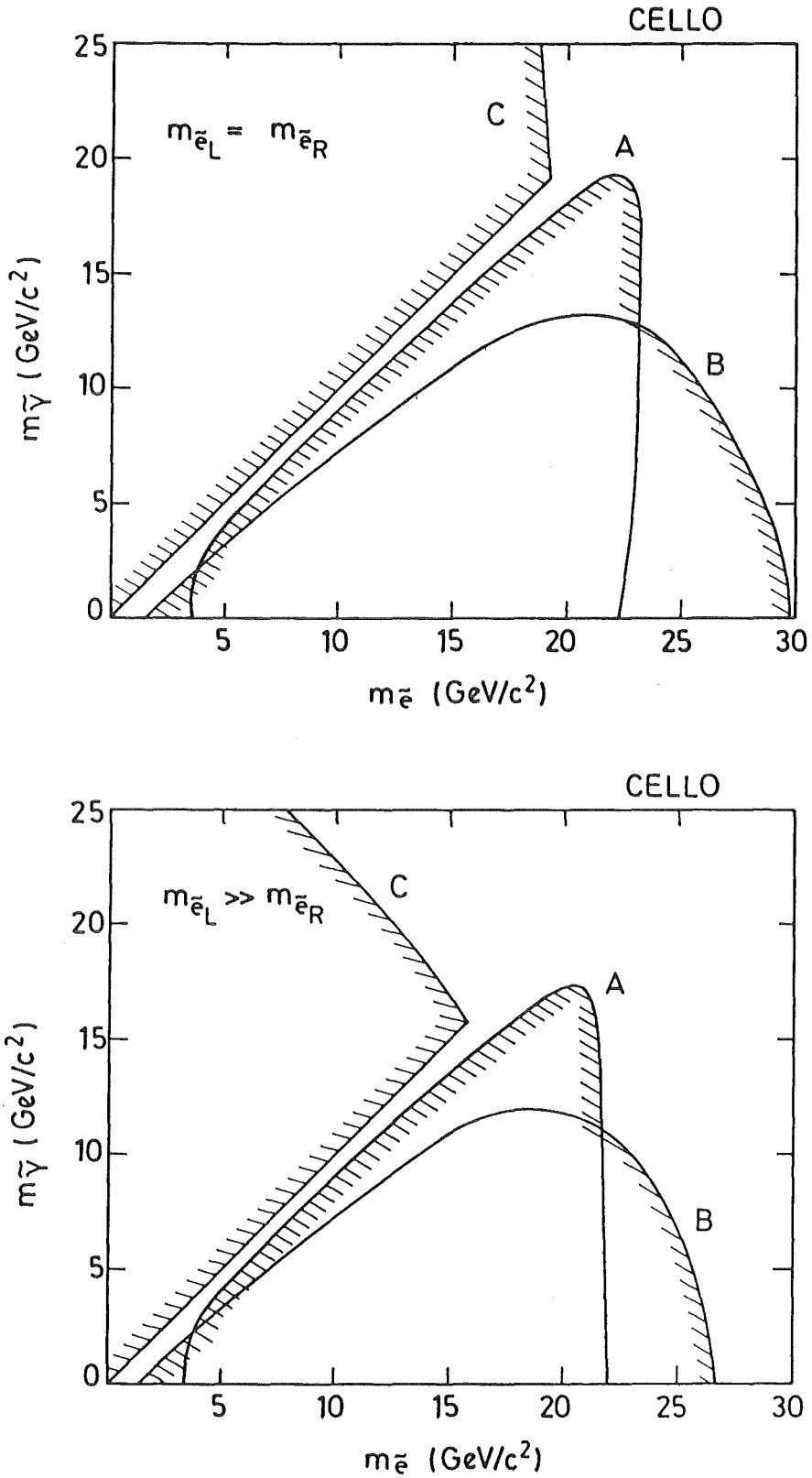

Figure 7.1: Scalar electron and photino mass domains excluded at the 95% C.L. for **(a)**: $m_{\tilde{e}_L} = m_{\tilde{e}_R}$, **(b)**: $m_{\tilde{e}_L} >> m_{\tilde{e}_R}$.
Contour A limits the domain excluded by $\tilde{e}$ pair production,
contour B that excluded by $\tilde{e}\,\tilde{\gamma}$ associated production.
Contour C limits the domain excluded for a stable $\tilde{e}$.

Using the cross section for the pair production of scalar electrons as given in Appendix A for arbitrary photino masses, the null result of our search for acoplanar electrons translates into the excluded domains limited by the contours labelled A in Figs. 7.1 a and 7.1 b, for $m_{\tilde{e}_R} << m_{\tilde{e}_L}$ and $m_{\tilde{e}_R} = m_{\tilde{e}_L}$, respectively.

To turn the result of our search for single electrons into limits on SP masses, we took the cross section for $\gamma e \rightarrow \tilde{\gamma}\tilde{e}$, as shown in Appendix A for arbitrary photino masses, and we used the equivalent photon approximation (Equ. (2.5) on page 21). The scalar electron and photino mass domains excluded by this analysis are limited by the contours labelled B in Fig. 7.1. Altogether, we exclude

$$\begin{aligned} m_{\tilde{e}_R} = m_{\tilde{e}_L} &< 29.8\ GeV \quad \text{and} \\ m_{\tilde{e}_R} &< 26.8\ GeV \quad \text{if } m_{\tilde{e}_L} >> m_{\tilde{e}_R} \end{aligned}$$

for massless photinos.

7.1.2 Scalar Taus

Scalar taus can be produced at an observable rate only in pairs. In addition, both cross section and detection efficiency are significantly lower than in the case of scalar electron pair production. This is reflected in a smaller excluded mass range which is shown in Fig. 7.2 for both the mass degenerate and the non degenerate case. For massless photinos, we exclude

$$\begin{aligned} m_{\tilde{\tau}_R} = m_{\tilde{\tau}_L} &< 20.6\ GeV \quad \text{and} \\ m_{\tilde{\tau}_R} &< 19.5\ GeV \quad \text{if } m_{\tilde{\tau}_L} >> m_{\tilde{\tau}_R} \end{aligned}$$

7.2 Gauginos

We next turn to the search for the supersymmetric partners of the weak gauge bosons. These might well be lighter than their ordinary partners, as suggested by some supergravity inspired models [38]. For definiteness, first we assume the wino and the zino to be pure gauginos and postpone the discussion of gaugino higgsino mixing.

7.2.1 Winos

Winos can be produced in pairs (Fig. 2.10 on page 24), or singly in assciation with a scalar neutrino (Fig. 2.13 on page 26), or affect the rate of radiative scalar neutrino pair production (Fig. 2.14 on page 27). Of course, the two latter cases are of interest only if the scalar neutrino is light. Here we will discuss only the first two cases. An account of a search for radiative scalar neutrino pair

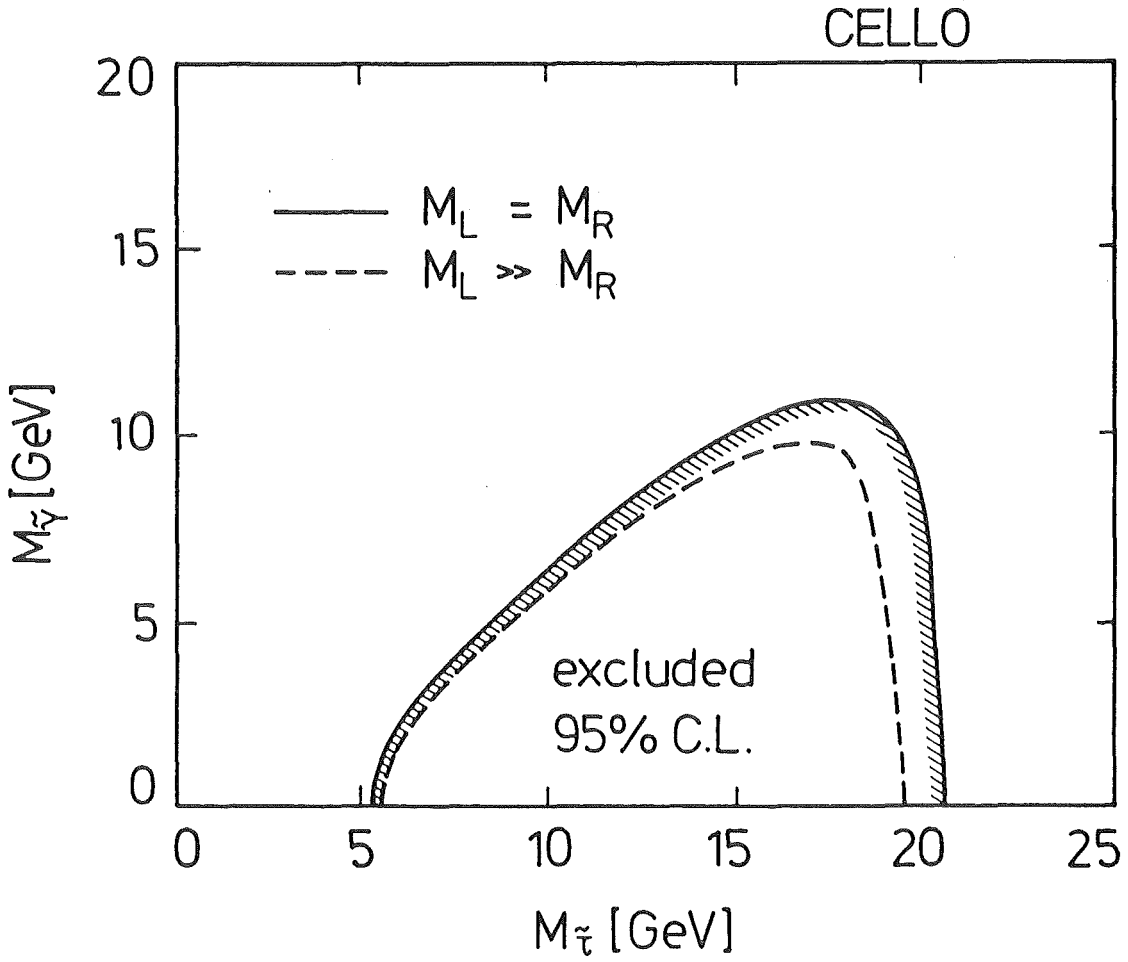

Figure 7.2: Scalar tau and photino mass domains excluded at the 95% C.L. for $m_{\tilde{\tau}_L} = m_{\tilde{\tau}_R}$ (full curve) and $m_{\tilde{\tau}_L} >> m_{\tilde{\tau}_R}$ (dashed curve).

production by CELLO is given in Ref. [50]. Depending on the mass hierarchy of the supersymmetric particles one has to consider three different cases:

7.2.1.1 Heavy gluino, heavy scalar neutrino.

In this case, only pair production is relevant. In order to get results valid irrespective of the gaugino-higgsino content within the wino we considered only the contribution from one photon annihilation.

To interpret the result of our searches for acoplanar lepton pairs, we took into account both W exchange (diagram f in Fig. 2.12 on page 25) and scalar lepton exchange (diagram e in Fig. 2.12) in the wino decay. In the latter case we assumed a scalar lepton mass of 100 GeV and we modified the $\tilde{z}$ decay matrix element given in Ref. [52]. The detection efficiency turns out to be independent

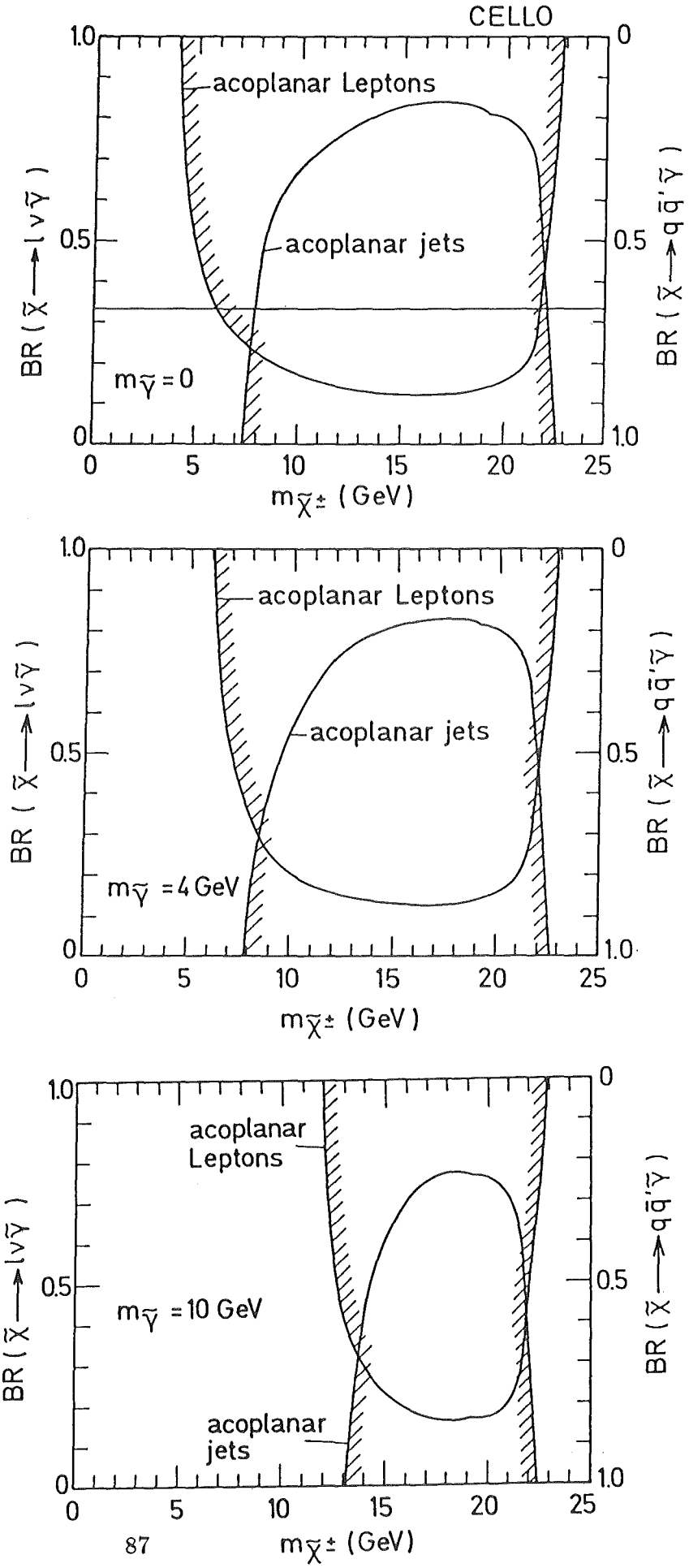

Figure 7.3: Wino masses excluded at the 95% C.L. as a function of the leptonic branching ratio, for the case where both $\tilde{g}$ and $\tilde{\nu}$ are heavy. and for $m_{\tilde{\gamma}}$ = 0, 4, and 10 GeV. The horizontal line in the $m_{\tilde{\gamma}}$ = 0 case indicates a leptonic branching ratio of $3 \star 11\%$ as expected for a wino decaying via W exchange.

of the wino decaying via W or scalar lepton exchange. The efficiency decreases for photino masses close to the wino mass because the decay leptons in this case have little energy. If the wino decay proceeds dominantly via W exchange, a branching ratio of $3 \star 11\%$ into leptons is expected. If the decay via scalar quark or lepton exchange is dominant one expects $BR(\tilde{w} \rightarrow l\nu\tilde{\gamma}) \sim 3 \star 16\%$ for the case of equal scalar quark and lepton masses. Fig. 7.3 shows the wino masses excluded as a function of the leptonic branching ratio assuming equal decay widths into e,μ, and τ, for $m_{\tilde{\gamma}} = 0,\ 4$, and $10\ GeV$.

We proceeded similarily to interpret the result of our search for acoplanar jets in terms of the mechanisms shown in Figs. 2.12 g and 2.12 h. Again, the detection efficiency is insensitive to the wino decaying via W or via scalar quark exchange. Wino mass domains excluded by these searches are also shown in Fig. 7.3.

It can be seen in Fig. 7.3a that, from the combined search for leptonic and hadronic final states, we can exclude, for massless photinos, wino masses between 7.5 and 22.4 GeV independently of the leptonic branching ratio. The upper bound of the excluded domain shows little sensitivity to the photino mass.

7.2.1.2 Light gluino.

In this case the wino would decay predominantly into $q\bar{q}\tilde{g}$ (see Fig. 2.12 i). Here also, only pair production is relevant. The events would show up in our standard multihadronic event selection with an efficiency of $\sim$ 87 % for high wino masses. From our precise measurement of the total hadronic cross section for center of mass energies up 46.78 GeV [40] we can put a lower limit of 21.0 GeV on the wino mass.

The signal to background ratio can be considerably enhanced for high wino masses close to the beam energy by looking for aplanar events. The absence of an excess of aplanar events at highest center of mass energies (we observe 9 events with an aplanarity $> .1$ while expecting 8.3 events from the aplanarity distribution observed at 38 GeV) allows to exclude masses for winos decaying mostly into $q\bar{q}\tilde{g}$

$$m_{\tilde{w}} < 22.4\ GeV$$

For massless photinos, this limit is not sensitive to the gluino mass. Note that this limit relies on a comparison of the aplanarity distributions observed at $\sqrt{s}$ =38 GeV (where wino pair production is excluded from the total hadronic cross section) and $\sqrt{s}$ = 46.6 GeV. It therefore is independent of a Monte Carlo simulation of the aplanarity distribution of multihadronic events.

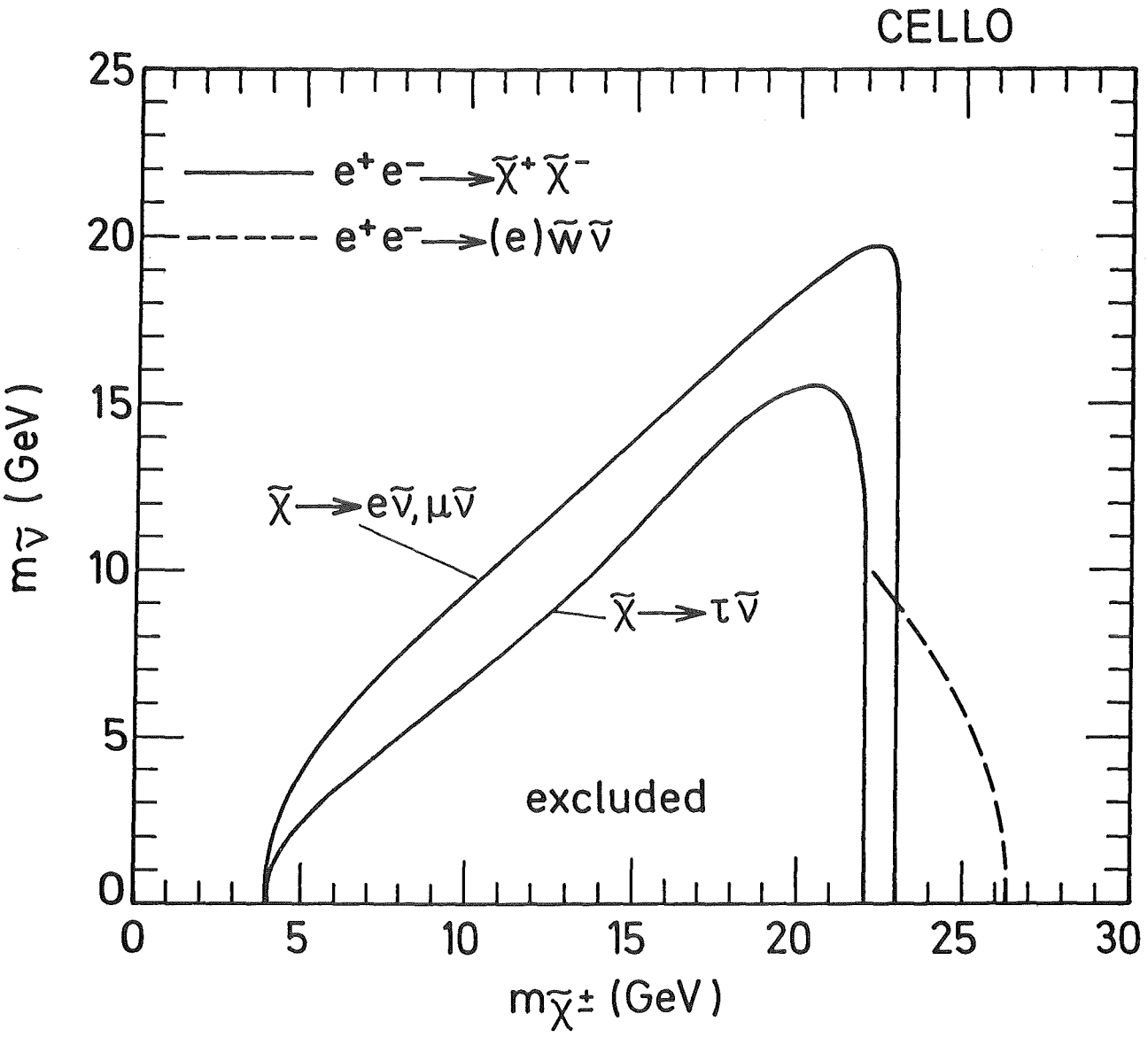

Figure 7.4: Chargino and scalar neutrino mass domains excluded at the 95% C.L. for the case of a light scalar neutrino.
The outer full contour limits the domain excluded by $\tilde{w}$ pair production, the dashed contour that excluded by associated $\tilde{w}\ \tilde{\nu}$ production in $e\gamma$ collisions, both in the case of a wino mostly gaugino-like, and with equal decay widths into e, μ and τ.
The inner full contour limits the mass domain excluded for a chargino decaying exclusively to $\tau\tilde{\nu}$, as expected if it is mostly higgsino-like.

7.2.1.3 Light scalar neutrino.

Here the only decay mechanism to consider is $\tilde{w} \rightarrow l\tilde{\nu}$ shown in Fig. 2.12 k.

From our searches for acoplanar lepton pairs, the domain of wino and scalar neutrino masses limited by the outer full contour in Fig. 7.4 could be excluded,

assuming equal decay widths into e, μ, and τ.

To interpret the result of our search for single electrons, we used the cross section for $\gamma e \rightarrow \tilde{w}\tilde{\nu}$ as given in Appendix A and the equivalent photon approximation (Equ. (2.5) on page 21). A conservative estimate is obtained this way since a full calculation taking into account all possible diagrams [39] systematically leads to a higher cross section. Our detection efficiency is around 70% for $\tilde{w}$ masses above the beam energy. For a wino purely gaugino and assuming an electronic branching ratio of 1/3, the domain limited by the dashed contour in Fig. 7.4 could be excluded. Any higgsino admixture will reduce this domain.

Altogether, for massless scalar neutrinos, we exclude wino masses below 26.3 GeV.

7.2.2 Zinos

Zinos can be produced singly in association with a photino by t-channel scalar electron exchange (Fig. 2.15 on page 28). We used the production cross section as given in Appendix A and, for the zino decay, the matrix element given in Ref. [52]. Again, as in the previous discussion on Winos we have to consider several zino decay scenarios:

7.2.2.1 Heavy gluino, heavy scalar neutrino.

In this case the zino will decay dominantly into $l\bar{l}\tilde{\gamma}$ and $q\bar{q}\tilde{\gamma}$ via scalar exchange (see Fig. 2.12 a and b on page 25). Making the assumption that all scalar partners of the quarks and leptons have equal masses, the expected branching ratios of the zino into quarks and leptons can be calculated from the known couplings. For zino masses above $b\bar{b}$ threshold and scalar masses above the zino mass one expects an electronic (hadronic) branching ration of $\sim$ 13 % (60 %).

Fig. 7.5 a shows the zino and scalar electron masses excluded by the search for acoplanar electron pairs assuming $m_{\tilde{\gamma}} = 2$ GeV (full lines) and $m_{\tilde{\gamma}} = 10$ GeV (dashed lines). Contours are shown for a 100% and 13% zino branching ratio into electrons. Note that scalar electron masses below 29.8 GeV (26.1 GeV) have been excluded for $m_{\tilde{\gamma}} = 0$ GeV (10 GeV) by our search for scalar electrons.

Zino masses excluded from the analysis of hadronic final states, namely from the search for monojets and acoplanar jets, are shown in Fig. 7.5 b as a function of the scalar electron mass for a 100% and a 60% branching ratio into $q\bar{q}\tilde{\gamma}$. The full lines correspond to a massless photino, the dashed contours are for a 10 GeV photino.

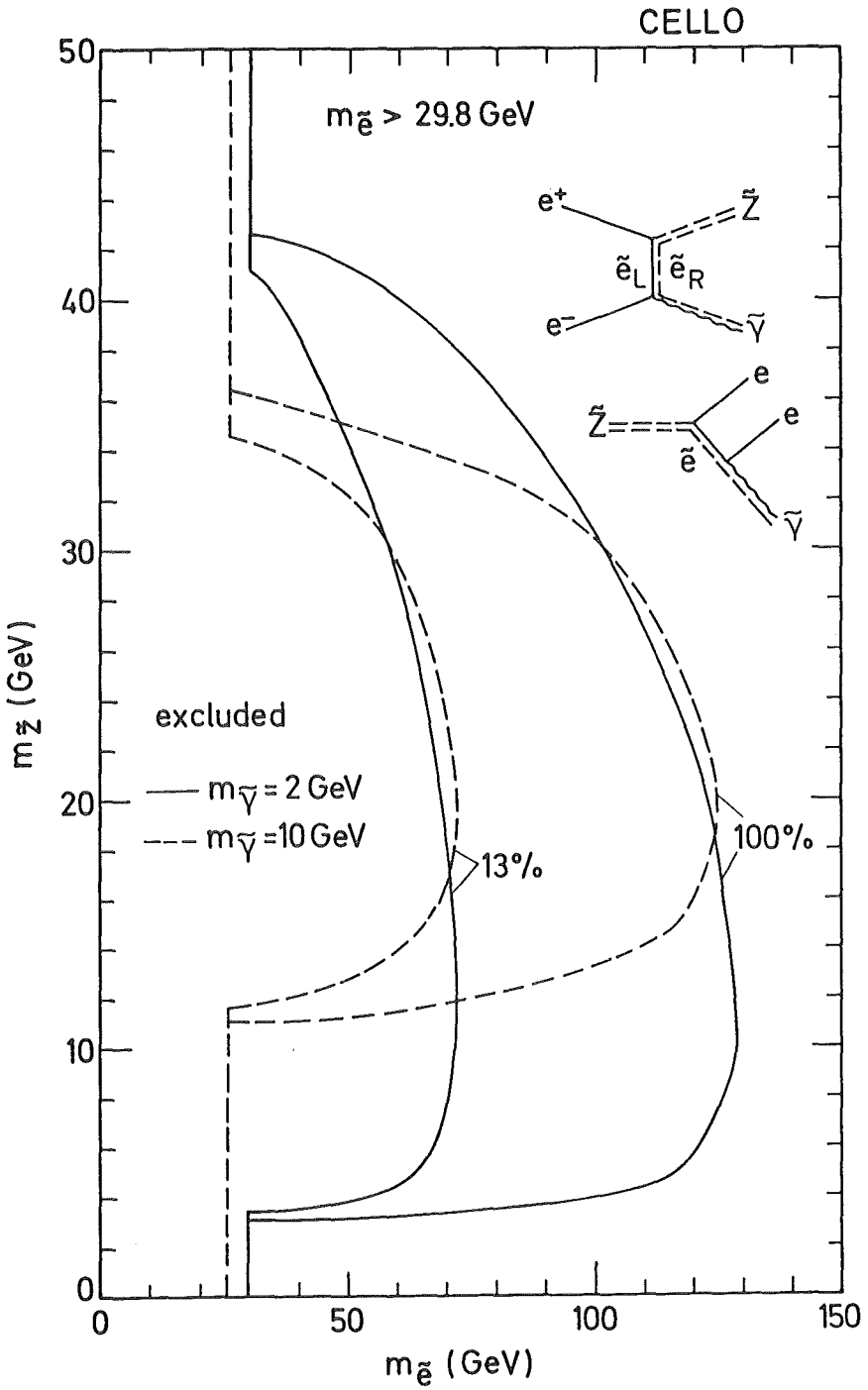

Figure 7.5: Zino and scalar electron mass domains excluded at the 95% C.L. for $m_{\tilde{\gamma}} = 2$ GeV (full lines) and $m_{\tilde{\gamma}} = 10$ GeV (dashed lines), assuming $m_{\tilde{e}_L} = m_{\tilde{e}_R}$. Scalar electron masses below 29.8 GeV (26.1 GeV) are excluded for $m_{\tilde{\gamma}} = 0$ ($m_{\tilde{\gamma}} = 10$ GeV) by the $\tilde{e}$ search.

(a) domain excluded from $\tilde{z} \to ee\tilde{\gamma}$ for two different branching ratios: 100% and 13%.

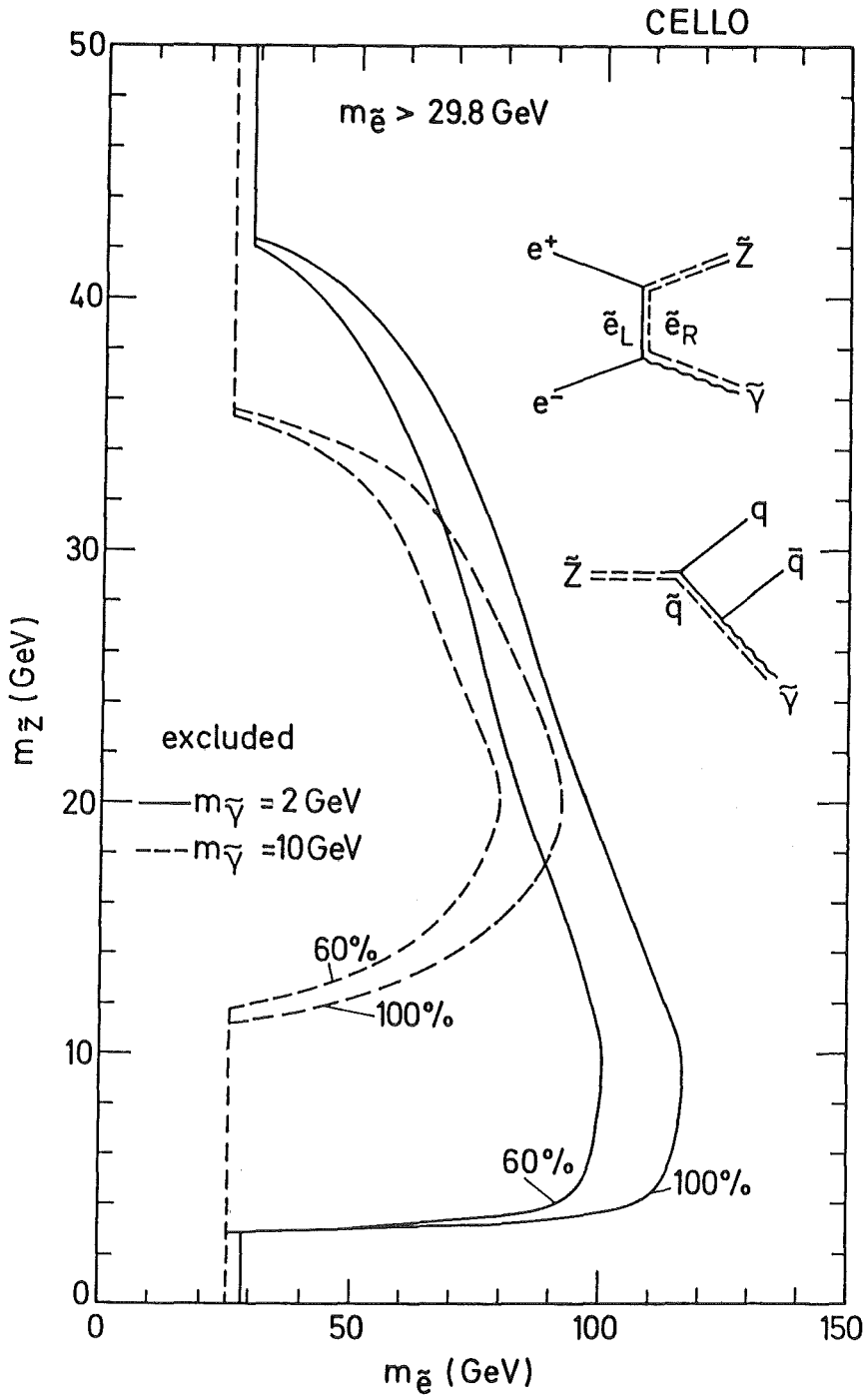

Figure 7.5:
(b) domain excluded from $\tilde{z} \to q\bar{q}\tilde{\gamma}$ for two different branching ratios: 100% and 60%.

Fig. 7.5 c shows the combined limit for $\tilde{z} \to q\bar{q}\tilde{\gamma}$ and $\tilde{z} \to ee\tilde{\gamma}$, assuming a leptonic branching ratio of 13% per lepton generation. Since we consider both leptonic and hadronic final states this result is rather insensitive to variations in the leptonic branching ratio. For $m_{\tilde{e_L}} = m_{\tilde{e_R}} < 70$ GeV, zino masses below ~31 GeV are excluded, with little dependence on $m_{\tilde{\gamma}}$ as long as smaller than 10 GeV.

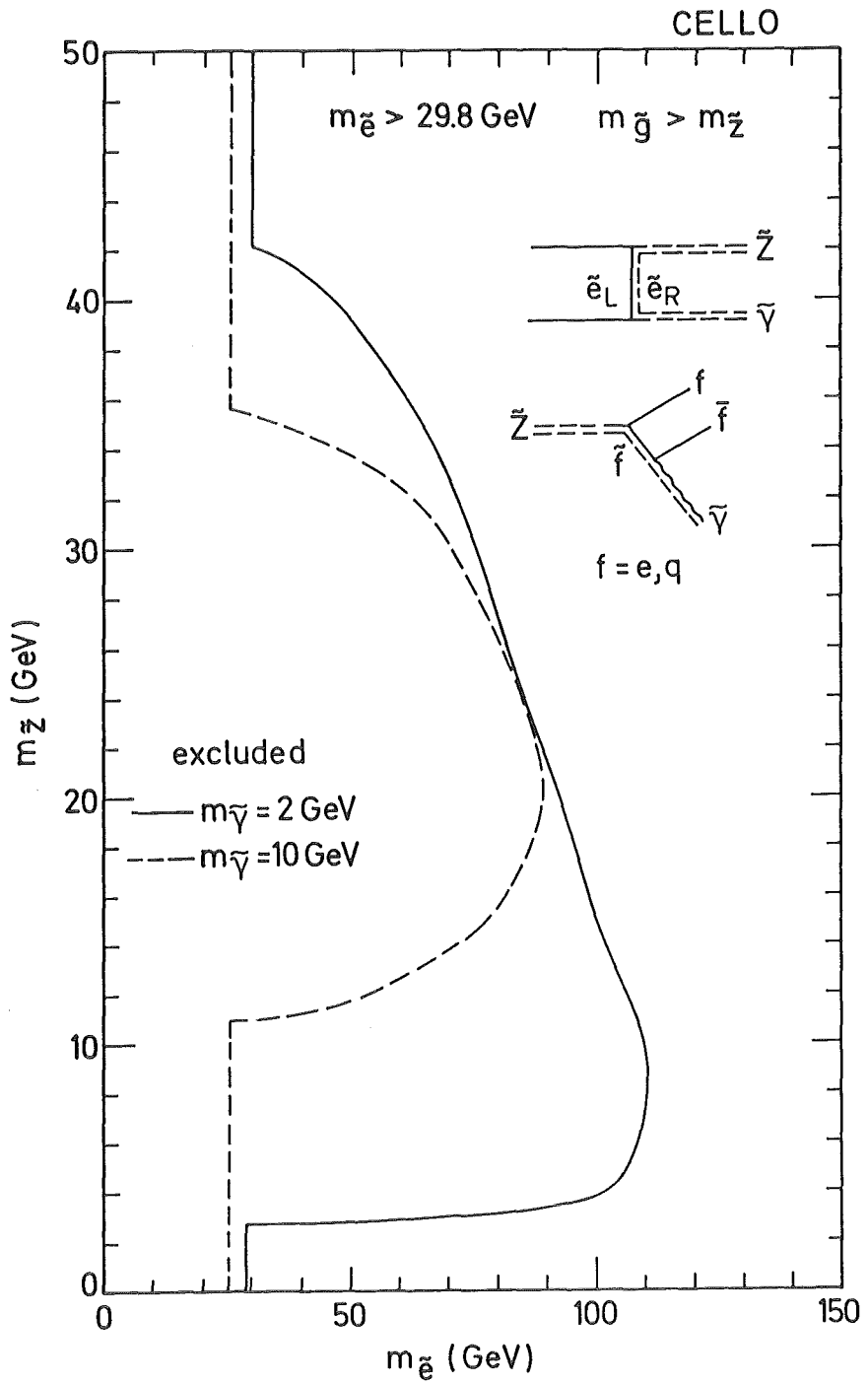

Figure 7.5
(c) domain excluded from the combination of $\tilde{z} \to ee\tilde{\gamma}$ and $\tilde{z} \to q\bar{q}\tilde{\gamma}$ assuming a hadronic (electronic) branching ratio of 60% (13%).

7.2.2.2 Light gluino.

If the gluino is lighter than the zino the dominant zino decay will be $\tilde{z} \to q\bar{q}\tilde{g}$ followed by $\tilde{g} \to q\bar{q}\tilde{\gamma}$. The searches for monojets and acoplanar jets are sensitive to this process, with the sensitivity depending on the zino mass (Fig. 6.4 d on

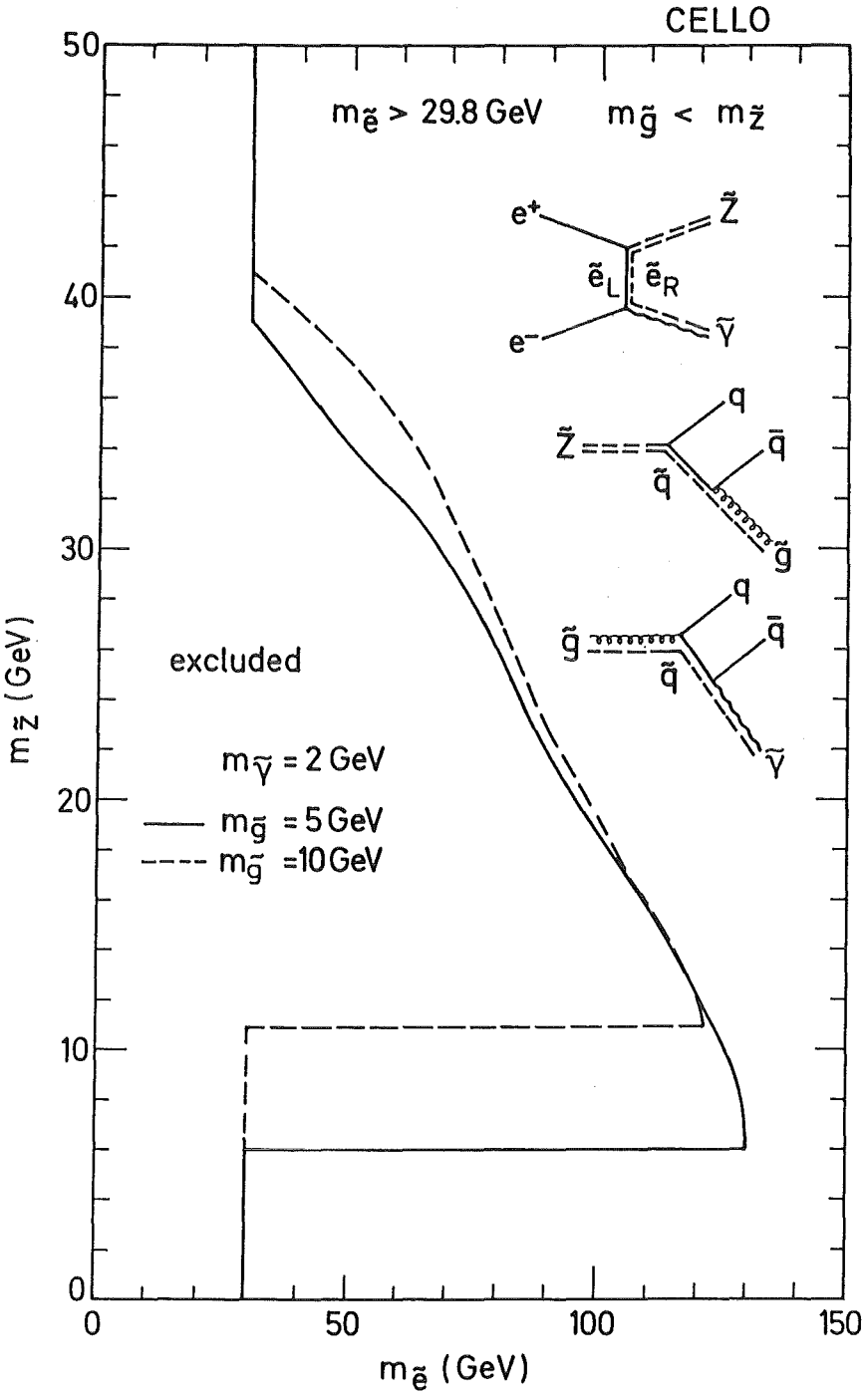

Figure 7.6: Zino and scalar electron mass domains excluded at the 95% C.L. if $\tilde{z} \rightarrow q\bar{q}\tilde{g}$ with $m_{\tilde{g}} = 5$ GeV (full line) and $m_{\tilde{g}} = 10$ GeV (dashed line) for a 100 % branching ratio into $q\bar{q}\tilde{g}$. $m_{\tilde{e}_L} = m_{\tilde{e}_R}$ is assumed. Scalar electron masses below 29.8 GeV are excluded for $m_{\tilde{\gamma}} = 0$ by our $\tilde{e}$ search.

page 80). Fig. 7.6 shows zino masses excluded by this analysis for a gluino mass assignment of 5 and 10 GeV. In both cases we have taken $m_{\tilde{\gamma}} = 2$ GeV. The contours are shown for a 100% branching ratio into $q\bar{q}\tilde{g}$ since this decay, if kinematically possible, is expected to be dominant. Here also, for $m_{\tilde{e}_L} = m_{\tilde{e}_R} < 70$ GeV, zino masses below ~30 GeV are excluded, with little dependence on the gluino mass below ~10 GeV. Zino masses below ~2 GeV cannot be excluded because of too large uncertainties in the gluino hadronization mechanism.

7.2.2.3 Light scalar neutrino.

If the scalar neutrino is light the zino will decay almost exclusively into and invisible $\tilde{\nu}\nu$ final state. In this case, which will not be considered here, zino production could still affect the rate of single photons by the reaction $e^+e^- \rightarrow \gamma\tilde{\gamma}\tilde{z}$. This possibility is studied in Ref. [15].

7.3 Higgsinos

After discussion of pure gaugino production in the previous section we now turn to the other limiting case and consider the production of pure higgsinos.

7.3.1 Charged Higgsinos

Charged Higgsinos can be produced in pairs via one photon annihilation. Again, depending on the mass of the scalar neutrino, we have to consider two cases:

7.3.1.1 heavy scalar neutrino

In this case the higgsino decays via W exchange into the lightest neutralino and a fermion pair (see Fig. 2.16 on page 29 and the discussion in section 2.4.1). This gives a signature identical to wino pair prodcution and the result shown in Fig. 7.3 are fully applicable. Since the decay proceeds via a W, just as in the case of a new heavy lepton, the expected leptonic branching fraction is 3 * 11 % independent of assumptions on the supersymmetric mass spectrum. Therefore, for $m_{\tilde{\gamma}} = 0$ we can exclude the range

$$6\ GeV < m_{\tilde{h}^{\pm}} < 22.1\ GeV\ .$$

7.3.1.2 light scalar neutrino

If the scalar neutrino is light the dominant higgsino decay will be $\tilde{h} \rightarrow \tau\tilde{\nu}$ because the $\tilde{h}l\tilde{\nu}$ coupling is proportional to the lepton mass. The search for acoplanar taus is sensitive to this process and allows us to exclude the domain in $\tilde{h}^{\pm}$ and $\tilde{\nu}$ mass

indicated by the inner full contour in Fig. 7.4. For a massless scalar neutrino we can exclude

$$4.0\ GeV < m_{\tilde{h}^{\pm}} < 22.0\ GeV\ .$$

7.3.2 Neutral Higgsinos

The second lightest neutral higgsino $\tilde{h}_2^0$ can be produced in association with the lightest one $\tilde{h}_1^0$ by annihilation into a virtual Z^0 (Fig. 2.17 on page 30). It will decay immediately into the lighter $\tilde{h}_1^0$ via a virtual Z^0 (see Fig. 2.17 and discussion in section 2.4.2). If the light $\tilde{h}_1^0$ escapes invisibly this gives the same experimental signature as single zino production, namely acoplanar leptons and, depending on the $\tilde{h}_2^0$ mass, monojets or acoplanar jets. The advantage of this process as compared to $e^+e^- \rightarrow \tilde{\gamma}\tilde{z}$ is that both the production rate and the relative hadronic and leptonic branching fractions can be predicted independent of the supersymmetric mass spectrum [37]. The hadronic (leptonic) branching ratio is determined by the couplings of the quarks and leptons to the Z^0 and by the available phase space. It varies between 50 (5.5) % and 70 (3.5) % for $\tilde{h}_2^0$ masses between 2 and 30 GeV.

Fig. 7.7 shows the upper limit on the cross section for $e^+e^- \rightarrow \tilde{h}_1^0\tilde{h}_2^0$ obtained by combining the searches for acoplanar electrons, acoplanar jets, and monojets and assuming the $\tilde{h}_1^0$ to be light ($<$ O(1 GeV)). Also show is the expected cross section for the case of maximum mixing (see [37,30]). Then $\tilde{h}_2^0$ masses in the range

$$2.0\ GeV \lesssim m_{\tilde{h}_2^0} < 33.4\ GeV\ .$$

can be excluded. This is an update of a result obtained in a previous CELLO publication [41].

7.4 Gaugino Higgsino Mixing

In general, photino, zino, and the neutral higgsinos are expected to mix forming so called neutralino mass eigenstates:

$$\tilde{\chi}_i^0 = \alpha_i\tilde{\gamma} + \beta_i\tilde{z} + \gamma_i\tilde{h}_1^0 + \delta_i\tilde{h}_2^0, \qquad i = 1\ldots4 \tag{7.2}$$

in very much the same way as the neutral gauge bosons of the U(1) and SU(2) mix giving the photon and the Z^0 (see Equ. (.1) on page 2). Similarily winos and charged higgsinos may mix forming charginos.

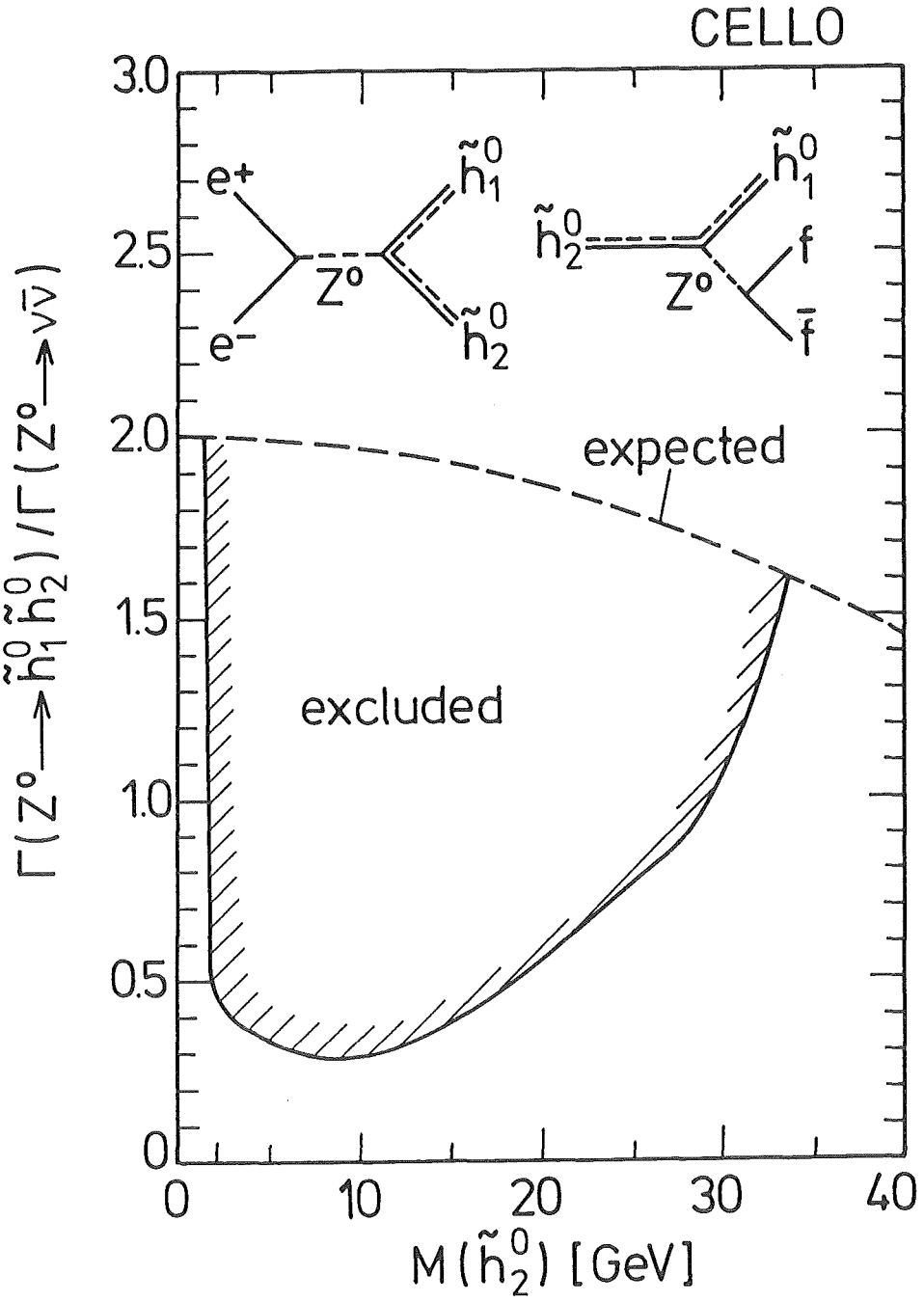

Figure 7.7: Upper limit on the decay width of a (real) Z^0 into the lightest ($\tilde{h}_1^0$) and second lightest ($\tilde{h}_2^0$) higgsino as function of the mass of the $\tilde{h}_2^0$ assuming $\tilde{h}_1^0$ to be light ($\lesssim$ 1 GeV). Also indicated is the decay width expected in the case of maximum mixing.

7.4.1 Charginos

Having considered all potential decay modes for both a wino and a charged higgsino we are able to put a lower limit of 22 GeV on the chargino mass, independent of the supersymmetric mass particle spectrum and independent of gaugino higgsino mixing.

7.4.2 Neutralinos

The associated production of the lightest and the second lightest neutralino $e^+e^- \rightarrow \tilde{\chi}_1^0\tilde{\chi}_2^0$ may proceed via scalar electron exchange or via a virtual Z^0 in s-channel, depending on the relative gaugino content in $\tilde{\chi}_1^0$ and $\tilde{\chi}_2^0$. The $\tilde{\chi}_2^0$ decay may be a mixture of all the processes discussed in section 7.2.2 and 7.3.2. As we have considered all these potential decays (with the exception of $\tilde{z} \rightarrow \tilde{\nu}\nu$) we may conclude that $2GeV \lesssim m_{\tilde{\chi}_2^0} \lesssim 30GeV$ is excluded independent of gaugino higgsino mixing if $m_{\tilde{e}} \lesssim 70GeV$, $m_{\tilde{\nu}} > m_{\tilde{\chi}_2^0}$, and the $\tilde{\chi}_1^0$ is light ($m_{\tilde{\chi}_1^0} <$ few GeV).

Note, however, that if the $\tilde{\chi}_1^0$ is mainly $\tilde{\gamma}$ -like and the $\tilde{\chi}_2^0$ is mainly a higgsino, the production cross section may become very low since the Z^0 does not couple to $\tilde{\gamma}$ and $\tilde{h}^0$ (Z^0 amplitude) and the $\tilde{h}^0 e\tilde{e}$ coupling is small ($\tilde{e}$ -exchange amplitude).

7.5 Neither $\tilde{\gamma}$ nor $\tilde{\nu}$ are the LSP

Having failed to detect any signal of supersymmetry under the assumption that either the $\tilde{\gamma}$ or the $\tilde{\nu}$ is the LSP we are led to contemplate other possiblitities. We will consider in turn:

- a charged LSP.
- a neutral LSP, with the photino as NLSP (next to lightest SP)
- a neutral LSP, with a heavy photino.

7.5.1 Search for Charged Stable Supersymmetric Particles

In this subsection, we investigate the (unlikely) possibility that the LSP be a charged stable particle. As for any charged supersymmetric particle the dominant production mechanism will be pair production via s-channel one photon exchange. In addition, if the produced LSP is a scalar electron, photino exchange will also contribute; and similarily scalar neutrino exchange for chargino pair production. However, in the latter case, because of the small electron mass, the t-channel

exchange contribution is reduced by the a priori arbitrary amount of higgsino component within the chargino. Since the interference between $\tilde{\gamma}$ and $\tilde{\nu}$ exchange is always constructive [27], we will ignore the contribution from scalar neutrino exchange to obtain safe limits on chargino production, independent of its gaugino content.

Pair production of new charged stable particles will appear in CELLO as an excess in the muon pair production cross section. We have measured [42] $R_{\mu\mu}=\sigma_{\mu\mu}/\sigma_{QED}=0.98\pm0.04\pm0.04$ at $\sqrt{s}$=43.0 GeV, where $\sigma_{QED} = 4\pi\alpha^2/3s$. The momentum and acceptance cuts applied in this analysis were $p > 10$ GeV/c and $|cos(\theta)| < .85$ for both tracks.

This result allows to exclude the region

$$m_{\tilde{w}} < 19.6\ GeV$$

for the mass of a stable wino. The production cross section for scalar muons or taus is considerably smaller. This is reflected in a less stringent limit of

$$\begin{aligned} m_{\tilde{l}_R} = m_{\tilde{l}_L} &< 17.6\ GeV \quad \text{and} \\ m_{\tilde{l}_R} &< 15.4\ GeV \quad \text{if } m_{\tilde{l}_L} >> m_{\tilde{l}_R}. \end{aligned}$$

Using the production cross section given in Appendix A, scalar electron and photino mass domains can be excluded; they are limited by the contours labelled C in Figs. 7.1 a or b, depending whether $m_{\tilde{e}_R} << m_{\tilde{e}_L}$ or $m_{\tilde{e}_R} = m_{\tilde{e}_L}$.

7.5.2 Unstable Photino

Assuming the LSP should be neutral and colourless remaining candidates after the photino and the scalar neutrino are a higgsino, a light gravitino, or possibly a zino. In this case the photino would be unstable decaying into a photon and the LSP $\widetilde{X}^0$. This, of course, would have drastic consequences on the signature of photinos. This case was discussed in Chapter 1. There we concluded from searches for unstable photinos at PETRA [15,16,17,18] that a photino decaying into photon and a $\widetilde{X}^0$ inside a detector is excluded for photino masses below $\lesssim$ 20 GeV and $\tilde{e}$ masses $\lesssim$ 100 GeV (see Fig. 1.2 on page 11).

7.5.3 The Case of Heavy Photinos

We now suppose that the photino is too heavy to play a role in the search for supersymmetric particles at PETRA energies, and we will consider the other neutral colorless LSP candidates.

If the LSP is the gravitino, and if it is not vanishingly light, it practically decouples [61]. The NLSP then effectively plays the role of the LSP, and no additional discussion is therefore needed in this case.

If the LSP is a very light gravitino, or a zino, or a higgsino:

- The limit for scalar taus is practically unaltered.
- The limit obtained in section 7.1.1 from the associated production of a photino and a scalar electron no longer applies. The limit from pair production may degrade somewhat because the contribution from t-channel exchange of the LSP may decrease. The one photon annihilation amplitude remains unaffected.
- The limits obtained in section 7.2.1 and 7.3.1 on charginos are practically unaffected.
- The limits obtained in section 7.2.2 on zinos no longer apply. The neutral higgsino limit from section 7.3.2 remains valid, although the production cross section may degrade as it depends on the higgsino content of the LSP. The effect of a reduced cross section can be derived from Fig. 7.7.

If the LSP is a scalar neutrino [26]:

- Because scalar leptons will decay to their associated scalar neutrino and a virtual W in a way very similar to the wino decays shown in Figs. 2.12 f and h the limits on scalar electrons, muons and taus become similar to those obtained for the wino in subsection 7.2.1.1, slightly worse however since scalars rather than fermions are pair produced here.
- The chargino limits for the case of a light scalar neutrino (subsections 7.2.1.3 and 7.3.1.2) fully apply.
- The zino limit of section 7.2.2 no longer applies as the zino would decay invisibly into $\tilde{\nu}\nu$. The neutral higgsino limit (section 7.3.2) does still apply as far as the condition that the $\tilde{h}_1^0$ is relatively light is fulfilled. Note, however, that even a small zino admixture to the $\tilde{h}_2^0$ would make the invisible decay $\tilde{h}_2^0 \rightarrow \tilde{\nu}\nu$ dominant.

7.6 Summary and Conclusions

Given the unavoidable complexity involved in the presentation of supersymmetric particle (SP) mass limits if one wishes to take into account all possible choices for the lightest supersymmetric particle (LSP), we prefer to summarize and discuss

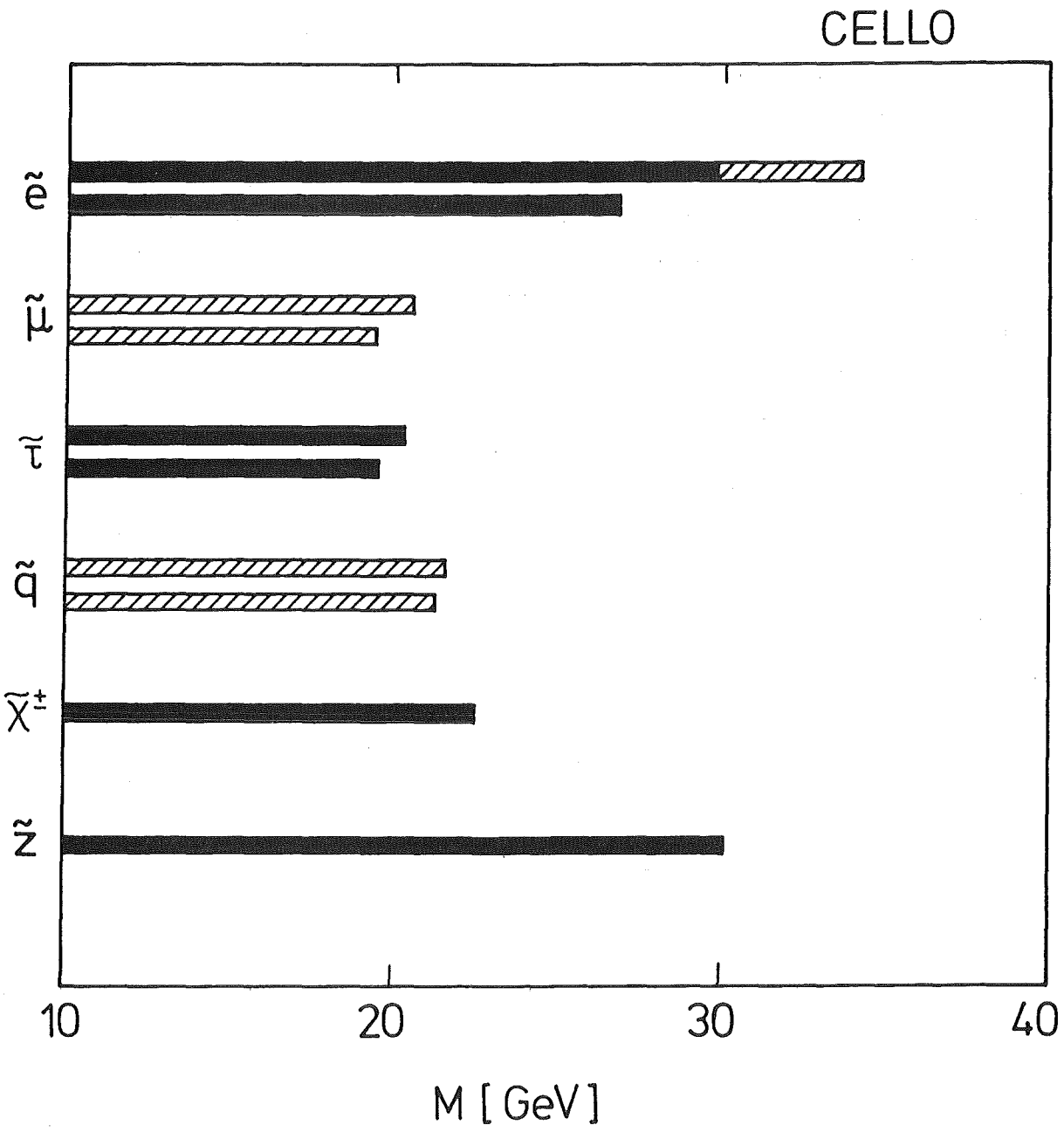

Figure 7.8: Supersymmetric particle mass limits obtained by CELLO at 95 % C.L. under the assumption of a massless photino. The limits obtained in this thesis are indicated by full bars. Also shown are limits on scalar muons and quarks [15]. The limit on scalar electrons can be improved by a search for single photons from radiative photino pair production via scalar electron exchange [50]. For the scalars, the upper bar corresponds to $m_L = m_R$ and the lower one to $m_L >> m_R$. The zino mass limit is shown for $m_{\tilde{e}_L} = m_{\tilde{e}_R} = 70$ GeV.

our results under the single but also most common assumption that the LSP is the photino. Assuming a low mass (< few GeV) photino Fig. 7.8 then shows in a pictorial way the domains we have excluded, at the 95 % C.L., for the masses of various SPs. The limit on scalar electrons can be improved by a search for radiative photino pair production. The results of such a search by CELLO [50] which was not subject of this thesis is also indicated.

The limits from pair production are fundamentally restricted by the available center of mass energy. As far as e^+e^- experiments are concerned, the best limits therefore come from PETRA (this results and Refs. [15,43,45]), and they should not be improved in the near future, at least until sufficient data has been collected at TRISTAN or SLC. Some others are essentially limited by the accumulated luminosity, namely those which result from the search for a t-channel propagator effect ($\tilde{e}$ for massless photinos). In this case, the best present limits come from PEP [44,45], but the CELLO results [50] should be significantly improved with the analysis of the 1986 run at 35 GeV center of mass energy in which a luminosity of $\sim$ 90 pb^{-1} has been accumulated. Finally, some limits suffer from both limitations ($\tilde{e}$ for higher photino masses, $\tilde{z}$); in this case, the most constraining results come from PETRA.

As far as non e^+e^-experiments are concerned, the most stringent limits come from the UA1 experiment [46] at the CERN $p\bar{p}$ collider, but up to now results have been presented only for scalar quarks and gluinos. For the other supersymmetric particles, it is unlikely that mass limits at the level of those obtained in e^+e^-experiments will be obtained at hadron colliders in the short run, except perhaps for the wino from the search for the decay $W \rightarrow \tilde{w}\tilde{\gamma}$.

Appendix A

Cross Sections for Supersymmetric Reactions in e^+e^- Interactions

Here we compile total and differential cross sections for all the reactions discussed in Chapter 2 and summarized in Tab. 2.1 on page 16. The relevant Feynman diagrams were shown in Chapter 2.

All cross sections are given for unpolarized beams. Z^0 contributions in the s-channel were neglected unless explicitly stated otherwise. For definiteness, in all cases mass eigenstates were assumed to coincide with the weak interaction eigenstates, i.e. no mixing. The consequences of mixing are discussed in Chapter 7.

All cross sections depend on the mass of the particles produced. In particular, a factor β always appears, where βE is the momentum of the final state particles. In case of the production of two particles of equal mass m β is simply:

$$\beta = \sqrt{1 - \frac{4m^2}{s}}. \tag{A.1}$$

If two particles of mass m_1 and m_2 are produced β is given by

$$\beta = \sqrt{\left(1 - \frac{(m_1 + m_2)^2}{s}\right)\left(1 - \frac{(m_1 - m_2)^2}{s}\right)}. \tag{A.2}$$

Differential cross sections will sometimes be expressed in terms of the momentum transfer squared t which reads in terms of the final particle mass m_f and the scattering angle Θ (neglecting m_i):

$$t = (p_i - p_f)^2 = m_f^2 + \frac{s}{2}\left(\beta\cos\Theta - \sqrt{\frac{4m_f}{s} + \beta^2}\right). \tag{A.3}$$

A.1 Matter Scalars (Squarks and Sleptons)

Scalar quarks and leptons can be produced via s-channel one photon annihilation.

$$\sigma(e^+e^- \to \tilde{f}_R\bar{\tilde{f}}_R) = N \cdot Q^2 \frac{\pi\alpha^2}{3s}\beta^3 , \qquad \text{for } f = \mu, \tau, q \tag{A.4}$$

$$\frac{\mathrm{d}\sigma(e^+e^- \to \tilde{f}_R\bar{\tilde{f}}_R)}{\mathrm{d}\cos\theta} = N \cdot Q^2 \frac{\pi\alpha^2}{4s}\beta^3 \sin^2\theta \tag{A.5}$$

Q is the fermion charge. N is a color factor, $N = 1$ for sleptons and $N = 3$ for squarks. In the case of mass degenerate $\tilde{f}_L$ and $\tilde{f}_R$ the cross section is doubled.

A.2 Scalar Electrons

A.2.1 Pair Production

For scalar electrons in addition to the one photon annihilation also t-channel photino exchange contributes to the cross section. It therefore depends also on the photino mass [20]:

$$\sigma(e^+e^- \to \tilde{e}_R^+\tilde{e}_R^-) = \frac{\pi\alpha^2}{8s}\beta\left[-(20 + \frac{4}{3}\beta^2 + 4\mu^2) + \frac{4 + 4\mu^2 + (1 + \beta^2 + \mu^2)^2}{\beta}\ln\frac{(1+\beta)^2 + \mu^2}{(1-\beta)^2 + \mu^2}\right] \tag{A.6}$$

$$\frac{\mathrm{d}\sigma(e^+e^- \to \tilde{e}_R^+\tilde{e}_R^-)}{\mathrm{d}\cos\theta} = \frac{\pi\alpha^2}{8s}\beta^3\sin^2\theta\left[1 + \left(1 - \frac{4K}{1 - 2\beta\cos\theta + \beta^2 + \mu^2}\right)^2\right] \tag{A.7}$$

where $\mu = m_{\tilde{\gamma}}/E_{beam}$.

If the partners of the right handed and left handed electron are degenerate in mass, this cross section is doubled. In the case of non vanishing photino mass the cross section is additionally enhanced by a contribution from $e^+e^- \to \tilde{e}_L\,\tilde{e}_R$ via t-channel $\tilde{\gamma}$ exchange:

$$\sigma(e^+e^- \to \tilde{e}_L^+\tilde{e}_R^-, \tilde{e}_R^+\tilde{e}_L^-) = \frac{8\pi\alpha^2}{s}\beta\frac{\mu^2}{(1 + \beta^2 + \mu^2)^2 - 4\beta^2} \tag{A.8}$$

$$\frac{\mathrm{d}\sigma(e^+e^- \to \tilde{e}_L^+\tilde{e}_R^-, \tilde{e}_R^+\tilde{e}_L^-)}{\mathrm{d}\cos\theta} = \frac{\pi\alpha^2}{s}\beta\left(\frac{\mu}{1 - 2\beta\cos\theta + \beta^2 + \mu^2}\right)^2 \tag{A.9}$$

Here the scalar electrons are produced in s-wave leading to a threshold behavior $\propto \beta$. Therefore, near threshold the $e^+e^- \to \tilde{e}\tilde{e}$ cross section is enhanced for non-zero photino masses.

A.2.2 Single Production in $e\gamma$ Collisions

The cross section for the supersymmetric analogue of Compton scattering reads [23]:

$$\sigma(e\gamma \ \to \tilde{e}_R\tilde{\gamma}, s) = \frac{\pi\alpha^2}{2s}\left[\eta(1+7\frac{\Delta}{s}) - 4\frac{\Delta}{s}(1+\frac{\Delta}{s})\ln\frac{\Delta+s(1+\eta)}{\Delta+s(1-\eta)}\right] \qquad \text{(A.10)}$$

$$\begin{aligned}\frac{\mathrm{d}\sigma(e^+e^- \to \tilde{e}_R\tilde{\gamma})}{\mathrm{d}\cos\Theta} \quad = \quad & \frac{\pi\alpha^2}{2s}\beta \ \left\{\frac{s+t-m_{\tilde{e}}^2}{s}\right. \\ & -\frac{(m_{\tilde{\gamma}}^2-t)(t+m_{\tilde{e}}^2)}{(t-m_{\tilde{e}}^2)^2} \\ & \left.+\frac{(m_{\tilde{\gamma}}^2(-2\Delta-s)-t(-2\Delta+s)}{s(t-m_{\tilde{e}}^2)}\right\}\end{aligned} \qquad \text{(A.11)}$$

where

$$\eta^2 = 1-2\frac{\Sigma}{s}+\frac{\Delta^2}{s^2}, \qquad \Sigma = m_{\tilde{e}}^2+m_{\tilde{\gamma}}^2, \qquad \Delta = m_{\tilde{e}}^2-m_{\tilde{\gamma}}^2, \qquad t=(p_e-p_{\tilde{\gamma}})^2.$$

Again, in the case of mass degenerate $\tilde{e}_L$ and $\tilde{e}_R$ the cross section is doubled.

A.2.3 Photino Pair Production via $\tilde{e}$ Exchange

The total cross section for this process is [24]

$$\sigma(e^+e^- \to \tilde{\gamma}\tilde{\gamma}, s) = \frac{2\pi\alpha^2}{s}\beta\left(\Delta^4+\frac{s}{2}m_{\tilde{e}}^2\right)\left[\frac{1}{\Delta^4+m_{\tilde{e}}^2}-\frac{1}{s\beta(\Delta^2+\frac{s}{2})}\ln\left(\frac{\Delta^2+\frac{s}{2}(1+\beta)}{\Delta^2+\frac{s}{2}(1-\beta)}\right)\right] \qquad \text{(A.12)}$$

with $\Delta = m_{\tilde{e}}^2 - m_{\tilde{\gamma}}^2$. It is doubled in the case of mass degenerate $\tilde{e}_L$ and $\tilde{e}_R$.

A.3 Gauginos

A.3.1 Wino Pair Production

Taking into account both s-channel γ and Z^0 exchange and t-channel $\tilde{\nu}$ exchange (assuming only one scalar neutrino species to contribute) the total and differential

cross section reads [28]:

$$\sigma(e^+e^- \to \tilde{w}^+\tilde{w}^-) = \frac{\pi\alpha^2}{s}\beta \left\{\frac{C_s}{3s^2}(2s^2+4sm_{\tilde{w}}^2)\right.$$
$$+C_t\left[1+\frac{2\Delta\Lambda}{s\beta}+\frac{\Delta^2}{m_{\tilde{\nu}}^4+m_{\tilde{w}}^4+m_{\tilde{\nu}}^2(s-2m_{\tilde{w}}^2)}\right]$$
$$\left.+\frac{C_{st}}{s}\left[(m_{\tilde{\nu}}^2-\frac{s}{2}-m_{\tilde{w}}^2)+\frac{\Lambda}{s\beta}(\Delta^2+m_{\tilde{w}}^2 s)\right]\right\} \quad \text{(A.13)}$$

where $\Delta = m_{\tilde{w}}^2 - m_{\tilde{\nu}}^2$, $\Lambda = \ln\frac{s(1-\beta)+2\Delta}{s(1+\beta)+2\Delta}$ and

$$\frac{\mathrm{d}\sigma(e^+e^- \to \tilde{w}^+\tilde{w}^-)}{\mathrm{d}\cos\Theta} = \frac{\pi\alpha^2}{2s}\beta \left\{2C_s\frac{(t-m_{\tilde{w}}^2)^2+m_{\tilde{w}}^2 s}{s^2}\right.$$
$$+C_t\frac{(t-m_{\tilde{w}}^2)^2}{(t-m_{\tilde{\nu}}^2)^2} \quad \text{(A.14)}$$
$$\left.+C_{st}\frac{(t-m_{\tilde{w}}^2)^2+m_{\tilde{w}}^2 s}{s(t-m_{\tilde{\nu}}^2)}\right\}$$

where $t = (p_e - p_{\tilde{w}})^2$ and (taking into account also the Z^0 contribution in s-channel)

$$C_s = 2 - \frac{L_e+R_e}{sin^2\theta_W(1-\frac{M_Z^2}{s})} + \frac{L_e^2+R_e^2}{4\sin^4\Theta_W(1-\frac{M_Z^2}{s})^2} \sim 2$$

$$C_t = \frac{1}{4\sin^4\Theta_W}$$

$$C_{st} = \frac{-1}{sin^2\theta_W}\left(1-\frac{L_e}{sin^2\theta_W(1-\frac{M_Z^2}{s})}\right) \sim \frac{-1}{sin^2\theta_W}$$

$L_e = -1 + 2sin^2\theta_W$ and $R_e = 2sin^2\theta_W$ are the couplings of the left and right handed electron to the Z^0.

A.3.2 Single Wino Production

The $e\gamma$ cross section reads [29]:

$$\sigma(e\gamma \to \tilde{w}\tilde{\nu}) = \frac{\pi\alpha^2}{2s\ \sin^2\theta_W}\beta$$
$$\left\{-3(1+\frac{\Delta}{s})-\frac{16\Delta m_{\tilde{w}}^2}{(s+\Delta)^2-s^2\beta^2}+\frac{2}{\beta}\left[1+\frac{2\Delta}{s}(1+\frac{\Delta}{s})\right]\ln\frac{1+\beta+\Delta/s}{1-\beta+\Delta/s}\right\} \quad \text{(A.15)}$$

$$\frac{\mathrm{d}\sigma(e^+e^- \to \tilde{w}\tilde{\nu})}{\mathrm{d}\cos\Theta} = \frac{\pi\alpha^2}{4s\ sin^2\theta_W}\beta \left\{ \frac{2(m_{\tilde{w}}^2 - t)}{s} \right.$$

$$- \frac{4(s+\Delta)(t-m_{\tilde{\nu}}^2)}{s(t-m_{\tilde{w}}^2)} \qquad \text{(A.16)}$$

$$\left. +2\frac{m_{\tilde{w}}^2 m_{\tilde{\nu}}^2 - t(m_{\tilde{w}}^2+s)}{(t-m_{\tilde{w}}^2)^2} \right\}$$

where $t = (p_e - p_{\tilde{\nu}})^2$ and $\Delta = m_{\tilde{w}}^2 - m_{\tilde{\nu}}^2$.

A.3.3 $\tilde{\nu}$ Pair Production via $\tilde{w}$ and Z^0 Exchange

Scalar neutrinos can be pair produced via Z^0 exchange and (in case of the $\tilde{\nu}_e$) also via $\tilde{w}$ exchange in t-channel. If the scalar neutrino is either stable or decays invisibly e.g. into $\tilde{\gamma}\nu$ the only possibility to detect this process is radiation tagging of the invisible final state. Here only the total cross section is relevant. It reads [28]

$$\sigma(e^+e^- \to \tilde{\nu}_e\tilde{\nu}_e) = \frac{\pi\alpha^2}{4sin^4\theta_W s^2} \left\{ E_t \cdot [-2s\beta + (s+2\Delta)\Lambda] \right.$$

$$E_s \cdot \frac{s^3\beta^3}{6(s-M_Z^2)^2}$$

$$\left. E_{st} \cdot \frac{1}{(s-M_Z^2)} \left[-\frac{s\beta}{2}(s+2\Delta) + (\Delta^2 + m_{\tilde{w}}^2 s)\Lambda \right] \right\} \qquad \text{(A.17)}$$

where $\Delta = m_{\tilde{w}}^2 - m_{\tilde{\nu}}^2$ and $\Lambda = \ln\dfrac{s(1-\beta)+2\Delta}{s(1+\beta)+2\Delta}$.

$$E_t = 1, \quad E_{st} = \frac{L_e}{1-sin^2\theta_W}, \quad E_s = \frac{L_e^2+R_e^2}{4(1-sin^2\theta_W)^2}$$

$E_t = E_{st} = 0$ for $\tilde{\nu}_\mu$, $\tilde{\nu}_\tau$. $L_e = -1 + 2sin^2\theta_W$ and $R_e = 2sin^2\theta_W$ are the neutral current couplings of the left and right handed electron.

A.3.4 Single Zino Production

In e^+e^- interactions zinos can be produced together with a $\tilde{\gamma}$ via $\tilde{e}$ exchange with a cross section [25]:

$$\sigma(e^+e^- \to \tilde{\gamma}\tilde{z}) = \frac{4\pi\alpha^2}{s}(c_R^2+c_L^2)\beta \left[\frac{\Delta^2 - \delta^2 + \frac{s}{2}m_{\tilde{e}}^2}{\Delta^2 - \delta^2 + s\ m_{\tilde{e}}^2} - \frac{\Delta(\Delta+\frac{s}{2}) - \frac{s}{2}m_{\tilde{\gamma}}m_{\tilde{z}}}{\beta s(\Delta+\frac{s}{2})} \ln\frac{\Delta+\frac{s}{2}(1+\beta)}{\Delta+\frac{s}{2}(1-\beta)} \right] \qquad \text{(A.18)}$$

where

$$\Delta = m_{\tilde{e}}^2 - \frac{m_{\tilde{\gamma}}^2 + m_{\tilde{z}}^2}{2}, \qquad \delta = \frac{m_{\tilde{z}}^2 - m_{\tilde{\gamma}}^2}{2}.$$

and $c_R = \tan\theta_W$, $c_L = \frac{1}{2}(\tan\theta_W - \cot\theta_W)$.

$$\frac{\mathrm{d}\sigma(e^+e^- \to \tilde{\gamma}\tilde{z})}{\mathrm{d}\cos\Theta} = \frac{\pi\alpha^2}{2s}(c_R^2+c_L^2)\beta\left[\frac{(m_{\tilde{\gamma}}^2 - t)(m_{\tilde{z}}^2 - t)}{(m_{\tilde{e}}^2 - t)^2} + \frac{(m_{\tilde{\gamma}}^2 - u)(m_{\tilde{z}}^2 - u)}{(m_{\tilde{e}}^2 - u)^2} + \frac{2sm_{\tilde{\gamma}}m_{\tilde{z}}}{(m_{\tilde{e}}^2 - t)(m_{\tilde{e}}^2 - u)}\right] \tag{A.19}$$

If one of the scalar electrons $\tilde{e}_L$ and $\tilde{e}_R$ is very much heavier than the other one has to set either c_L or c_R to zero.

A.4 Higgsinos

A.4.1 Charged Higgsino Pair Production

Charged Higgsinos can be pair produced via one photon annihilation with the same cross section as e.g. a new heavy lepton, namely

$$\sigma(e^+e^- \to \tilde{h}^+\tilde{h}^-) = \frac{4}{3}\frac{\pi\alpha^2}{s}\cdot\frac{3\beta - \beta^3}{2} \tag{A.20}$$

$$\frac{\mathrm{d}\sigma(e^+e^- \to \tilde{h}^+\tilde{h}^-)}{\mathrm{d}\cos\Theta} = \frac{\pi\alpha^2}{2s}\beta\left[1 + \cos^2\Theta + (1-\beta^2)\sin^2\Theta\right] \tag{A.21}$$

A.4.2 Neutral Higgsino Production Via a Virtual Z^0

The lightest and second lightest neutral higgsino $\tilde{h}_1^0$ and $\tilde{h}_2^0$ can be produced via a virtual Z^0 in the s-channel. The cross section reads [37]:

$$\sigma(e^+e^- \to \tilde{h}_1^0\tilde{h}_2^0) = \xi\frac{\pi\alpha^2}{s}(a^2+v^2)4\chi^2\beta\left[\frac{4(E_1E_2 - \eta_1\eta_2 m_1 m_2)}{s} + \frac{\beta^2}{3}\right] \tag{A.22}$$

$$\frac{\mathrm{d}\sigma(e^+e^- \to \tilde{h}_1^0\tilde{h}_2^0)}{\mathrm{d}\cos\Theta} = \xi\frac{\pi\alpha^2}{s}(a^2+v^2)2\chi^2\beta\left[\frac{4(E_1E_2 - \eta_1\eta_2 m_1 m_2)}{s} + \beta^2\cos\Theta\right] \tag{A.23}$$

where

$$\chi = \frac{1}{16sin^2\theta_W(1 - sin^2\theta_W)}\cdot\frac{s}{s - M_Z^2 + iM_Z\Gamma_Z}$$

is the Z^0 propagator and E_i, m_i are the energy and mass of the produced higgsinos $\tilde{h}_i^0$. $v = -1 + 4sin^2\theta_W$ and $a = -1$ are the vector and axialvector couplings of the electron to the Z^0. $\eta_i = \pm 1$ is the sign of the Majorana condition (see Ellis et al. [30]) and ξ is a mixing factor and corresponds to $(\delta_1\delta_2 - \gamma_1\gamma_2)^2$ in the notation of Ref. [30]. Its maximum value is 1 in case of maximum mixing.

Appendix B

Search for Charged Scalar Particles

In contrast to the minimal Standard Model supersymmetry requires a second Higgs doublet in order to give masses to both the up and down type quarks [6]. As a consequence, supersymmetry predicts the existence of physical charged Higgses. In addition, the (at least) two Higgs doublets are required to preserve the one to one correspondence between bosonic and fermionic degrees of freedom for the weak gauge bosons and Higgses and their respective fermionic partners.

Models of dynamic symmetry breaking such as Technicolor or Extended Technicolor [34] avoid elementary scalars and thus circumvent the hierarchy problem mentioned in the introduction by postulating the Higgses to be composite objects made up of fermions bound by a strong technicolor force with a scale of $\sim$ 1 TeV. These models predict the existence of charged technipions as pseudo - Goldstone bosons with low mass. Although technipions are extended objects, their size is expected to be around 1 TeV^{-1}. Therefore, they should behave pointlike at PETRA energies.

Charged scalar particles can be pair produced in e^+e^- annihilation into a virtual photon:

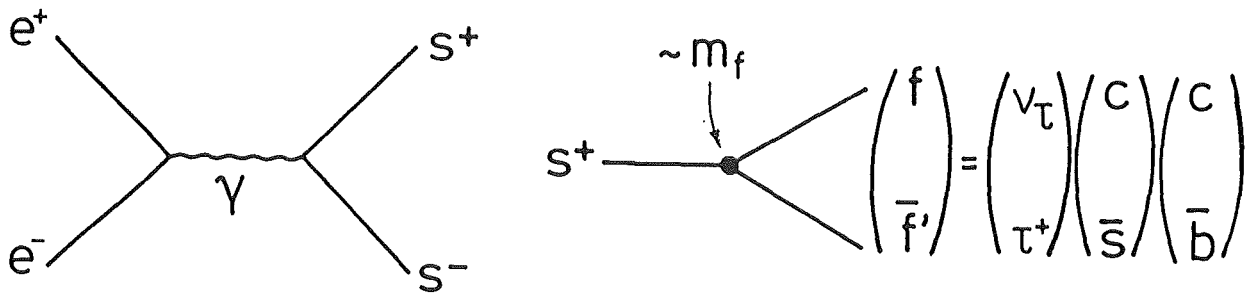

Figure B.1: Pair production and decay of charged Higgses or technipions.

with the same cross section as scalar muons or taus (see Appendix A). The production cross section close to threshold is very small compare to the μ pair cross section.

Charged scalar particles, be they Higgses or technipions, are expected to couple to fermions proportional to the fermion mass. Therefore their dominant decay modes will be into $\tau\nu$ or hadronically into $c\bar{s}$ or $s\bar{b}$ with unknown relative branching ratios. The search for acoplanar tau pairs described in section 5.1 on page 50 is sensitive to pair production of charged scalars decaying into a τ, be it charged Higgses, or technipions, or scalar taus. Fig. B.2 shows mass range excluded for a charged Higgs or technipion as a function of its branching ratio into $\tau\nu$.

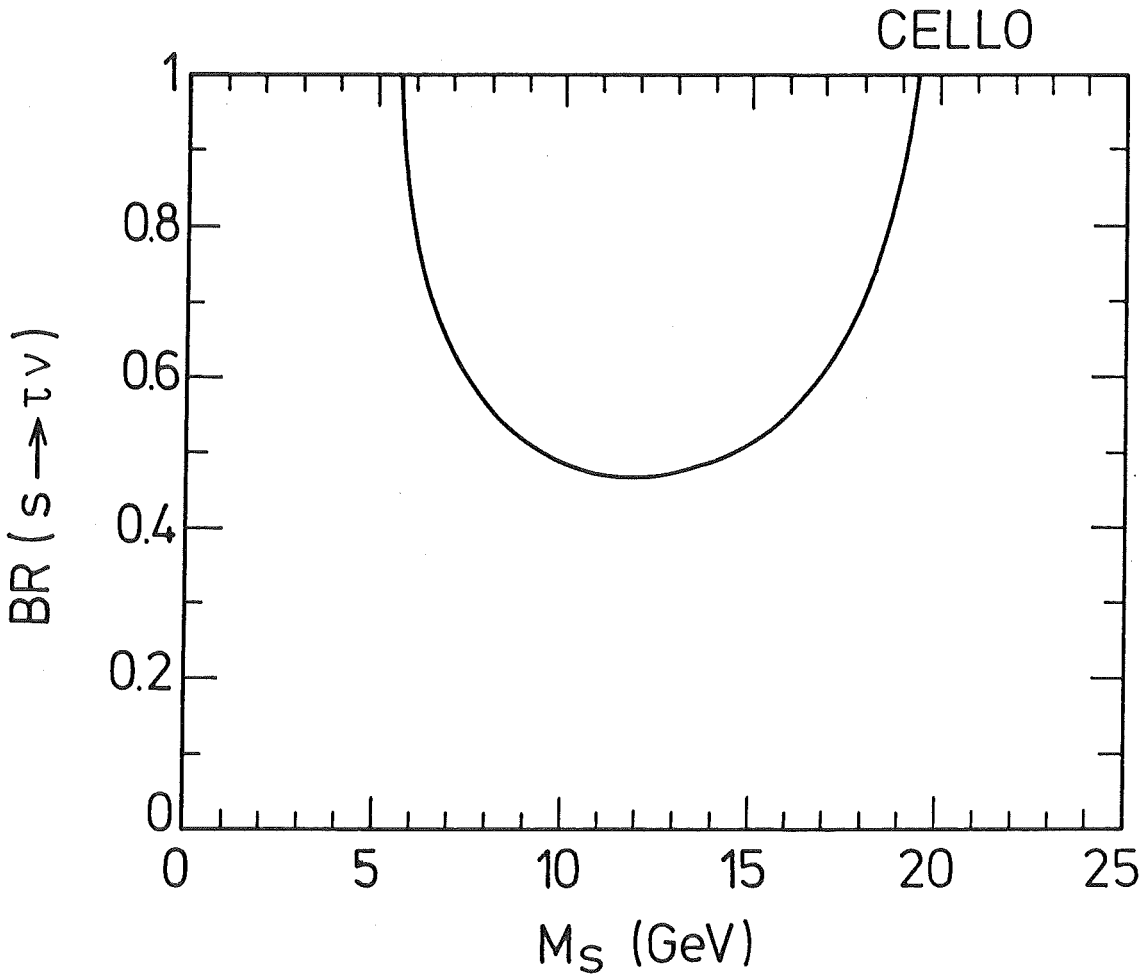

Figure B.2: Mass range for a charged Higgs or technipion excluded at 95 % C.L. as a function of its branching ratio into $\tau\nu_\tau$.

Appendix C

Charged Heavy Lepton

The standard model does not predict the number of fermion generations. The repetitve nature of the three known families suggests a search for new leptons of a possible fourth generation.

A new charged lepton would be pair produced via one photon annihilation with the same cross section as a charged higgsino, namely

$$\sigma(e^+e^- \rightarrow L^+L^-) = \frac{\beta(3-\beta^2)}{2}\sigma_{\mu\mu} \qquad \text{(C.1)}$$

where $\sigma_{\mu\mu}$ is the lowest order QED μ pair cross section.

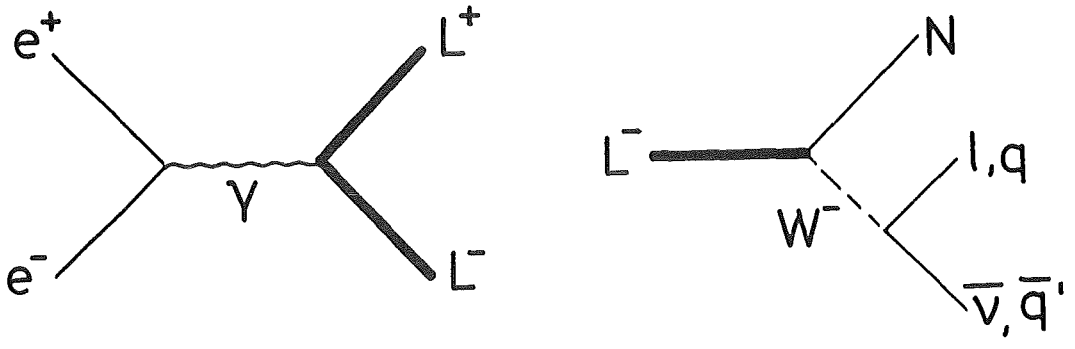

Figure C.1: Pair production and decay of a sequential heavy lepton.

It is expected to decay via W exchange into a lighter lepton and neutrinos or into hadrons and neutrino with a leptonic branching fraction of $\sim 3 \cdot 11\%$. A general signature is missing energy and momentum carried away by neutrinos (Fig. C.2).

Note that both production process and decay mechanism are identical to the case of higgsino pair production. Fig. C.3 shows the excluded heavy lepton mass range as a function of the mass of its associated neutrino as obtained from our search for acoplanar ee and $e\mu$ final states. Note that lower heavy lepton masses

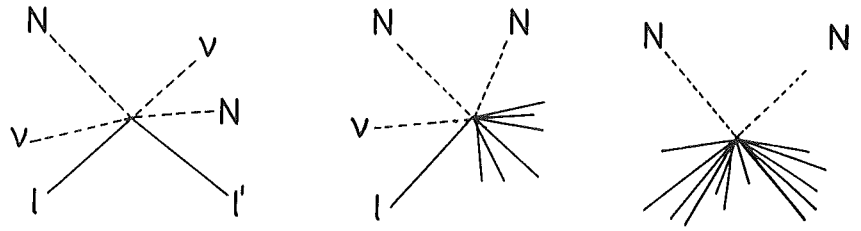

Figure C.2: Signatures of heavy lepton pair production and decay. (Compare also Fig. 2.11 on page 24.)

are completely excluded from measurements of the total hadronic and the tau pair cross sections.

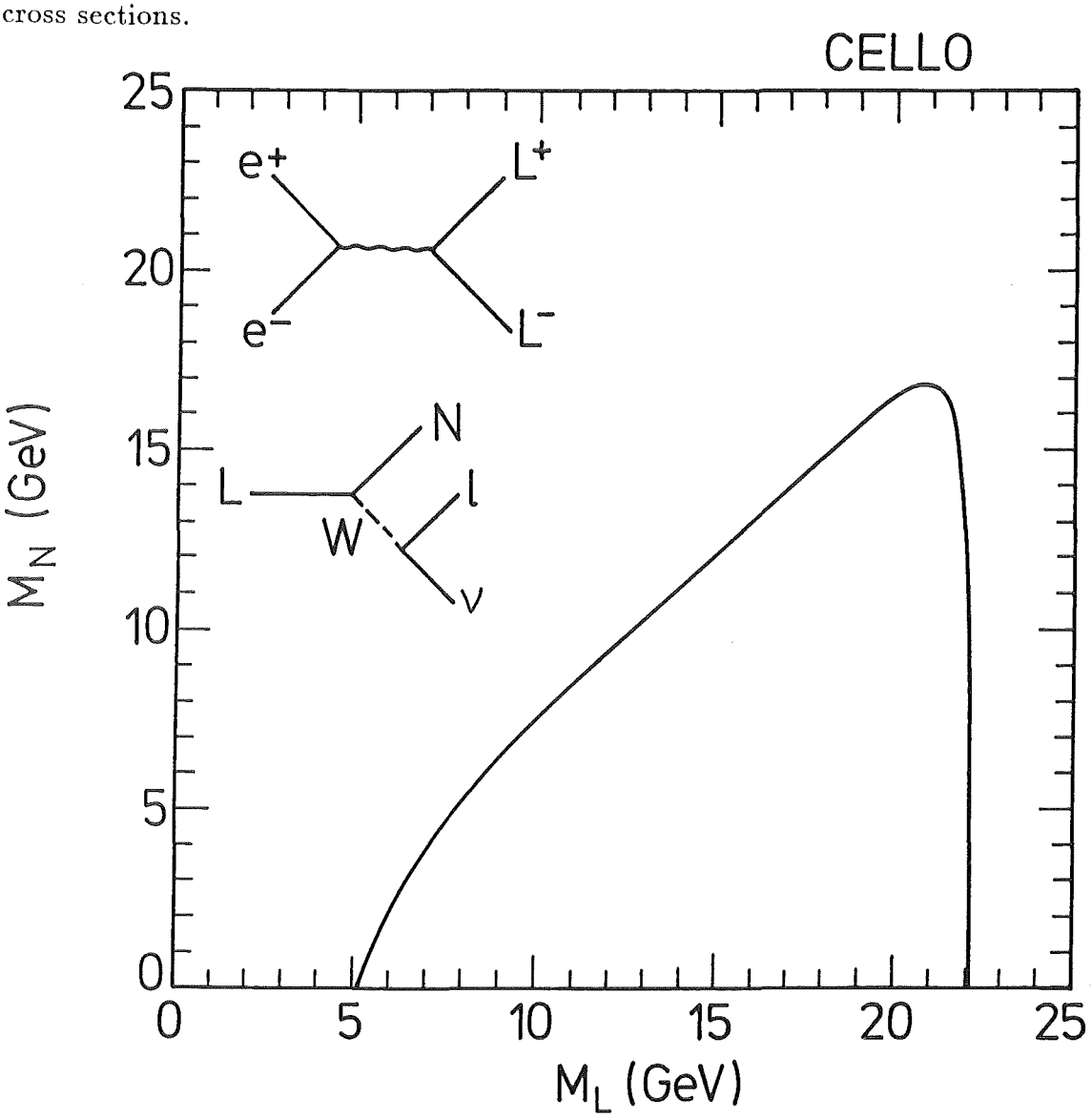

Figure C.3: Mass range excluded at 95 % C.L. for a new heavy lepton as function of the mass of its associated neutrino.

Bibliography

[1] F.J. Hassart et al., Phys. Lett. 46B(1973), 138

[2] J.J. Aubert et al., Phys. Rev. Lett. 33(1974), 1404
J.E. Augustin et al., Phys. Rev. Lett. 33(1974), 1408

[3] UA1 coll., G. Arnison et al., Phys. Lett. 122B(1983),103, 126B(1983),398, and 129B(1983),273
UA2 coll., G. Banner et al., Phys. Lett. 122B(1983),476, and P. Bagnaia et al., Phys. Lett. 129B(1983),130

[4] Kr.A. Gol'fan, E.P. Likhtman, JETP Lett. 13(1971),323
J. Wess, B. Zumino, Nucl. Phys. B70(1974),39
P. Fayet, S. Ferrara, Phys. Rep. 32C(1977), 249

[5] J.H. Schwartz, Phys. Reports 89(1983), 223
M.B. Green, Surveys in High Energy Phys. 3(1983), 127 and references therein
J. Ellis, CERN preprint TH.4255(1985)

[6] K. Inoue et al., Progr. Theor. Phys. 67(1982),927
and errata 70(1983),330 and 71(1984),413

[7] J. Ellis and J.S. Hagelin, Nucl. Phys. B238(1984), 453

[8] P. Fayet in "Unification of the Fundamental Particle Interactions", eds. S. Ferrara, J. Ellis, and P. Van Nieuwenhuizen (Plenum Press, N.Y., 1980), p. 587

[9] S.S. Gershtein and Ya.B. Zel'dovich, Pis'ma Zh. Eksp. Teor. Fiz. 4(1966), 174 (JETP Lett. 4(1966). 120)
R. Coswik and J. McClelland, Phys. Rev. Lett. 29(1972), 669
B.W. Lee and S. Weinnberg, Phys. Rev. Lett. 39(1977), 165

[10] C. Quigg, FERMILAB-Conf-85/174-T(1985)

[11] H. Goldberg, Phys. Rev. Lett. 50(1983), 1419
J. Ellis et al., Nucl. Phys. B(1984), 453

[12] N. Cabibbo, G.R. Farrar, and L. Maiani, Phys. Lett. 105B(1981),155

[13] H. Komatsu and J. Kubo, Phys. Lett. 157B(1985), 90

[14] G.L. Kane, proceedings of the XXI. Rencontre de Moriond on Perspectives in Electroweak Interactions and Unified Theories, Les Arcs, March 9-16, 1986

[15] CELLO coll., H.J. Behrend et al., DESY 87-013 (1987), submitted to Z. Phys. C

[16] JADE coll., W. Bartel et al., Phys. Lett. 139B(1984),327 and S. Komamiya, private communication

[17] MARK J coll., B. Adeva et al., Phys. Lett. 152B(1985),439

[18] TASSO coll., M. Althoff et al., Z. Phys. C26(1984), 337

[19] S. Komamiya, talk at the Int. Symp. on Lepton and Photon Int. at High Energies, Kyoto, Japan (1985), Heidelberg preprint HD-PY 86/01
J. Haissinski, talk at the XVI symposion on Multiparticle Dynamics, Kiryat-Anavim, Israel (1985), Orsay preprint LAL 85/32

[20] M. Glück, E. Reya, Phys. Lett. 130B(1983), 423
T. Kobayashi and M.Kuroda, Phys. Lett. 134B(1984), 271

[21] M. K. Gaillard et al., Phys. Lett. 116B(1982),279

[22] C. Weizsäcker and E.T. Williams, Z. Phys. 88(1934),612

[23] J.A. Grifols and R. Pascual, Phys. Lett. 135B(1984),319
M. Glück, Phys. Lett. 129B(1983),255

[24] J. Ellis and J.S. Hagelin, Phys. Lett. 122B(1983),303
K. Grassie and P.N. Pandita, Phys. Rev. D30(1984),22

[25] E. Reya, Phys. Lett. 133B(1983),245

[26] L.E Ibanez and C. Lopez, Nucl. Phys. B233(1984),511
J.S. Hagelin, G.L. Kane, and S. Raby, Nucl. Phys. B241(1984),638

[27] V. Barger et al., Phys. Lett. 131B(1983),372

[28] S. Dawson, E. Eichten, C. Quigg, FERMILAB-Pub-83/82-THY and LBL-16540, revised version October 1984

[29] J.A. Grifols and R. Pascual, Phys. Lett. 135B(1984),319
G. Eilam and E. Reya, Phys. Lett. 145B(1984),425 and
erratum, Phys. Lett. 148B(1984),502

[30] J. Ellis et al., Phys. Lett. 132B(1983),436

[31] J.M. Frere and G.L. Kane, Nucl. Phys. B223(1983),331

[32] F. Berends, P.H. Daverveldt, and R. Kleiss, Nucl. Phys. B253(1985),441

[33] F. Berends, K. Gaemers, R. Gastmans, Nucl. Phys. B68(1974), 541
F. Berends, R. Kleiss, Nucl. Phys. B228(1983), 537

[34] S. Weinberg, Phys Rev. D13(1976), 974 and D19(1979),1277
L. Susskind, Phys Rev. D20(1979), 2691
S. Dimoupolos and L. Susskind, Nucl. Phys. B155(1979), 237
E. Eichten and K. Lane, Phys. Lett. 90B(1980), 125

[35] R.M Barnett, H.E. Haber, and K.S. Lackner, Phys. Lett. 126B(1983), 64 and Phys. Rev. D29(1984), 1990

[36] D. Ware and M.E. Machacek, Phys. Lett. 147B(1984), 415
J.A. Grifols, M. Martinez, and J. Sola, Nucl. Phys. B268(1986), 151

[37] H. Baer, K. Hagiwara, and S. Komamiya, Phys. Lett. 156B(1985), 117

[38] S. Weinberg, Phys. Rev. Lett. 50 (1983) 387,
R. Arnowitt, A.H. Chamseddine and P. Nath,
Phys. Rev. Lett. 50 (1983) 232,
P. Fayet, Phys. Lett. 125B (1983) 178.

[39] J.A. Grifols, M. Martinez, and R. Pascual, Z. Phys. C29 (1985) 309

[40] CELLO coll., H.J. Behrend et al., Phys. Lett. 183B(1987), 400

[41] CELLO coll., H.J. Behrend et al., Phys. Lett. 161B(1985), 182

[42] CELLO coll., H.J. Behrend et al., preprint DESY 87-005(1987), submitted to Phys. Lett. B

[43] JADE Coll., W. Bartel et al., Z. Phys. C29 (1985) 505,
JADE Coll., W. Bartel et al., Phys. Lett. 152B (1985) 392,
JADE Coll., W. Bartel et al., Phys. Lett. 152B (1985) 385,
JADE Coll., W. Bartel et al., Phys. Lett. 146B (1984) 126,
JADE Coll., W. Bartel et al., Phys. Lett. 139B (1984) 327,
MARK J Coll., B. Adeva et al., Phys. Lett. 152B (1985) 439,
MARK J Coll., B. Adeva et al., Phys. Rev. Lett. 53 (1984) 1806,
TASSO Coll., M. Althoff et al., Z. Phys. C26 (1984) 337,
TASSO Coll., R. Brandelik et al., Phys. Lett. 117B (1982) 365.

[44] ASP Coll., G. Bartha et al., Phys. Rev. Lett. 56 (1986) 685.
MAC Coll., E. Fernandez et al., Phys. Rev. Lett. 54 (1985) 1118,
MAC Coll., E. Fernandez et al., Phys. Rev. Lett. 52 (1984) 22,
MARK II Coll., L. Gladney et al., Phys. Rev. Lett. 51 (1983) 225

[45] For a recent update, see:
M.Davier, Proc. of the 23rd Int. Conf. on High Energy Physics, Berkeley (1986), and preprint LAL 86-31,
J.F.Grivaz, ibid. and preprint LAL 86-28,
S.Whitaker, ibid. and preprint BUHEP 86-10.

[46] A.Honma, Proc. of the 23rd Int. Conf. on High Energy Physics, Berkeley (1986), and preprint CERN EP/86-153.

[47] CELLO coll., H.J.Behrend et al.,Phys.Lett. 168B(1986),420

[48] G. Franke, CELLO-Note (1984), unpublished

[49] P. Grosse Wiesmann and H. Küster CELLO-Note K-105(1985), unpublished

[50] CELLO coll., H.J. Behrend et al., Phys. Lett. 176B(1986), 247

[51] Particle Data Group, Phys. Lett. 170B(1986), 1

[52] D.A. Dicus et al., Phys. Rev. D30(1984), 1112

[53] T. Sjöstrand, Comp. Phys. Comm. 27 (1982) 243 and 28 (1983) 229
We used the updated version JETSET 5.2

[54] H. Küster, diploma thesis, Karlsruhe KfK 3610(1983)

[55] G. Bonneau and F. Martin, Nucl. Phys. B27(1971), 381

[56] CELLO coll., H.J. Behrend et al., Phys. Scr. 23(1981), 610

[57] P. Grosse Wiesmann, CELLO-Note K-67(1984), unpublished
K. Gamerdinger and H. Jung, CELLO-Note K-114(1985), unpublished

[58] H.J. Behrend, Comp. Phys. Comm. 22(1981), 365

[59] H. Küster, CELLO-Note K-106(1985), unpublished

[60] C. Jacobs, L. McCulloch, CERN CAMAC note 63-00 (1976), unpublished

[61] P.Fayet, Phys. Lett. 70B (1977),461